2014

Performance of Active Vibration Isolation in the Advanced LIGO Detectors

Ryan Thomas DeRosa
Louisiana State University and Agricultural and Mechanical College

PERFORMANCE OF ACTIVE VIBRATION ISOLATION IN THE ADVANCED LIGO DETECTORS

A Dissertation

Submitted to the Graduate Faculty of the
Louisiana State University and
Agricultural and Mechanical College
in partial fulfillment of the
requirements for the degree of
Doctor of Philosophy

in

The Department of Physics and Astronomy

by
Ryan Thomas DeRosa
B.S., University of Rochester, 2006
B.A., University of Rochester, 2006
December 2014

Acknowledgments

During my tenure at the Livingston Observatory it has been a singular privilege to interact and work with the numerous scientists and engineers who staffed and visited the site during the science run and to make Advanced LIGO. This is a *very* long list of people, and it is not possible to name them all. However, I would be remiss not to draw attention to a number of people who made my graduate education both possible and enjoyable.

I would like to thank my advisor, Joe Giaime, for his patience, advice, patience, support, and patience, and for pointing me towards a dissertation year after year.

I would like to thank Gaby Gonzalez, and Jorge Pullin, for their hospitality, particularly upon our arrival in Baton Rouge, despite its coincidence with a hurricane.

I would like to thank Rana Adhikari for involving me in the commissioning effort during Enhanced LIGO, and for offering many insightful ideas since then.

I would like to thank the seismic isolation working group for many useful discussions, in particular Brian Lantz and Richard Mittleman.

I would like to thank Sam Waldman for invigorating discussions and for always bringing a lot of energy to laboratory work.

I shared many long nights working on the big machine with my fellow commissioners, including Tobin Fricke, Kate Dooley, Jeff Kissel, Anamaria Effler, Chris Mueller, Adam Mullavey, Denis Martynov, Zach Korth, Jan Poeld, Keiko Kokeyama, and Rob Ward.

I would like to bring special attention to the efforts of Valera V Frolov, the indefatigable leader of the Livingston commissioning effort, whose collegiality, resolve, and dedication to the scientific method created a focused and productive climate in the control room. Together with this professional gratitude, I would like to add my personal thanks for many enjoyable discussions, on all topics, often rich with laughter.

Finally, I would like to thank my parents, for providing an easy and enriching childhood, and my wife Sara, for her love and support, without which this work would not have been possible.

LIGO was constructed by the California Institute of Technology and the Massachusetts Institute of Technology, with funding from the National Science Foundation. The laboratory operates under the cooperative agreement PHY-0757058.

Table of Contents

List of Figures

Abstract

The second generation of LIGO detectors has finished construction and the commissioning effort is pushing the instruments towards their designed sensitivity. Around the world similar undertakings are underway, and soon a global network capable of astrophysical observation will be operational. The first sentences are being written in an important chapter of terrestrial gravitational wave detection, an entire century after the theoretical foundations of general relativity were laid, and after decades of calculation, design, proposals, plans, and laboratory work.

In order to make sensitive measurements, the detector must be well isolated from the vibrations of the ground, and much of this thesis describes the effectiveness of active control platforms used to mitigate the transmission of seismic motions to the test masses. This work was performed both during the last science run of the first generation LIGO detector and as part of the commissioning of the second generation instrument.

1

Introduction

1.1 Gravitational Radiation

In order to avoid violating causality, theories describing gravitational interaction must include gravitational waves (GWs). The theory of general relativity (GR) [1] describes these waves as traveling disturbances in the space-time metric, $g_{\mu\nu}$, which propagate with the speed of light, c. The metric is a tensor quantity which describes a space-time geometry by determining the interval between events, ds, via the computation [1]

$$ds^2 = g_{\mu\nu} dx^\mu dx^\nu, \tag{1.1}$$

where dx^μ and dx^ν are the coordinate distances (three spatial and one time) of the two events, the metric is defined locally, and lowered indices repeated in superscript are assumed to be summed, that is $a_\mu b^\mu = \sum_{\mu=0}^{3} a_\mu b^\mu$. These GWs are generated by accelerating mass, and are a particular solution to the field equations,

$$G_{\mu\nu} = \frac{8\pi G}{c^4} T_{\mu\nu}, \tag{1.2}$$

where $G_{\mu\nu}$ is the Einstein tensor (describing space-time curvature), G is the gravitational constant, and $T_{\mu\nu}$ is the stress-energy tensor (describing matter and energy

distributions). Far from the source (the "weak-field" regime) the disturbance in space-time caused by GWs can be approximated as a small perturbation, $h_{\mu\nu}$, to the metric,

$$g_{\mu\nu} \simeq \eta_{\mu\nu} + h_{\mu\nu}, \text{where } |h_{\mu\nu}| \ll 1, \tag{1.3}$$

and where $\eta_{\mu\nu}$ is the Minkowski ("flat-space") space-time metric. After some coordinate transformations the perturbation for a wave, propagating with a frequency ω in the z direction, can be written as

$$h_{\mu\nu}(z,t) = \begin{pmatrix} 0 & 0 & 0 & 0 \\ 0 & -h_+ & h_\times & 0 \\ 0 & h_\times & h_+ & 0 \\ 0 & 0 & 0 & 0 \end{pmatrix} \cos[\omega(\mathrm{t} - \frac{\mathrm{z}}{\mathrm{c}})] \tag{1.4}$$

where t is time, and h_+ and h_x represent the two gravitational wave polarizations, referred to as "plus" and "cross". Besides the two polarizations another notable feature evident in this formulation is that GWs only create a disturbance in the two directions transverse to their direction of propagation. It should also be noted that monopole and dipole radiation are forbidden by the conservation of energy and momentum, respectively. Quadrupole radiation is the lowest order allowed, so any source of GWs must have a non-zero quadrupole moment.

An important consequence of a passing GW is their effect on the proper distance between two inertial bodies. If there is one object placed at the origin of our coordinate system, $dx^\mu = (t, 0, 0, 0)$, and another placed at a position $dx^\nu = (t, L_0, 0, 0)$, then the proper distance between will be the path integral

$$L_{\text{proper}} = \int \sqrt{|ds^2|} = \int \sqrt{|g_{\mu\nu} dx^\mu dx^\nu|}. \tag{1.5}$$

For this simple example, this reduces to

$$L_{\text{proper}} = \int_0^{L_0} \sqrt{|g_{xx}|}dx, \tag{1.6}$$

at any given moment. If a + polarized GW passes by the inertial test masses, traveling in the z direction, Equation 1.6 becomes,

$$L_{\text{proper}} \simeq L_0\sqrt{\eta_{xx} + h_{xx}} \simeq L_0\left(1 + \frac{h_+}{2}\right) \tag{1.7}$$

when $|h_+|$ is small. The amplitude of the fluctuation in the distance between the two test masses is $\delta L_{\text{proper}} = L_0\frac{h_+}{2}$, and it is a key point that the disturbance is proportional to the unperturbed distance, L_0. That is, the gravitational wave produces a strain,

$$\frac{\delta_L}{L_0} = \frac{h_+}{2}. \tag{1.8}$$

In the perpendicular direction, a + polarized wave would produce the same strain, but with opposite sign, and the effect of the wave on a ring of test masses would resemble Figure 1.1.

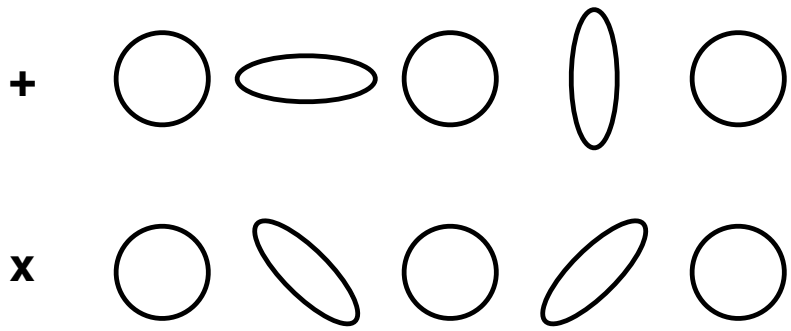

FIGURE 1.1. Cartoon depicting the effect of + and x polarized gravitational waves, propagating into the page, on a ring of inertial test masses. Each consecutive image is advanced in time by 1/4 of the GW's period.

1.2 Astrophysical Sources

The chief difficulty in detecting gravitational waves is their exceedingly small effect when received on Earth, with a typical strain scaling as $h \sim GMv^2/Rc^4$, where R is the distance to the object which has mass M, and is moving at velocity v. Despite the unfriendly factor of $G/c^4 \simeq 10{-}44$ s^2/m kg, astrophysical masses moving at relativistic speeds stand a chance of terrestrial detection. Several potential sources are studied and usually divided by event duration and waveform characteristics into a 2x2 table:

	Modeled waveforms	Un-modeled or no waveforms
Short ($t_{\rm dur} <$ minutes)	Binary inspiral	Supernovae and other Bursts
Long (continuously emitted)	Pulsar spin-downs	Stochastic/Cosmological Background

When the model waveform is available, potential signals can be judged not only by coincidence in time and frequency between the two detectors, but also by how well they fit the analytical forms. The brief modeled waveforms of binary inspirals take on a characteristic signal, described below, which includes a series of signal sign reversals which help to distinguish it, while pulsar signals are so long lived they should be modulated by a known Doppler shift as the Earth moves relative to the source.

1.2.1 Binary Inspirals

The coalescence of two compact objects such as neutron stars and black holes is expected to be the fiducial source for gravitational wave detectors, and to some extent terrestrial detectors are designed with them in mind [2]. While these signals are considered to be short duration for LIGO, in truth the detector is only going to catch the final 10's or 100's of seconds of what is most likely a 100's of millions

of years long process. Two neutron stars, each with mass M and a distance R from the Earth, in circular orbits about each other in the x-y plane, will produce gravitational waves propagating in the z direction with amplitude [3]

$$h_+(t) = \frac{32\pi^2 G}{Rc^4} M r^2 f^2 \left(\frac{1+\cos(\theta^2)}{2}\right) \cos\left(4\pi \mathrm{ft}\right), \tag{1.9}$$

where r is half of the distance between the stars, f is the frequency of their orbit, θ is the angle between the z axis the observer's line of sight.

Interesting things to note about Equation 1.9 are that the gravitational waves are emitting at twice the orbital frequency, and that they only decay as $1/r$ as they propagate away from the source. The radius of the orbit and its frequency are not independent, $f = \sqrt{GM/16\pi^2 r^3}$. After plugging in some numerical constants the amplitude of this strain can be rewritten as

$$h \simeq 1.6\mathrm{x}10^{-20} \left(\frac{M}{1.4\odot}\right)^2 \left(\frac{1\ \mathrm{Mpc}}{R}\right), \left(\frac{f}{100\ \mathrm{Hz}}\right)^{2/3} \tag{1.10}$$

when the binary system is optimally aligned to the detector (orbital plane normal to line of sight). For a 1.4-1.4 solar mass binary neutron star system in the Virgo cluster ($R \sim 15$ Mpc away), the expected strain in the last moments of the inspiral signal is therefore $h \sim 10^{-21}$.

Of special note regarding such star systems is the Hulse-Taylor binary, discovered in 1974, for which the indirect detection of gravitational waves has already been confirmed [4]. The electromagnetic signals from the pulsar in this binary neutron star system allowed for the careful measurement of its orbital decay, which matches the expected decay with the inclusion of energy lost due to emitted gravitational waves to better than 1% [5]. As binary systems' orbits decay the frequency of their rotation increases, which results in a ramp-up in the strain amplitude as can be

seen from Equation 1.10: the characteristic "chirp" signal. Since a waveform is predicted, matched filtering and parameter estimation are used in addition to the standard data cuts to further constrain the search analyses [6], although no signals have been detected.

1.2.2 Supernovae/Bursts

Other short duration signals include supernovae and un-modeled bursts, possibly including those from the merger of two compact objects at the completion of their inspiral phase. The theoretically predicted energy conversion to gravitational waves in core-collapse supernovae of $\sim 10^{-10}$ - 10^{-8} $M_{\odot}c^2$ [7] limits the sensitive range of modern detectors to 10-100's of kpc (as opposed to 10-100's of Mpc for binary inspiral events). Modeling suggests that the strain amplitude depends strongly on the angular velocity of the core upon collapse, and that the frequency of the peak signal will be in the vicinity of 650-800 Hz. [7]. While binary inspiral events are most likely going to be relied upon as "standard siren" sources due to a priori knowledge of the waveform, the reverse may be true for a supernova in that the gravitational wave signal may provide heretofore unobtainable information about the physics of core collapse [8].

1.2.3 Continuous Wave

Spinning objects such as neutron stars and pulsars will likely produce gravitational waves, confined to a single frequency which is then Doppler shifted as the detector moves relative to the source. If such an object is truly symmetric about its rotation axis, it will not possess a time varying quadrupole moment, and therefore not radiate gravitational waves. However, if there is a deviation from symmetry the

spin will produce a sinusoidal disturbance, at twice the rotation frequency, with strain amplitude [9]

$$h = \frac{16\pi^2 G}{rc^4}\varepsilon I f^2, \tag{1.11}$$

where f is the neutron star's rotation frequency, I is its principal moment of inertia, r is its distance from the detector, and ε is its *equatorial ellipticity*. Since these are long-term signals, with known f and sky position in the case of pulsars, data can be integrated to reach sensitivities below the stationary noise background of the detector. Using the gravitational wave detector data collected to date, limits have been set on pulsar strains which correspond to ϵ's as low as $\sim$ 7x10^{-8} [9, 10, 11].

1.2.4 Stochastic Backgrounds

While all of the astrophysical signals described above are single sources detected individually, there is also inevitably a stochastic background of unresolved sources. This ensemble could be a combination of inspirals, supernovae, etc. or could, more excitingly, be of cosmological origin [12], akin to the cosmic microwave background (CMB)[13, 14]. While the CMB's surface of last scattering was on the order of 10^5 years after the Big Bang, when hydrogen recombination produced an optically thin environment, the weak interaction of gravitational waves with matter places the surface of last scattering very close to the Big Bang[15, 16]. Typically the stochastic background is discussed in terms of a (dimensionless) quantity, which is obtained by integrating the following expression over the frequency band of interest,

$$\Omega_{\rm gw}(f) = \frac{1}{\rho_{crit}}\frac{d\rho_{gw}}{d\ln f}, \tag{1.12}$$

where $\rho_{\rm gw}$ is the energy density of gravitational waves, and $\rho_{\rm crit}$ is the energy density required to close the universe.

The frequency dependence of $\Omega_{\rm gw}(f)$ varies between different cosmological models, but in general the detection scheme is the same. Assuming the instrument noises are statistically independent between detectors, cross-correlating their outputs and integrating over long periods should reveal the strain noise power generated by the underlying GW background, with the measurement or limit improving as $\sqrt{T}$, the integration time [17]. Current and planned detectors are separated widely across the planet, in order to improve the resolution of point source locations [18], so the condition that instrument noises are independent is not a difficult one, except perhaps in the case of atmospheric magnetic resonances [19]. While the separation between detectors allows for correlation studies, it does come at the cost of reduced response of the combined network due to location and alignment deviations, compared to co-located and co-aligned detectors [20]. To date, an upper limit on $\Omega_{\rm gw}$ in the LIGO band has been set at $6.9\text{x}10^{-6}$ [21, 22, 23].

1.3 Thesis Outline

The rest of this thesis will focus on problems involved with the commissioning and performance of the second generation of interferometric gravitational wave detectors, specifically Enhanced LIGO (eLIGO) and Advanced LIGO (aLIGO).

- Chapter 2 will give an overview of terrestrial detectors in general, including the historical performance of Initial LIGO (iLIGO) and Enhanced LIGO (eLIGO), as well as the expected performance of aLIGO. The state of aLIGO at the time of this writing is also briefly presented.

- Chapter 3 will detail vibration isolation schemes used in aLIGO, including their control schemes and performance to date. Some advanced techniques used during eLIGO which are applicable today are also desribed.

- Chapter 4 will discuss potential future work on low frequency isolation, a topic which arises in Chapter 3, where low frequency indicates motion below 0.1 Hz. Some modeling of novel schemes is presented.

- Chapter 5 discusses mechanisms which relate the previous chapters topic of low frequency isolation to the signal band of gravitational wave detectors. Non-linear effects and their mitigation, especially during eLIGO, are explored.

- Chapter 6 details a study of piezoelectric actuators, used in eLIGO and aLIGO, including the results of a table top experiment.

- Chapter 7 briefly proposes future work which could extend the work of this thesis, and Chapter 8 offers concluding remarks.

Research work on a physics experiment as large as LIGO inevitably involves a good deal of collaboration. Also, the longevity of the experiment produces a situation where the design, prototyping, and final implementation of any particular piece of instrumentation are not always carried out by a single individual, but are rather pushed forward by a procession of scientists, engineers, and students. For the ease of the reader, the contents of this dissertation are presented in a more generally descriptive manner, with the author's individual contributions specified here. Also, although mentioned and shown later in this thesis, I did not participate in the mechanical design of any of the isolation platforms (this work being completed before I began my graduate studies).

Regarding the HEPI system: HEPI was previously commissioned at the Livingston Observatory and was a fully functional isolator before my involvement with the experiment [74, 73], with isolation performance similar to that shown in

Chapter 3. The work presented on global feed-forward using HEPI during the sixth science run was a collaboration between me and my co-authors listed in the related journal article [75]. Personally, I:

- Collected and weighted the cavity control signal and seismometer data
- Calculated the FIR Wiener filters and fit them to IIR coefficients
- Measured the transfer functions between witness sensors and cavity control signals, and fit them for inversion
- Analyzed the effects on the in-band noise and duty cycle, using established software available to the collaboration

After the installation of Advanced LIGO, I also measured the interaction between X and Y force application onto the HEPI cross-beams and the inertial sensors of the in-vacuum isolation platform.

Regarding the HAM ISI: extensive prototyping was done, including a PhD thesis by Jeffrey Kissel[88], albeit with a significantly less rigid support structure than the final implementation, which limited the control bandwidth achieved previous to this work (the isolation platform itself is almost identical). I designed both the blend and controller filters presented here, producing platform motions significantly below their requirements (and previously achieved results) around 1 Hz. The sensor correction filters used on HAM ISI's were designed previously in a separate PhD thesis, by W. Hua [71]. I also calculated the expected platform motion using a Simulink [77] model.

Regarding the BSC ISI: similar to the HAM ISI, a prototype was built and tested, also described in W. Hua's thesis [71], albeit with a significantly different control topology relying on subtraction, rather than feedback, for isolation at the

peak in the ground motion (the microseism). The decision for this design shift was motivated by the on-going detector commissioning efforts. I designed the blend, control, and sensor correction filters used for the results shown here, and modeled both the expected platform motion and the effect of the position sensor plate misalignment on the transfer of ground motion and tilt to the platform. I also measured and compensated for the plate's deviation from parallelism on the units deployed at the Livingston observatory, with help from Celine Ramet and Richard Mittleman.

Regarding the integrated systems performance: studying the platform motion with interferometric cavities was not previously achieved (or possible) during prototyping, so as part of the detector commissioning team this was one of my chief goals. I calculated the expected cavity motion from the modeled platform motion and made comparisons once each cavity was stably controlled.

I created all of the modeled platform motions in the Chapter 4, describing low frequency controls improvements. I also proposed and demonstrated the differential position sensor feed-forward technique shown.

Regarding the transient effects described in Chapter 5: I did the analyses of the platform control's effect on the propagation of ground transients, using search algorithms designed previously [103], with slight adaptations to account for the particular spectral content of the signals I was most interested in. I devised, performed, and analyzed the upconversion experiment looking for non-linearities in the corner interferometer, as well as the associated electronics investigation, with helpful suggestions from both Rana Adhikari and Valera Frolov.

Regarding the piezo actuator experiment: I assembled and analyzed this experiment at the Livingston observatory, including the interferometric apparatus and

digital controls system, in collaboration with Valera Frolov. The original proposal for this experiment came from Valera Frolov and Peter Fritschel.

2

Gravitational Wave Detectors

2.1 Resonant Bars

In order to detect gravitational waves we need a transducer capable of converting (tiny) strains into measurable signals (currents, voltages, etc.). Early efforts focused on the design of resonant mass detectors, usually in the form of large metal cylinders, and usually referred to as *Weber bars*, after their pioneer J. Weber. Such detectors rely on the excitation of the rigid body modes by stresses exerted on them by passing gravitational waves [24], and the transfer of this motion to a second, smaller oscillator. Although a narrow-band detector, pulse signals with a relatively wide frequency content can be found this way, by placing the resonant response at a suitable frequency, and maintaining a high quality factor to amplify the signal. The motion of the smaller oscillator is converted to an electrical signal, originally done with piezoelectric crystals.

Weber's original program of experiments involved several aluminum bars, with most of them co-located and one separated by about 1000 km, and a successful detection claim was made [25]. Despite the failure to reproduce these results, and subsequent refutation of Weber's claim [26, 27], resonant mass detector research was not deterred and instrument development continued. Modern devices, such as the recently decommissioned ALLEGRO detector at LSU [28], cool the

antennae to cryogenic temperatures to reduce thermal noise (the Q factor of aluminum also increases when sufficiently cooled), and use super-conducting readout devices (SQUIDs) for improved sensitivity, achieving sensitivities approaching 10^{-21} strain/$\sqrt{\text{Hz}}$ around 900 Hz [29].

2.2 Interferometers

2.2.1 Resonant Cavities

Around the same time experiments with bars were being performed, discussion of interferometric detectors began [30], wtih the promise of both sensitivity and bandwidth improvements when compared to resonant bar detectors. The travel time for light sent between two inertial masses will fluctuate when a GW passes by, and this travel time can measured as optical phase changes in an interferometric cavity. Here, the free-falling objects are actually the mirrors which reflect the probe beam, and the cavity is sometimes referred to as a *Fabry-Perot interferometer* [31, 32], with a schematic shown in Figure 2.1.

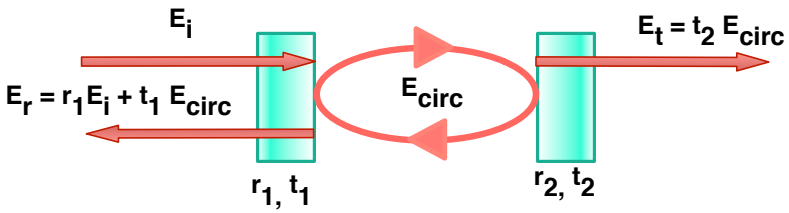

FIGURE 2.1. Cartoon of a Fabry-Perot interferometer, constructed by interfering a laser field returning from the cavity, E_{r}, with light circulating within the cavity which leaks out of the input mirror.

Here, E_{circ} is defined on the right-hand side of the input mirror, and the convention used is the explicit addition of a π phase shift when the field is reflected from the cavity side of the mirror. In practice the probe light incident on the cavity is a laser beam, and if the intra-mirror distance is such that the phase of the incident field coincides with the phase of the field returning from the far mirror

there will be a build-up of light in the cavity, which is said to be *on resonance*. If we write the incident electric field as E_{i}, and the field reflection and transmission coefficients for the first and second mirrors are $r_{1,2}$ and $t_{1,2}$, respectively, then the fields in reflection and transmission of the cavity can be written in terms of the mirror properties and input field as,

$$E_{\mathrm{r}} = E_{\mathrm{i}} \frac{r_1 - (r_1^2 + t_1^2) r_2 e^{i2\varphi}}{1 - r_1 r_2 e^{i2\varphi}}, \tag{2.1}$$

$$E_{\mathrm{t}} = E_{\mathrm{i}} \frac{t_1 t_2 e^{i\varphi}}{1 + r_1 r_2 e^{i2\varphi}}, \tag{2.2}$$

where φ is the optical phase accumulated during a one-way transit between mirrors. For a cavity of length L, the phase depends on both the mirror distance and the laser frequency, $\varphi = kL = (2\pi/\lambda)L = \pi\nu/f_{\mathrm{fsr}}$, where k is the "wave-number" of the field, $\lambda = c/\nu$ is the wavelength of the light, ν and ω are the frequency and angular frequency of the light, respectively, and $f_{\mathrm{fsr}} = c/2L$ is the cavity's *free spectral range* (the spacing between successive resonances). Equation 2.1 shows that the field in reflection of the cavity contains a measurement of the optical phase, and therefore this cavity is a potential gravitational wave detection device. It is also important to note that the sign of a field reflected by an on-resonance, *over-coupled* ($r_2 > r_1$) cavity is inverted.

In order to keep the cavity on resonance (at the linear operating point), feedback control must be employed. A common solution to this problem is the Pound-Drever-Hall (PDH) technique [33]. A phase modulation is applied to the laser light before entering the cavity, producing a set of *sidebands* on the main *carrier* light, producing a new input field of

$$E_{\mathrm{i}} e^{\Gamma \sin(\Omega t)} = E_{\mathrm{i}} \sum_{N=-\infty}^{\infty} i^N J_{\mathrm{N}}(\Gamma) e^{iN\Omega t} \tag{2.3}$$

where J_{n} is the n^{th} order Bessel function of the first kind, and Γ is the *modulation depth*, and Ω is the modulation frequency. The $N = 0$ term ($E_{\mathrm{i}} J_0(\Gamma)$) corresponds to the carrier, with higher order terms representing the symmetric sidebands. Low order sidebands dominate the non-carrier field in reflection of the cavity, since $\Gamma < 1$, and upon demodulation at Ω an error signal linear in cavity phase detuning appears,

$$\varepsilon \propto \frac{P_{\mathrm{i}} \Gamma \mathcal{F}}{\lambda} \delta L \tag{2.4}$$

where $\mathcal{F}$ is the cavity *finesse*, $\mathcal{F} = \pi\sqrt{r_1 r_2}/(1 - r_1 r_2)$. The length of the cavity or the frequency of the source can then be adjusted to null this signal. Figure 2.2 shows the slope of this signal for a high finesse ($\mathcal{F} \sim 100$'s) cavity.

If the mirrors of a Fabry-Perot cavity are highly reflective the light inside the cavity can be expected to make several round-trips before leaking through either mirror. This will amplify the effect of a passing gravitational wave until the storage time of the cavity exceeds half of the signal period, after which cancellation will begin to attenuate the accumulated phase. This gain-bandwidth trade-off, also known as the *phase gain*, is equal to

$$g_\varphi = \frac{2\mathcal{F}}{\pi} \frac{1}{\sqrt{1 + (f/f_{\mathrm{c}})^2)}}, \tag{2.5}$$

where f_{c} is the *cavity pole* (half the cavity linewidth). The cavity's pole frequency, finesse, and free spectral range are inter-related,

$$\mathcal{F} = \frac{f_{\mathrm{fsr}}}{2 f_{\mathrm{c}}}. \tag{2.6}$$

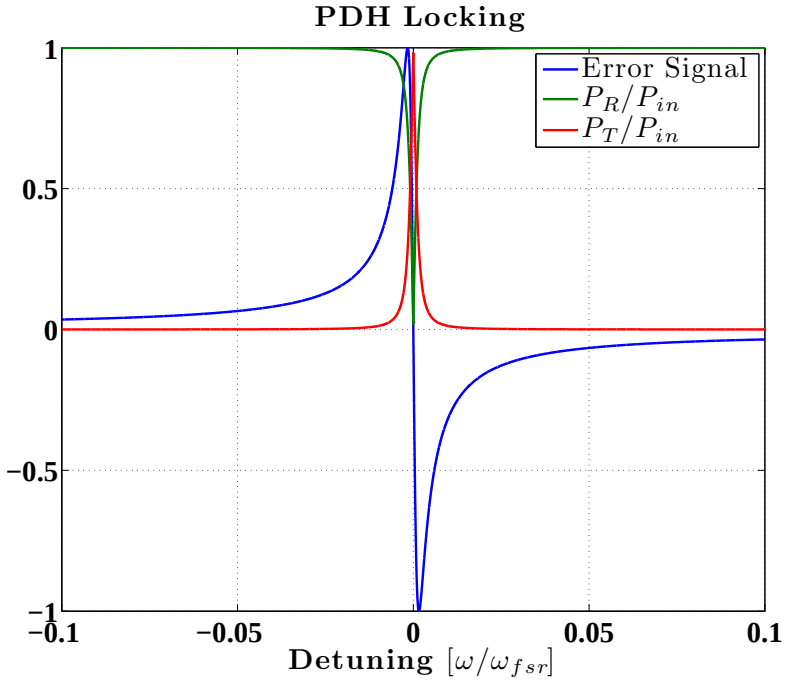

FIGURE 2.2. The PDH locking technique allows for the use of feedback to match cavity length and source frequency. For a critically coupled cavity ($r_1 = r_2$, when the error signal is nulled the cavity resonates, with the reflected power approaching zero and the transmission approaching the input power. Sideband resonances produce similar PDH error signals, but with opposite slopes to the carrier so they can be differentiated.

A high finesse cavity effectively increases arm length, an important factor for a strain detector.

While for $f < f_c$ a high finesse cavity can have a large response in the reflected field to phase detuning, it is equally sensitive to frequency fluctuations of the input field, $\delta\varphi = \delta L/L + \delta\nu/\nu$. For a $\lambda = 1$ µm laser ($\nu \simeq 3\text{x}10^{14}$), a frequency stability on the order of $3\text{x}10^{-7}$ Hz/$\sqrt{\text{Hz}}$, at ∼100 Hz, would be required to detect strains of 10^{-21}, and no such timing standard exists. The difficulty in such experiments, as well as how such a detection apparatus would be constructed and read-out when searching for pulsars, is described in [34].

2.2.2 Michelson Interferometers

A Michelson interferometer [35], where each perpendicular arm is a resonant Fabry-Perot cavity, can make use of the phase gain as well as provide immunity to frequency fluctuations of the input field, since they will be common to both arms and only differential phase changes, such as those caused by gravitational waves, will manifest at the dark (anti-symmetric) port. A schematic drawing of a Michelson interferometer is shown in Figure 2.3

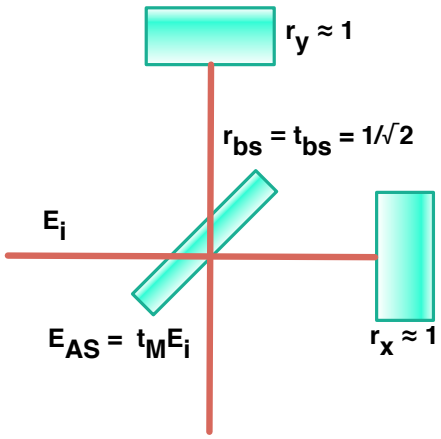

FIGURE 2.3. Cartoon of a Michelson interferometer. The four sides of the beamsplitter form two arms and two output ports. The path which returns to the input is referred to as the "bright" or "symmetric" port, while the other output is referred to as the "dark" or "anti-symmetric" port. The bright and dark terminology correspond to a specific mode of operation of a Michelson interferometer. In LIGO the arm in transmission of the beamsplitter is also called the "X arm", while in reflection it is the "Y arm".

In a simple Michelson, we can describe the field transmission and reflection coefficients as we do for a mirror, with the transmission coefficient defined as (assuming a 50/50 beamsplitter),

$$t_{\mathrm{M}} = \frac{E_{\mathrm{AS}}}{E_{\mathrm{i}}} = \frac{1}{2} r_{\mathrm{x}} e^{i2\varphi_{\mathrm{x}}} - \frac{1}{2} r_{\mathrm{y}} e^{i2\varphi_{\mathrm{y}}}, \tag{2.7}$$

where $\varphi_{\mathrm{x,y}}$ are the optical phases accumulated by traversing the X and Y arm lengths, and $r_{\mathrm{x,y}}$ are the field reflectivities of the mirrors at the ends of the arms

(whose values are close to 1). The beamsplitter is given, by convention, a π phase flip when reflecting from the anti-symmetric port side. Re-writing this with the mean and differential reflectivity, $r_+ = (r_\mathrm{x} + r_\mathrm{y})/2$ and $r_- = r_\mathrm{x} - r_\mathrm{y}$, and mean and differential phases, $\varphi_+ = (\varphi_\mathrm{x} + \varphi_\mathrm{y})/2$ and $\varphi_- = \varphi_\mathrm{x} - \varphi_\mathrm{y}$, we find

$$t_\mathrm{M} = e^{i2\varphi_+} \left(i r_+ \sin(\varphi_-) + \frac{r_-}{2} \cos(\varphi_-) \right). \tag{2.8}$$

If the mirror reflectivities are well matched, $r_- = 0$, and the arm lengths are set to keep the anti-symmetric port dark, $\varphi_- \simeq 0$, then the field at the output of the Michelson will depend linearly on the fluctuations in differential phase but only weakly depend on common-mode fluctuations of the input field. We cannot sense the field directly (it oscillates at $\sim$300 THz), so instead we measure the power, P_AS,

$$E_\mathrm{AS} = E_\mathrm{i} t_\mathrm{M}, \tag{2.9}$$

$$P_\mathrm{AS} = |E_\mathrm{AS}|^2 = P_\mathrm{i} \sin^2(\varphi_-), \tag{2.10}$$

assuming the end mirrors are totally reflective.

In a Fabry-Perot Michelson, where the end mirrors are replaced by resonant cavities, the r_x and r_y terms of Equation 2.7 are modified to include the phase gain, Equation 2.5, resulting in a transmission coefficient of

$$t_\mathrm{M} \simeq i r_+ e^{i2g_\varphi\varphi_+} \sin(g_\varphi \varphi_-), \tag{2.11}$$

where r_+ now indicates the mean reflectivity of the arm cavities, as in Equation 2.1. Although some modifications to this layout are described in the next sections,

the core readout scheme of interferometric detectors exists already in the Fabry-Perot Michelson: the common arm length (CARM) is used as the laser frequency reference, while measurement of the differential arm length (DARM) is used to detect gravitational waves.

2.2.3 Recycling

With the Michelson held on the dark fringe, most of the laser power returns from the interferometer back towards the source. The addition of another mirror between the laser and the beamsplitter, as shown in Figure 2.4, creates another resonant cavity, where the Fabry-Perot Michelson acts as one end mirror.

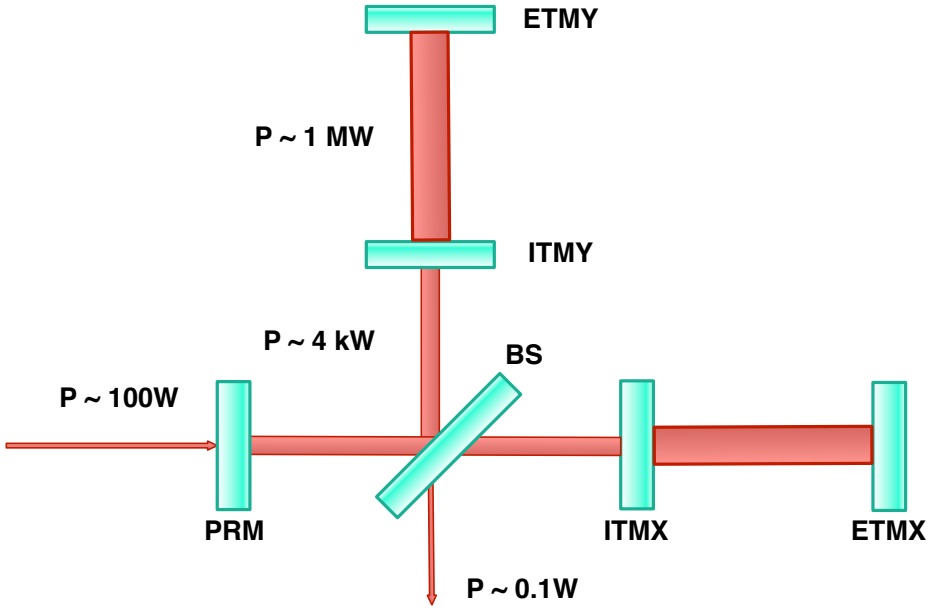

FIGURE 2.4. Cartoon of a power recycled Michelson interferometer with Fabry-Perot arms (PRFPMI). The power levels shown are in-line with what is expected to be used in second generation detectors. The mirror labels are: PRM (power recycling mirror), BS (beamsplitter), ITMX/Y (input test mass X or Y), and ETMX/Y (end test mass X or Y).

This technique is known as *power recycling* [36], and correspondingly the extra mirror is the *power recycling mirror*. If the reflectivity of the Fabry-Perot Michelson is

$$r_{\mathrm{fpmi}} = \frac{r_1 - r_2(1 - \mathrm{losses})}{1 - r_1 r_2}, \tag{2.12}$$

where r_1 and r_2 are the arm cavity mirror reflectivities, then the coupled cavity formed by the power recycling mirror and the Fabry-Perot Michelson will have a power recycling gain of

$$g_{\mathrm{prc}} = \frac{t_{\mathrm{prm}}}{1 - r_{\mathrm{prm}} r_{\mathrm{fpmi}}}, \tag{2.13}$$

where $r_{\mathrm{prm}} = \sqrt{1 - t_{\mathrm{prm}}}$ is the reflectivity of the power recycling mirror. This means that there will be g_{prc}^2 more light incident on the beamsplitter than on the power recycling mirror, or $[g_{\mathrm{prc}}/t_{\mathrm{prm}}]^2$ more light incident on the beamsplitter in the recycled vs. non-recycled configuration (i.e., with or without the power recycling mirror aligned). The value of r_{prm} is chosen to match the overall losses in the rest of the interferometer, such that the input power is critically coupled into the detector. When considered independently, the short power recycling cavity (PRC, only including the input mirrors of the arm cavities and the power recycling mirror) is actually anti-resonant for the carrier field, relying on the sign change of this field upon reflection from the arm to create power build-up.

The motive to increasing the circulating power with recycling gain follows from a fundamental limit on the interferometer's phase measurement capability: *shot noise*. The discrete nature of the laser field detected at the dark port of a Michelson results in photon counting errors, with a power fluctuation of

$$\delta P_{\mathrm{shot}} = \sqrt{2h\nu P_{\mathrm{AS}}} = \sqrt{2h\nu P_{\mathrm{BS}} \sin^2(\varphi_-)}, \tag{2.14}$$

where h is Planck's constant, and P_{BS} is the power incident on the beamsplitter (P_{i} for a simple Michelson, $P_{\mathrm{i}} g_{\mathrm{prc}}^2$ with power recycling). The derivative of P_{AS} with

respect to the differential phase is known as the *optical gain* (with unit of W/rad), and reveals the phase sensitivity due to shot noise (when φ_- is small) to be

$$\frac{dP_{\rm AS}}{d\varphi_-} = 2P_{\rm BS}\sin(\varphi_-)\cos(\varphi_-), \tag{2.15}$$

$$\delta\varphi_{\rm shot} = \frac{\delta P_{\rm shot}}{dP_{\rm AS}/d\varphi_-} = \sqrt{\frac{h\nu}{2P_{\rm BS}}}, \tag{2.16}$$

where this last quantity has units of radians/$\sqrt{\rm Hz}$. The shot noise limit will improve as the square root of the power incident on the beamsplitter. For LIGO, which uses a $\lambda = 1.064$ µm laser, the shot noise in units of displacement noise (m/$\sqrt{\rm Hz}$) will be

$$\delta x_{\rm shot} = \frac{\delta\varphi_{\rm shot}}{k} \simeq 7{\rm x}10^{-17}\sqrt{\frac{1{\rm W}}{P_{\rm BS}}}. \tag{2.17}$$

The coupled cavity created when using power recycling can be arranged to have an extremely narrow linewidth, $f_{\rm cc} < 1Hz$, providing very effective filtering of noises on the input laser. This incurs no penalty by attenuating astrophysical strain signals, since they produce differential phase shifts and are therefore not recycled.

A recycling mirror can also be placed between the anti-symmetric surface of the beamsplitter and the dark port readout, in this case known as a *signal recycling mirror* [36]. When both recycling techniques are employed, the interferometer is said to be *dual-recycled*, see Figure 2.5. The cavity formed by the signal recycling mirror and the Fabry-Perot Michelson allows for gain-bandwidth tuning of the differential arm sensitivity, by tuning its length to be resonant or anti-resonant for the carrier light, or somewhere in-between.

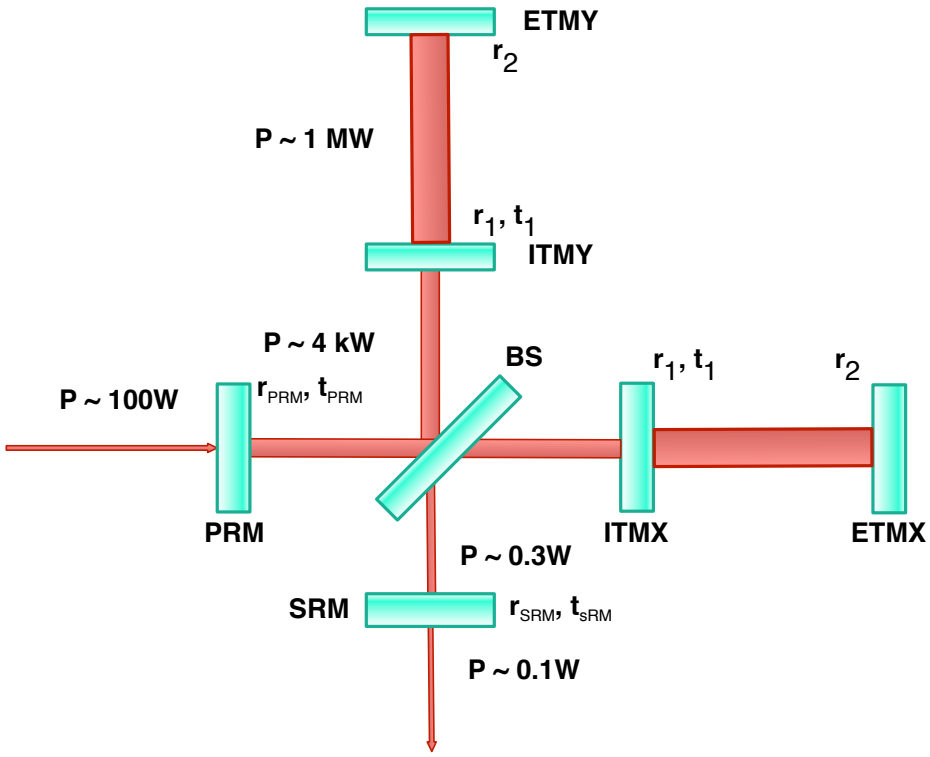

FIGURE 2.5. Cartoon of a dual-recycled Michelson interferometer with Fabry-Perot arms. Similar to the PRFPMI, with the addition of the SRM (signal recycling mirror), between the readout port and the beamsplitter.

At the present, unless targeting a specific source with a narrow expected frequency, the best option for current detectors is the case of a resonant signal recycling cavity, which results in an anti-resonant coupled cavity for signals with the reflection phase shift from the arm cavities (although more properly referred to as signal *extraction*, in practice this extra mirror is still referred to as signal *recycling* for the anit-resonant case). While this increases the detector bandwidth, it comes at the cost of low frequency gain, but since current detectors are limited by displacement, not sensing, noises at these frequencies this trade-off is acceptable. Tuning the signal recycling cavity (SRC) length, or optical phase, $\varphi_{\rm src}$, modifies the transfer function of the detector response to differential strains following the formula [37]

$$T(\omega) = \frac{t_1 t_{\rm srm} e^{-i(\omega\tau_{\rm arm}+\omega\tau_{\rm src}+\varphi_{\rm src})/2}}{1 - r_1 r_2 e^{-i\omega\tau_{\rm arm}} - r_1 r_{\rm srm} e^{-i(\omega\tau_{\rm src}+\varphi_{\rm src})} + r_2 r_{\rm srm}(1-{\rm loss}){\rm e}^{-{\rm i}(\omega\tau_{\rm arm}+\omega\tau_{\rm src}+\varphi_{\rm src})}}, \tag{2.18}$$

where ω is the signal's angular frequency, $t_{\rm srm}$ and $r_{\rm srm}$ are the field transmission/reflectivity of the signal recycling mirror, and $\tau_{\rm arm}$ and $\tau_{\rm src}$ are the round-trip travel times of the arm cavity and signal recycling cavity, respectively. $T(\omega)$ relates the relative power fluctuation at the signal port to the strain, normalized by input power. This formula ignores the frequency response of the signal recycling cavity by itself, but this is not important in the relevant frequency band, since the SRC is relatively quite short. A plot of this function for a variety of cavity detunings is shown in Figure 2.6.

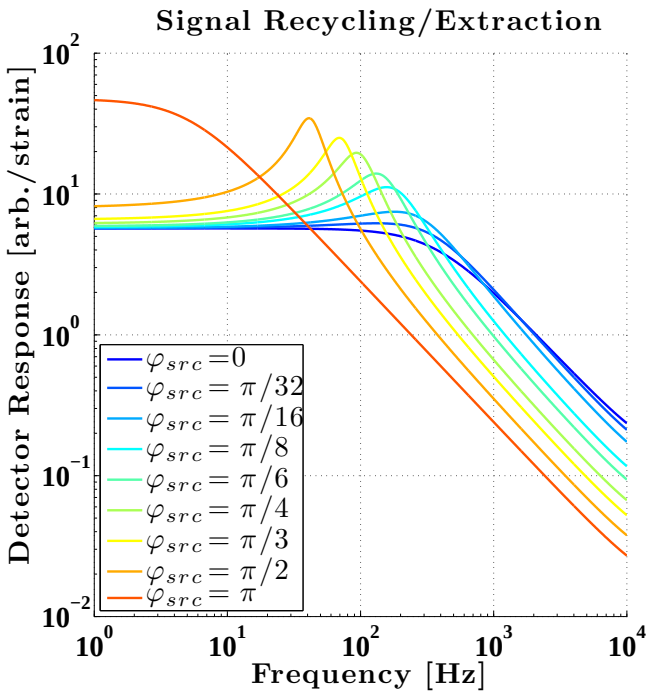

FIGURE 2.6. Frequency response of a signal recycled interferometer, with similar parameters to aLIGO, as the SRC phase is tuned from signal recycling (maximum DC response) to signal extraction (maximum bandwidth).

2.3 Noises

In general, noises impair the detector's performance either by confusing the phase measurement (*sensing noises*), or by preventing the mirrors from acting as inertial test masses (*displacement noises*). A brief description of some of the main noise sources from each type follows, with this information being generally true of any interferometric gravitational wave detector, but specifically referring to the case of Advanced LIGO. Displacement noise limits on the strain sensitivity scale as the inverse of the interferometer arm length. Below about 10 Hz, displacement noises are dominated by vibrations of the mirror support, driven by seismic motion. The feedback control forces used to overcome seismic disturbances also produce displacement noises, due to the self-noises of the various sensors and actuators required. These problems will be discussed in following chapters, as well as how the mirrors are isolated from these effects.

Around 100 Hz seismic noise is heavily attenuated, and the remaining displacement noise is chiefly from thermal (Brownian) motion of the mirror substrates, the wires/fibers which hold them, and the reflective coatings. The manner in which lossy (dissipative) mechanisms create thermal displacement noises is described by the fluctuation-dissipation theorem [38, 39, 40], which tells us that a mechanical oscillator with one degree of freedom will experience a fluctuating force spectral density defined by

$$F = \sqrt{\frac{4k_{\mathrm{B}}Tm\omega_0}{Q}}, \tag{2.19}$$

where k_{B} is Boltzmann's constant, T is the temperature of the oscillator, $\omega_0 = 2\pi f_0$ is its fundamental frequency, and Q is its "quality factor", a measure of how damped the system is, one relation being $Q = f_0/\Delta f_{\mathrm{FWHM}}$. Thermal noise from

the suspensions and mirror substrates can be mitigated by using low loss (high Q) materials, keeping the suspension wires/fibers thin at the ends, and by engineering their resonant modes to be at frequencies outside of the detection band. Finding low loss materials for the reflective coatings has historically been problematic, and this is expected to be the dominant contribution from thermal noises to current detectors, as well as a limiting noise source overall around 100 Hz [41]. Also, all thermal noises can of course be reduced by lowering the temperature to the apparatus, and there are past prototypes, and future plans, for using cryogenic detectors [42, 43].

From f ∼100 Hz and higher, sensing noises are dominated by photon shot noise, mentioned previously as the motivation for power recycling. Apart from higher input laser power or more power recycling gain, there is also the possibility of injecting squeezed light into the anti-symmetric port of the interferometer to improve the shot noise limit by redistributing quantum noise from the phase quadrature to the amplitude quadrature [48, 49, 50]. This will increase quantum radiation pressure noise, caused by power fluctuations in the laser beam reflecting off the mirrors producing a fluctuating pressure, but trade-offs may be acceptable (or a frequency dependent squeezing may be applied [51]). Other sensing noises include scattering of light out of then subsequently back into the main laser field [52, 53], forward scattering off of residual gas molecules in the arm cavities, noises in the readout electronics, laser frequency, laser amplitude, and phase noise in the RF oscillators used to generate the sidebands for feedback control.

2.3.1 First and Second Generation Terrestrial Interferometers

The LIGO laboratory operates two observatories, one situated in Hanford, WA, and the other in Livingston, LA. The distance between detectors is ∼3000 km,

corresponding to a light travel time of ∼10 ms. One interferometer with 4 km long arms, referred to as L1, can be housed at the Livingston site (LLO), while the Hanford site (LHO) is equipped for two, and in the past did house one 4 km and one 2 km detector, known as H1 and H2, respectively. To date, all LIGO detector generations have been installed in their original ultra-high vacuum envelopes, with the enclosed volume being $\sim 25 \times 10^6$ liters.

While the first generation LIGO detectors continually improved their sensitivities and duty cycles over six science runs (S1-S6), historically their operation is broken into just two phases: Initial LIGO (iLIGO), and Enhanced LIGO (eLIGO). Only the last science run, S6, took place in the eLIGO era, running from July 2009 until October 2010. This incorporated an incremental upgrade to iLIGO while preparations for the second generation, Advanced LIGO (aLIGO) were underway. Both iLIGO and eLIGO used the power-recycled Fabry-Perot Michelson topology, with 10's of W of input power, 10 kg test masses, and a sensitive band from ∼80 Hz to a few kHz [54]. The major difference between iLIGO and eLIGO was the shift from an RF detection scheme to DC readout [58], aided by the introduction of an Output Mode Cleaner (IMC) at the dark port [59]. Other detectors around the world which operated during the first generation include VIRGO, in Tuscany [55], GEO600 [56], in Lower Saxony, and the TAMA 300 detector in Tokyo [57].

The second generation of detectors, currently being constructed, installed, and commissioned, include not only aLIGO [60], but Advanced VIRGO [61], and KAGRA [43]. A cartoon showing the light travel times between planned second generation detectors is shown in Figure 2.7. So many detectors spread over such large baselines serves to improve sky-localization accuracy [62]. Advanced LIGO is a nearly comprehensive overhaul, including larger masses (40 kg), more laser power ($>$ 100 W), and extensive isolation improvements from 1 Hz up. The topology

has also evolved, from a power recycled to a dual recycled Fabry-Perot Michelson. The targeted sensitivity is ∼10x more than eLIGO, a factor of 1000x in sensed volumed, with a bandwidth extending down to 10 Hz.

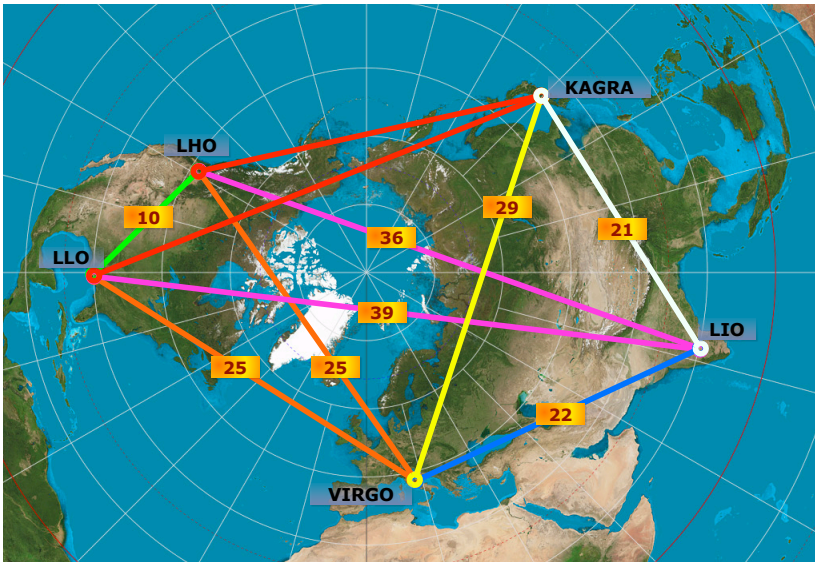

FIGURE 2.7. Approximate locations of planned second generation detectors, as well as the signal travel time between them, in ms. "LIO" refers to a proposed third aLIGO detector (enough hardware was created for three instruments), located somewhere in India, and its position on this chart is meant as a rough guess.

There are plans beyond this generation of terrestrial interferometers, including the sub-terranean Einstein Telescope [44]. Also, it should be mentioned that space-based interferometers have long been studied and proposed, such as LISA (now called the New Gravitational-wave Observatory (NGO)) [45], although none have launched yet. It should be pointed out that LISA chief sensitivity will be at frequencies considerably lower than, and indeed almost certainly out of the reach of, terrestrial interferometers (sub-Hz). There are also entirely different kinds of detections, including the use of pulsar timing arrays [46] to detect ultra-low frequency ($\sim 10^{-8}$ Hz gravitational waves, and investigations into the polarization of the cosmic microwave background to detect gravitational waves of cosmological origin [47].

2.4 State of the Art

Figure 2.8 shows a representative displacement sensitivity for the L1 interferometer during S6. Above ∼150 Hz the performance is limited by shot noise, below this a variety of technical noises relating to the control systems as well as residual seismic noise dominate. A common figure of merit for detector performance is the "inspiral range", which is the distance from which a binary neutron star (BNS) inspiral waveform, with component masses of 1.4-1.4 $M_{\odot}$, could be detected with a SNR of 8. Currently, the relevant unit is *megaparsec* (Mpc), that is 10^6 parsec or about $2x10^{19}$ miles. The maximum range achieved during S6, for both L1 and H1, was ∼20 Mpc, for ∼15 W of input power. The black trace ("science requirement") in Figure 2.8 was the stated sensitivity goal for initial LIGO, which was achieved at all frequencies which contribute significantly to binary neutron star inspiral reach. Despite this, modeled signal rates for S6 predicted a small chance (1 in 50 years of data) of detection with the eLIGO instruments (which collected a little less than a year of coincident data), and the chief purpose was as a technology demonstration before proceeding to Advanced LIGO.

Figure 2.9 contains a model noise budget for the aLIGO detectors, created using the GWINC software package for MATLAB [63, 77]. Only a subset of noise predictions are shown, which include the sensitivity limiting contributions of quantum noise, coating thermal noise, and seismic noise. Also, this choice of input power and SRC detuning (lack of detuning, more accurately) is only one mode of operation available, and most likely earlier science runs will take place at a lower power, lower sensitivity state [64]. In this projection, suspension thermal noise is only truly limiting at the vertical, or "bounce", mode of the test mass suspesions, around 9 Hz, as well as the very high Q violin peak, around 500 Hz. While there

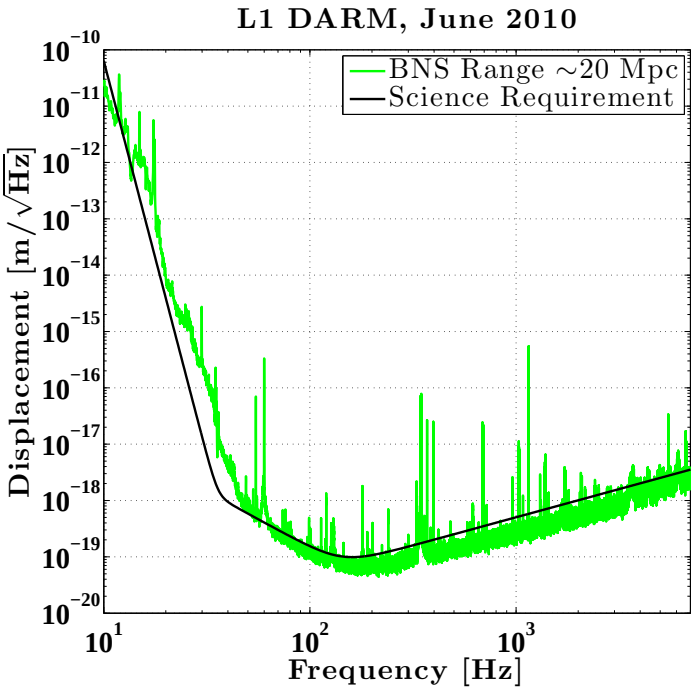

FIGURE 2.8. Above ~150 Hz the eLIGO interferometers were shot noise limited. While the phase noise spectral density of shot noise is white, the strain sensitivity degrades as f due to the arm cavity pole (~80 Hz for eLIGO). The sharp up-turn in noise below 50 Hz is referred to as the "seismic wall". Lines at 51, 396, 404, and 1150 Hz are calibration injections, and the group around 400 Hz correspond to the "violin" modes of the suspension wires.

is a clear path, mentioned in previous sections, for improving the shot noise limit, it is also clear that a corresponding improvement in the coating thermal noise's contribution to the strain readout must be devised to proceed beyond aLIGO. A prediction for the likely rates of binary coalescences in the aLIGO era is ~40 per year [65].

Figure 2.10 shows the sensitivity of the Livingston detector around the time this thesis was written (still during a period of full-time commissioning). Full power operation was not available, instead about 10 W is injected to the detector, and the inspiral range around 36 Mpc at the best of times.

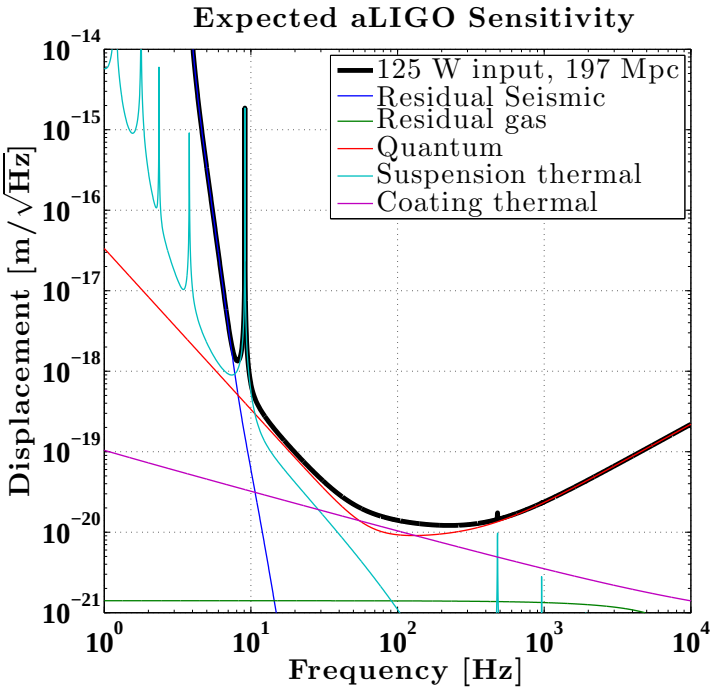

FIGURE 2.9. Expected aLIGO performance. The total noise, in black, is calculated for 125 W of power into the interferometer, and 80 ppm round trip losses (each arm, no mismatch). This corresponds to an inspiral range of ∼200 Mpc. The most sensitive frequency band is around ∼100 Hz, referred to as the "bucket", where the limiting noise sources are the coating thermal noise, and quantum noise (shot noise and radiation pressure meet at round this frequency with this input power).

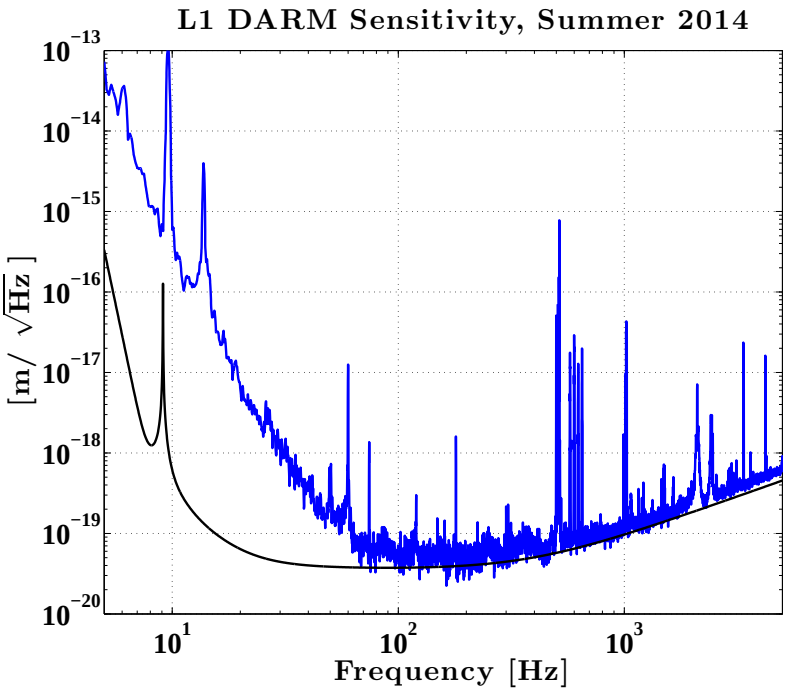

FIGURE 2.10. Contemporary performance of the Livingston interferometer, with $P_{\text{in}} = 10$ W, and an inspiral range of ∼36 Mpc (calibration preliminary).

3

Vibration Isolation

In order to sense such small displacements as those laid out in the previous chapters the test masses must be isolated from the vibrations of the ground. At most locations on the Earth the motion of the ground neatly separates into three categories, with corresponding frequency bands. At ∼1 Hz and above, surface vibrations dominate and are generated by two different sources, both of which follow a day-night cycle:

- Human activity, for instance the operation of motor vehicles and trains, or logging
- High, gusting winds which push on buildings, trees, or other obstructions

At night, when both these disturbances have abated, the seismic motion falls off roughly as $1/f^2$, with a level of $\sim 10^{-8} \frac{\mathrm{m}}{\sqrt{\mathrm{Hz}}}$ at 1 Hz being typical for the Livingston site. The day-time increase can be 5x to 10x the ambient level. This means that in the detection band the test mass inertial motion should be at least $\sim 10^8$x less than the input from the ground, a stringent requirement which informs the design of the isolation system.

Even if the mirrors are isolated well enough to achieve design sensitivity at ∼100 Hz, some feedback force will always be required to keep the optical cavities on

resonance. Several noise coupling terms put constraints on the degree to which the cavity lengths must be stabilized. Feedback actuation can be achieved by attaching small magnets to the backs of the mirrors, such that current running through a nearby coil of wire exerts a magnetic force on the mirror. This is how all mirrors were actuated during iLIGO and eLIGO, and for aLIGO this is used for most mirrors, except the test masses themselves which are driven with an electrostatic force.

Between ∼0.1 and ∼1 Hz the ground motion is dominated by the "microseism", seismic waves generated by complex interactions of water waves in the oceans and other large bodies of water. The microseism is a persistent disturbance, and is composed of both a "primary" and "secondary" microseisms, the first being peaked in frequency around 75 mHz and the second the double-frequency of that. In the absence of earthquakes, the secondary microseism is the largest ground disturbance a seismic isolation system faces, with quite a large variation from season to season (winter being the worst), or in the presence of severe weather (sometimes a serious concern in Louisiana!). At the Livingston site the height of the microseismic peak varies by about 2 orders of magnitude, from a few 100's of $\mathrm{nm}/\sqrt{\mathrm{Hz}}$ to 10's of $\mu\mathrm{m}/\sqrt{\mathrm{Hz}}$.

Below 0.1 Hz the seismic spectrum is usually less active than the higher frequency bands, except in the presence of earthquakes. Wind activity can also manifest itself as signals in this band, although not by creating a real seismic disturbance but instead by tilting the inertial sensors used to measure the ground (seismometers), an interaction that will be discussed later in this chapter. Also worth mentioning is the very long period (∼12 hours) tidal strain caused by the Earth-Moon-Sun system [66], which the isolation system may be asked to compensate. A spectrum of the ground motion is displayed in Figure 3.1, with measurements from LIGO

Livingston taken at different points in the day and year. Long-term statistical analyses of the ground motion variation at both LIGO sites can be found in [67], and for a number of sites around the world in [68].

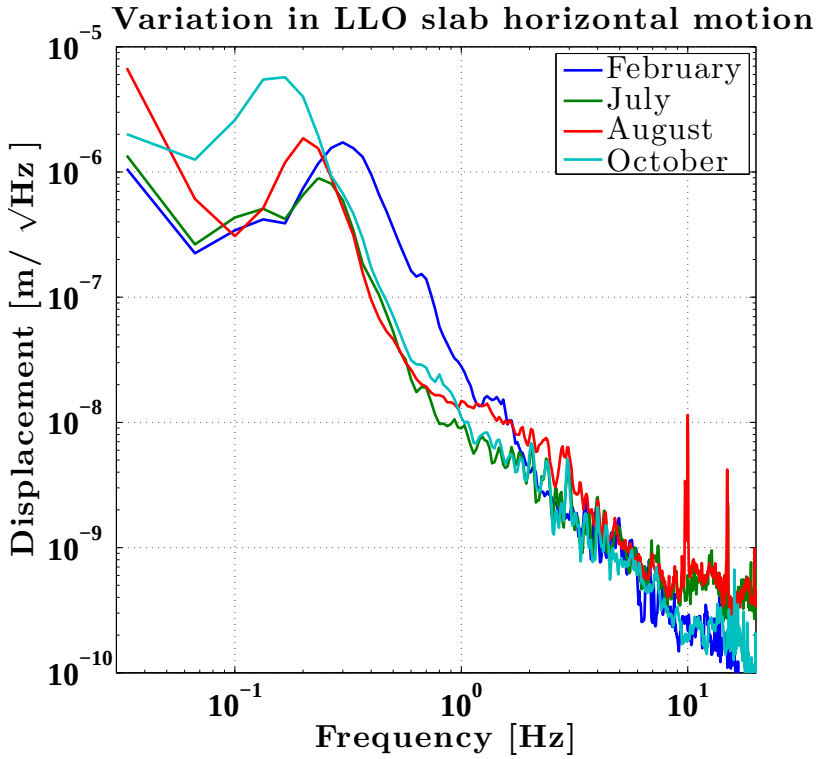

FIGURE 3.1. Example seismic spectrum showing several possible environments. The curve labelled February displays a particularly high frequency but median amplitude microseismic peak, as well as some elevated day-time motion around 1-2 Hz. The seismic noise in the July curve is low at most frequencies which is typical of the summer. The August curve was at a time of high winds, which create excess above 1 Hz and also a lot of tilt below 0.1 Hz. The October curve shows the winter-time microseismic excess.

The following sections will describe passive and active isolation schemes, both which are used in LIGO, review their performance as well as some of the difficulties they face.

3.1 Passive Isolators

A passive isolation system works by transmitting energy more and more poorly as the frequency of the disturbance extends above the natural frequency, f_0, of

the isolator. The natural frequency of the isolator is usually determined by the isolator's geometry or construction, the length of a pendulum for instance, as is the case of LIGO. The trade-off for high frequency isolation is that at f_0 any input disturbance will be amplified to some extent. Among other technical difficulties, the sensitivity of conventional inertial sensors limits the degree to which active isolation can perform, necessitating a passive isolation system to bridge the gap between ground motion and the detector's design sensitivity. Conversely, since the natural frequency of a pendulum decreases only as $1/\sqrt{l}$, l being the length of the pendulum, providing low frequency (microseism) isolation passively has technical difficulties of its own: even a 40 m tall pendulum would only provide a factor of few reduction at 0.2 Hz.

The transmission of motion of a pendulum resembles the left panel of Figure 3.2, where a $1/f^2$ slope attenuates the input disturbance above f_0. In the frequency domain it is described (omitting some subtleties described in the Appendix) by the transfer function

$$H(\omega) = \frac{\omega_0^2}{\omega_0^2 - \omega^2 + \frac{i\omega\omega_0}{Q}}. \tag{3.1}$$

Suspending multiple masses successively as pendulums, with similar resonance frequencies, results in a coupled system which isolates input motion as $1/f^{2N}$, for N stages, above the highest resonant frequency. In iLIGO the test mass mirrors were suspended as single stage pendulums, but for aLIGO they are suspended from quadruple chains, the modeled transmission of which is shown in the right panel of Figure 3.2.

Despite the awesome power of the aLIGO passive isolators, at 10 Hz the attenuation of 10^7 and ground motion of $\sim 10^{-10}$ m/$\sqrt{\text{Hz}}$ leave a few orders of magnitude

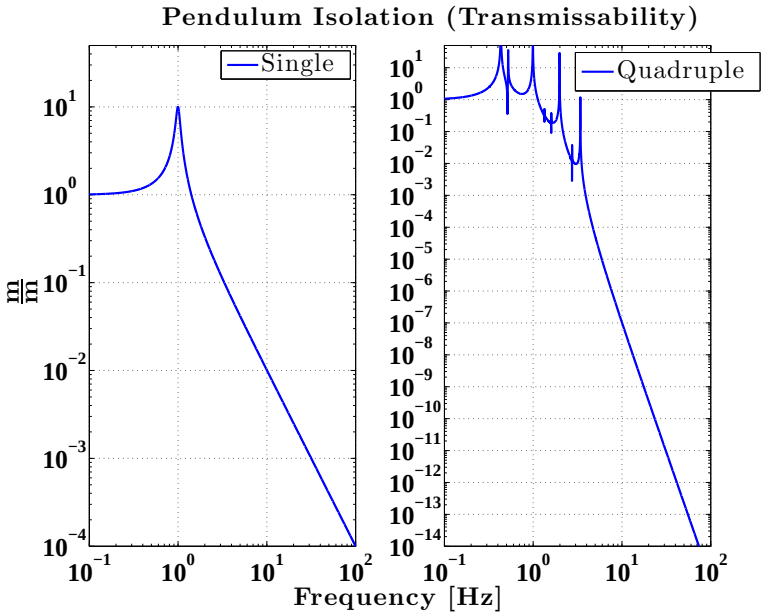

FIGURE 3.2. Single and multiple pendulum isolation transfer functions, relating the motion of the suspended mass to the motion of the suspension point. The sharp features on in the right panel, in between the four main pendular resonances, are residual effects of cross coupling from other degrees of freedom.

in isolation to be contributed by the active isolation systems. Also, in order to achieve robust and simple (where possible) controls of the interferometric degrees of freedom (both length and angle), the rms motion of the test masses should be reduced as much as possible by the active platforms.

3.2 Tilt-Horizontal Coupling

All of aLIGO's active isolation systems contain horizontal inertial sensors, and a recurring topic when working with these instruments at low frequencies ($f < 0.5$ Hz) is tilt-horizontal coupling [69]. At the heart of an inertial sensor is a proof mass referenced to a housing or cage, with its motion decoupled by the use of an elastic element like a spring or flexure. The apparent force between the housing and the proof mass has two terms:

$$F = m\ddot{x} - mg\cos\theta, \tag{3.2}$$

where m is the mass of the proof mass, $\ddot{x}$ the horizontal inertial acceleration of the housing, g is the acceleration constant of gravity (at the surface of the Earth), and θ is the angle formed between the sensor's axis and the direction of the local gravitational force. If the alignment of the sensor is composed of a static orientation, θ_0, and its variation due to ground tilt, $\delta\theta$, then the incremental change in force becomes

$$\delta F = m\ddot{x} + mg\ \delta\theta\ \sin\ \theta_0. \tag{3.3}$$

The orientation of the sensor therefore determines its sensitivity to tilts: for a vertical inertial sensor the instrument axis is aligned with gravity, i.e. $\theta_0 = 0$ and the sensitivity to small orientation deviations vanishes. For a horizontal inertial sensor, however, $\theta_0 = \pi/2$, and the sensitivity to orientation deviations remains,

$$\delta F_{\text{horiz.}} = m\ddot{x} + mg\ \delta\theta. \tag{3.4}$$

The relative contributions to the sensor output from these two terms is clear when examining Equation 3.4 in the frequency domain:

$$\delta F(\omega)_{\text{horiz.}} = -m\omega^2 x(\omega) + mg\ \delta\theta(\omega), \tag{3.5}$$

giving the relation for the equivalent displacement signal, $x(\omega) = -\frac{g}{\omega^2}\delta\theta(\omega)$. Due to the $1/\omega^2$ frequency dependence this term only confuses the inertial sensor output at low frequencies, typically becoming the dominant signal starting at $f \simeq 0.03$-0.1 Hz (with the variation due to the amount of variation in the seismic environment). Below this frequency the horizontal inertial sensors are acting, unintentionally, as inertial tilt-meters. The proximity in frequency space of the microseismic disturbance and the pollution of tilt presents a significant (perhaps the *most* significant)

challenge for active control systems with requirements like those of aLIGO, and as such this topic will be referred to repeatedly in the following sections.

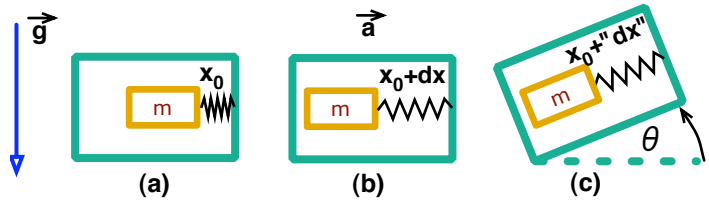

FIGURE 3.3. An inertial sensor formed by a proof mass, m, coupled to a cage by a spring, in three scenarios. In scenario (a), the cage is at rest with respect to inertia, and the mass maintains a fixed distance x_0 from it. In scenario (b) the cage is accelerated, perhaps by the motion of the ground at the cage's location (i.e. a seismometer), and the inertia of the proof mass creates a relative force on the spring element, sensed as a displacement dx. In scenario (c) an equivalent signal dx is generated, not by linear acceleration of the sensor with respect to inertia, but by a change in the sensor alignment, θ, with respect to local gravity.

3.3 Sensor Blending and Control Topology

Another common thread in all aLIGO active isolation systems is the combined use of relative position sensors and inertial sensors, a process known as "sensor blending" or "sensor fusion" [71]. Position sensors allow for DC coupled controls, so the alignment of the isolation platform can be stabilized against drifts in temperature, up to the level at which the sensors themselves drift. The inertial sensors are not sensitive at low frequencies, but when placed on the isolation platform can be used to quiet the payload motion with feedback, or with feed-forward when placed on the support stage (or ground).

Assuming one relative position and one inertial sensor will form the error point of the control loop, two filters, one low-pass and one high-pass filter, are needed to combine them, called the "blend filters". The frequency at which these two filters have equal magnitudes is called the "blend frequency". After filtering and summation the combined sensor is called the "super sensor". A simplified schematic

of the control topology for this scenario is shown in Figure 3.4, and with a few more details this is a useful tool for all of the isolation systems discussed in the following sections, where each of the six degrees of freedom (DOFs, 3x translations and 3x rotations) will have an equivalent signal flow. An important caveat is that this model assumes the mechanics of the isolator's sensing and actuation have been diagonalized enough to work with SISO controllers for each DOF. In general this is not true, and the details of each individual isolation system will be discussed separately in later sections.

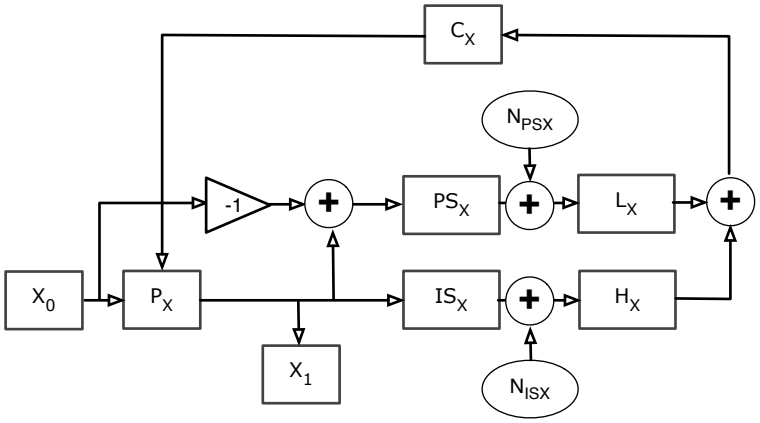

FIGURE 3.4. Abbreviated version of a two sensor blended control loop. X_0 is the input motion, P_{X} is the mechanical response of the isolation stage, X_1 is the motion of the isolated platform, IS_{X} and PS_{X} are the frequency responses of the inertial sensor and position sensor, respectively, L_{X} and H_{X} are the low-pass and high-pass blend filters, respectively, and C_{X} is the controller. $N_{\mathrm{PS_X}}$ and $N_{\mathrm{IS_X}}$ are the self-noises of the position and inertial sensors.

The open loop gain (OLG) of this system is the product

$$G(\omega) = P_{\mathrm{X}}(\omega)\ \left[H_{\mathrm{X}}(\omega)IS_{\mathrm{X}}(\omega) + L_{\mathrm{X}}(\omega)PS_{\mathrm{X}}(\omega)\right]\ C_{\mathrm{X}}(\omega), \tag{3.6}$$

and if we write the equation for the platform motion (dropping the ω for ease) we find

$$X_1 = \frac{-G}{1-G} L_{\mathrm{X}} \cdot X_0 + \frac{G}{1-G} L_{\mathrm{X}} \cdot N_{\mathrm{PS_X}} + \frac{-G}{1-G} H_{\mathrm{X}} \cdot N_{\mathrm{IS_X}} + \frac{P_{\mathrm{X_0 \to X_1}}}{1-G} X_0. \quad (3.7)$$

The goal of the control scheme is to make X_1 as small as possible. Note that, in the limit of no controls (i.e. $G \to 0$), the platform motion is simply the input motion filtered by the mechanical response of the system, $X1 = \frac{P_{X_0 \to X_1}}{1-G} X_0$. Also note that, at frequencies where the loop gain is large ($\frac{G}{1-G} \to 1$), until the sensor noises become limiting the platform motion will simply be the input motion filtered by the blending low-pass, $X_1 = L_{\mathrm{X}} \cdot X_0$.

When seismometers on the support stage, or the ground, are used in the isolation scheme it is either via summation into the control signal, referred to as feed-forward, or by summation into the error point, referred to as "sensor correction." The sensor correction term is sourced from the typical implementation of this technique in the context of LIGO: using a low-frequency inertial sensor on the ground summed into the position sensor signal in the blend. The control loop then locks the platform to inertia in a wider band. A new term must be added to the platform motion to account for this path, $X_0 L_{\mathrm{X}}(1 - SC_{\mathrm{X}})G/(1-G)$, where $SC_{\mathrm{X}}(\omega)$ is the sensor correction filter.

The chief benefit to feed-forward, in contrast to feedback, is that it is an inherently stable control scheme, since the witness sensor signal is not altered by the actuators. The chief difficulty is that the performance is dependent on the accurate calibration and matching of the sensors involved, since both feed-forward and sensor correction are essentially subtraction schemes.

In Equation 3.6 it is clear that the sum of the blend filters directly alters the complex loop gain and therefore must obey some stability constraints. Assuming the blend filters include compensation for their individual sensor's frequency responses,

then the control stability problem can be separated from the noise management problem by requiring that the blend filters contain no right-half plane poles and be complementary,

$$H_{\mathrm{X}}(\omega) + L_{\mathrm{X}}(\omega) = 1, \tag{3.8}$$

or at least approximately so. In general, the blend filter design should satisfy several more criteria:

- Above the blend frequency, the low pass filter should have enough attenuation to allow for servo control to reduce the residual seismic motion to the level of the platform sensor noise
- Below the blend frequency, the high pass filter should have enough attenuation to limit the transmission of low frequency inertial sensor noise or tilt (this is in direct competition with the above criteria due to the blend filter sum stability constraints)
- Around the blend frequency, the phase of the normalized blend filters ($\frac{LP}{HP+LP}$ and $\frac{HP}{HP+LP}$) should not create too much gain peaking or an ill-conditioned impulse response

While all 6 rigid body degrees of freedom have similar control topologies for the aLIGO isolation systems, the tilt-horizontal coupling mechanism discussed in the previous section enhances the complexity of the horizontal degrees of freedom, which are also the most important from the interferometry point of view. A more complete diagram of the control topology for these DOFs is shown in Figure 3.5. Correspondingly, the equation for the horizontal platform motion is modified to include these terms,

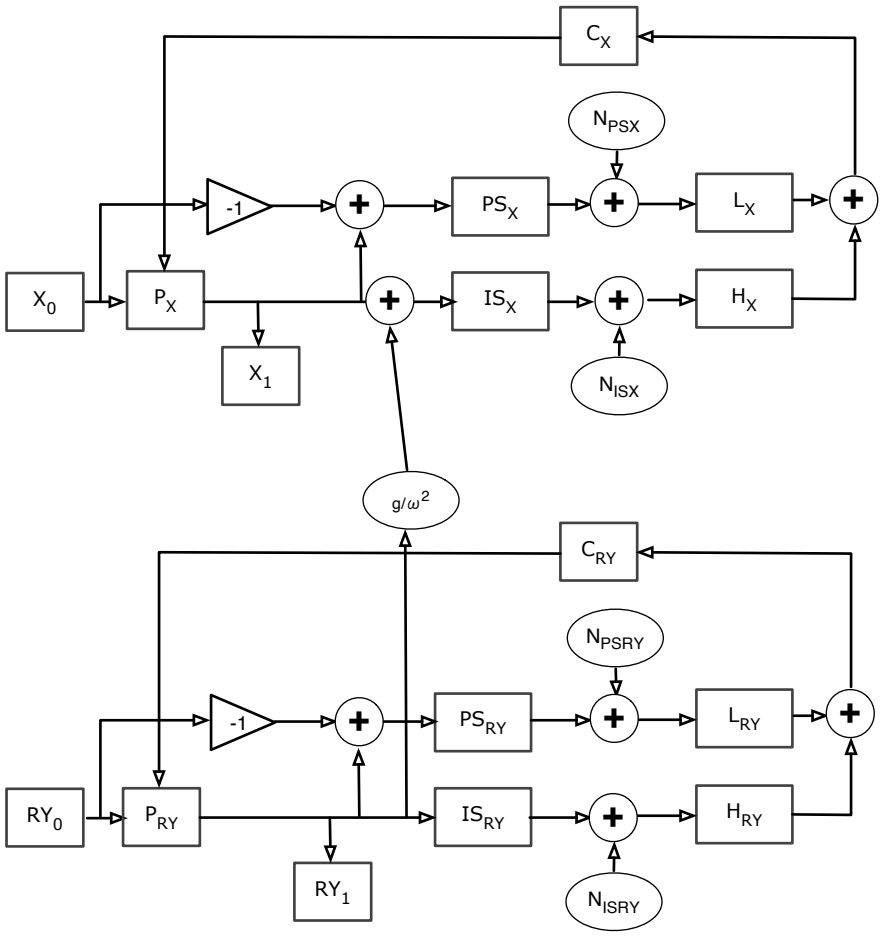

FIGURE 3.5. A more realistic schematic of a two sensor blended control loop, where tilt horizontal coupling is included.

$$X_1 = \frac{-G}{1-G} L_{\mathrm{X}} \cdot X_0 + \frac{G}{1-G} L_{\mathrm{X}} \cdot N_{\mathrm{PS_X}} + \frac{G}{1-G} H_{\mathrm{X}} \cdot N_{\mathrm{IS_X}} + \frac{P_{\mathrm{X_0 \to X_1}}}{1-G} X_0 + \frac{G}{1-G} H_{\mathrm{X}} \cdot RY_1 \tag{3.9}$$

where RY_1 indicates the platform tilt motion, which follows an analogous formula to Equation 3.7. There is another platform tilt consideration in that none of the active isolators' sensor/actuator planes are aligned with the suspension point planes of their payloads. The resulting lever arms produce direct tilt to horizontal couplings, which can be significant in the 1-10 Hz band, necessitating a balance between this effect, $RY_1 \cdot \delta z_{\mathrm{lever}}$, and $\frac{G_{\mathrm{X}}}{1-G_{\mathrm{X}}} H_{\mathrm{X}} \cdot \frac{G_{\mathrm{RY}}}{1-G_{\mathrm{RY}}} H_{\mathrm{RY}} N_{\mathrm{IS_{RY}}}$.

3.4 Active Isolators in Advanced LIGO

There are three active isolation systems in aLIGO, one which is deployed outside of the vacuum system and two different kinds which can be deployed inside: In-Vacuum Seismic Isolators (ISIs), single stage in a HAM, two stages in a BSC. HAM and BSC simply refer to the two different vacuum chamber geometries: Horizontal Access Modules (HAMs), and BeamSplitter Chambers (BSCs), although this second definition is often disputed (and searches through the LIGO acronym literature yield inconsistent results).

3.4.1 HEPI

The out of vacuum system is HEPI (Hydraulic External Pre-Isolator) [74, 73], and as the name implies is actuated with hydraulic valves supplied with high pressure fluid in each laboratory building (one circuit for all of the chambers in the corner station and one each for the end stations). Although technically an Advanced LIGO system, HEPI has been employed at LLO for the past ∼10 years, since there was a technical need and the system was ready for deployment at that time. The corner of each vacuum chamber has a HEPI pier, a drawing of which is shown in Figure 3.6, and an engineering drawing of a HAM chamber with HEPI is shown in Figure 3.7.

In each pier there are four key components,

- A pair of maraging steel "offload" springs, with $k \simeq 10^6$ N/m, which bears the static weight of the payload (∼2000 kg in a HAM, ∼5000 kg in a BSC) and can also be used for coarse positioning

- A hydraulic actuator, capable of moving the payload ±1 mm, outputting ∼1500 N

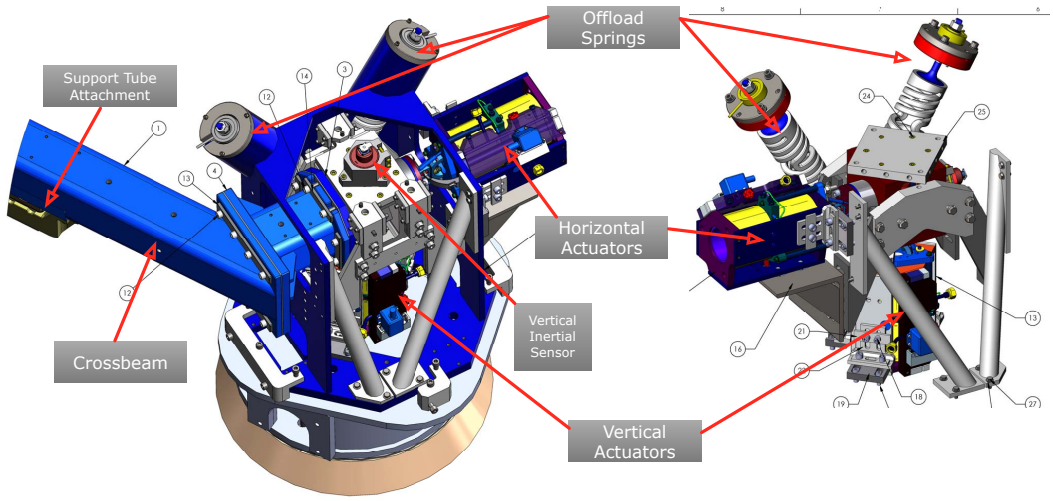

FIGURE 3.6. Engineering drawings of a HEPI corner or "pier", shown on the left with the housing and crossbeam included, and on the right with the housing removed to expose the offload springs. The position sensors and horizontal inertial sensor are not easily visible from these viewpoints.

- An inductive position sensor referencing the payload position against the support structure, the Kaman DIT-5200 with a noise floor of $\sim$3x10^{-10} m/$\sqrt{\text{Hz}}$

- An inertial sensor, the Sercel L-4C 1 Hz geophone, with a noise floor of $\sim$2x10^{-11} m/$\sqrt{\text{Hz}}$ at 1 Hz, falling off as $1/f$ above that and increasing as $1/f^3$ below that

Since there are 8 sensor pairs two over-constrained DOFs can also be sensed and controlled, referred to as the horizontal and vertical "pringles", since they correspond to deformations rather than translations or rotations. The offload spring resonance is around 8 Hz, and although it does not bear the static load the hydraulic actuator significantly alters the system dynamics due to both the significant damping providing by the hydraulic fluid and internal resonances of the actuator itself, in the region of 10's of Hz [70]. Two connections mate the suspended portion of the pier to the in-vacuum equipment,

- A cross-beam which hangs between piers, attaching at each end with an angle (30° on a HAM chamber, 45° on a BSC)

- Two support tubes, hanging beneath and clamping to the cross-beams, which enter the vacuum system through a metal bellows where they are bolted to the in-vacuum equipment's support plates

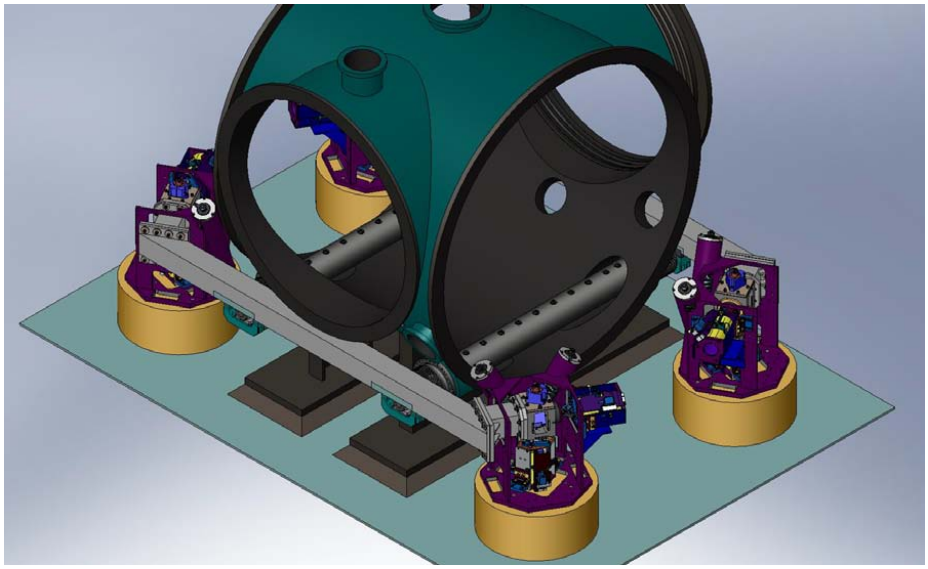

FIGURE 3.7. An engineering drawing of the HEPI system on a HAM chamber cutaway. The four gold cylinders are support blocks which ground the purple HEPI piers. The gray beam spanning between piers in the longer dimension is the cross-beam, and between cross-beams the hang the support tubes. The support tubes are shown entering and exiting the vacuum chamber, with the series of black dots representing the bolt holes where the in-vacuum equipment support plate is attached.

This structural support contributes to the dynamics of the HEPI plant, shown in Figure 3.8, where the compliance of the cross-beam produces complex pole/zero pairs around 10 Hz. The overall 1/f slope visible in the actuator to position sensor transfer functions is due to a ∼30 mHz pole in the actuator itself, which is very overdamped by the viscosity of the hydraulic fluid [70]. For position and alignment control the actuator response allows for a supremely simple feedback controller: merely a multiplicative constant. For inertial isolation the support dynamics and

unreliability of true plant inversion limit the bandwidth of HEPI control to ∼10-15 Hz, with an example shown in Figure 3.9.

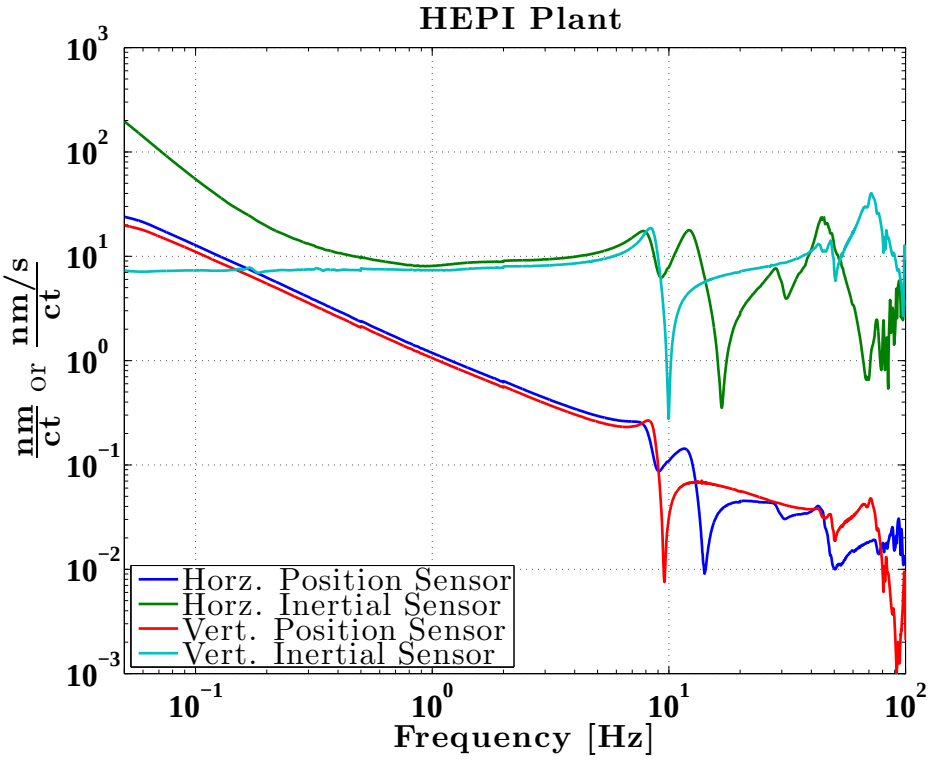

FIGURE 3.8. The response of the HEPI system's horizontal and vertical sensors to actuation. The discrepancy below 1 Hz between the horizontal and vertical inertial sensors' transfer functions is due to tilt deformation of the HEPI pier. Numerous features of the support structure are apparent starting around 10 Hz.

The roll-up in the horizontal inertial sensor is from tilt-horizontal coupling, where the tilt is generated by deformation under stress in the corner housing where the L4-C is placed. The crossover from useful signal to tilt corruption is so high (100's of mHz) that it must be corrected for in order to provide useful isolation in the 0.5-5 Hz region (the most critical due to the frequencies of the suspension resonances). The control topology for HEPI is therefore a modified version of Figure 3.4, where the output of the horizontal servo (i.e. horizontal force application) is used to predict the tilt signal and subtract it from the inertial signal portion of the blend. Figure 3.10 shows the inclusion of this extra internal feedback mechanism, which

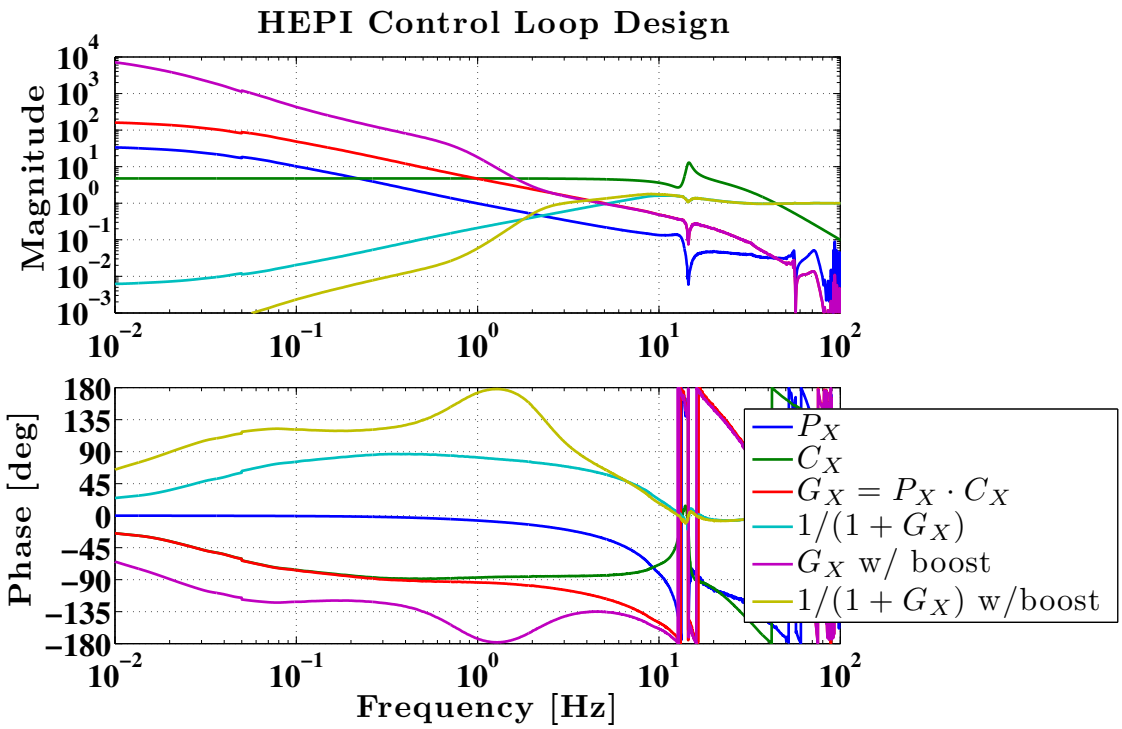

FIGURE 3.9. Frequency responses of the relevant components in a HEPI control loop. The compensator, C_X, partially inverts the plant features around 10 Hz and relies on the natural $1/f$ response of the actuator to provide an unconditionally stable loop gain, G_X. Once engaged, the low frequency servo gain is bolstered with at "boost" filter as well as a low frequency integrator, which pushes the loop into conditional stability (note the phase bubble around the 5 Hz upper unity gain frequency) but provides adequate suppression.

is referred to as the "twist" correction, since it stems from mechanical flexing in the pier housing.

Typically HEPI is also used with sensor correction, using a Streckeisen STS-2 seismometer placed on the technical slab. This sensitivity at low-frequency of this device ($\sim 10^{-9}$ nm/$\sqrt{\text{Hz}}$ at the microseism, increasing as f^{-2} below that) complements the L4-C's on the HEPI payload, which can then be blended in around 300 mHz. Inevitably the STS-2 is susceptible to tilt of the slab below 100 mHz, and to combat this a polyphase FIR cutoff filter was designed [71, 72] to:

- Attenuate with a slope of f^3 below 40 mHz, down to 8 mHz, where it flattens out (the STS-2 response attenuates as f^2 below 8 mHz)

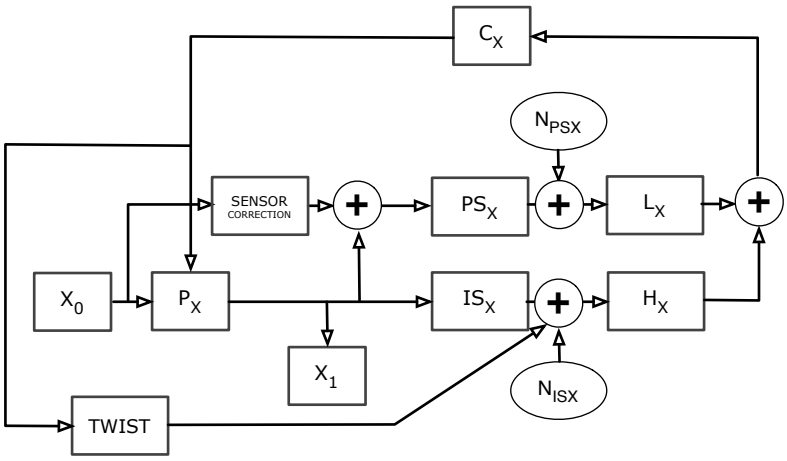

FIGURE 3.10. Control topology for a HEPI system where pier deformation correction is included, as is the sensor correction path.

- Amplify by no more than 3x between 40 mHz and 100 mHz
- Match gain and phase well above 100 mHz, such that the 10x isolation is providing around the microseism

Figure 3.11 shows the frequency response of this FIR high-pass, as well as the expected isolation from ground motion, assuming perfect sensor calibration and matching. The features every 2 Hz are artifacts of the polyphase architecture, which keeps the number of FIR taps required manageable by being effectively sampled at this frequency. These artifacts are filtered out in practice and no not pose a problem.

The performance of a HEPI system as described so far is shown in Figure 3.12. Unfortunately, for HAM chambers the performance below $\sim$0.5 Hz comes at the cost of some unintended tilting of the in-vacuum payload. Force application to the corners of the HEPI cross-beam also produces some deformation, such that pushing on one beam and pulling on the other (to cancel horizontal motion) bends one beam up and the other down, rotating the support tubes and the ISI inside, Figure 3.13 is a cartoon of this effect. The magnitude of the effect is approximately

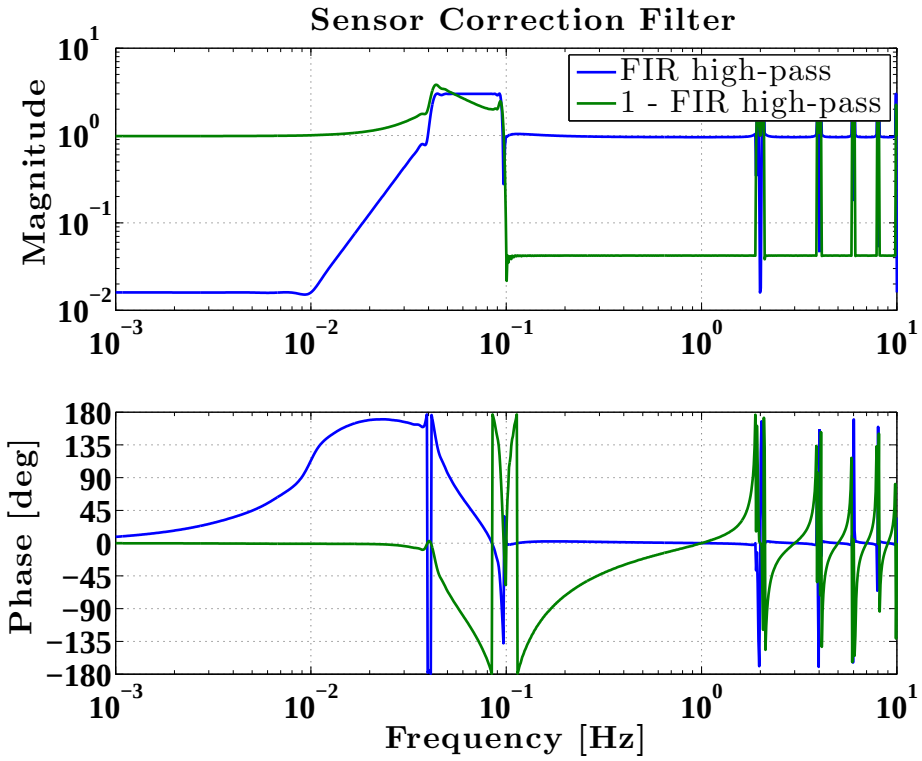

FIGURE 3.11. Polyphase FIR filter used to prevent low frequency tilt injection when using sensor correction. See [71] for full details on the filter design.

0.1 rad/m, so a typical microseism of $\delta x \simeq$ a few µm/$\sqrt{\text{Hz}}$ produces $\delta\theta \simeq$ of a few 100 nrad/$\sqrt{\text{Hz}}$, which is sensed by the ISI's horizontal inertial sensors as $\delta x = g/\omega^2\ \delta\theta \simeq$ a few µm/$\sqrt{\text{Hz}}$ at 0.15 Hz: the ISI does not witness any isolation, as is shown in Figure 3.14. The blend frequency on the ISI needs to be low enough to provide isolation at the suspension resonances, which start around 0.7 Hz for the hardware in a HAM, but this will impress the tilt induced by HEPI drive and defeat the low frequency isolation.

In light of this unintended interaction, for aLIGO HAM HEPI's simply provide DC position and alignment control. This requires little to no force application between 0.1 and 1 Hz, since the relative motion is already very small. The filtered ground seismometer signal, used for sensor correction, is communicated to the ISI instead.

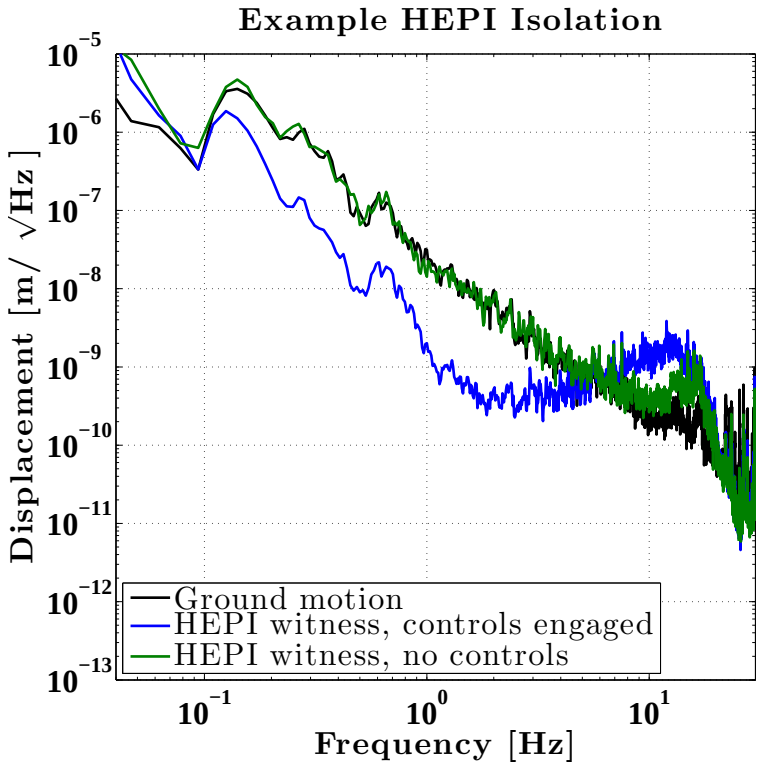

FIGURE 3.12. Typical isolation performance for a HEPI system with a blending frequency of ∼0.5 Hz and a control loop as shown in Figure 3.9. Isolation at the microseism comes from sensor correction and the slight amplification around 10 Hz comes from a combination of the plant dynamics and loop shape.

3.4.2 HEPI during S6

During LIGO's Sixth Science Run (S6), which took place from July 2009 until October 2010, the Livingston detector was equipped already with HEPI, but all in-vacuum isolation was provided by a passive "stack" (a 4-layer mass-spring platform support) except for a single HAM ISI at the detection port (not supporting any interferometrically coupled mirrors, just the OMC). With no inertial sensors on the payload, cross-beam deformation was not an issue for providing isolation at the microseism with HEPI. On the contrary, HEPI proved to be crucial for maintaining duty cycles greater than 50% at the Livingston observatory [74], for two reasons: the microseism as stated previously, but also its ability to damp the in-

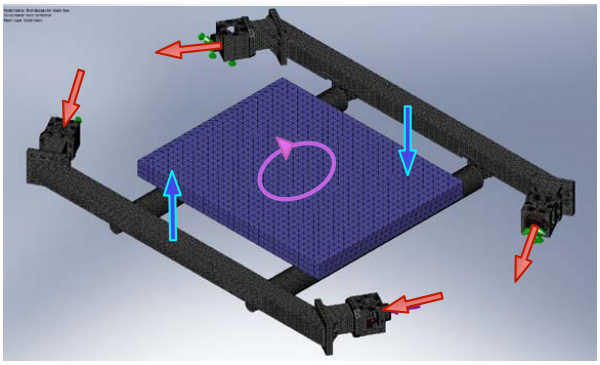

FIGURE 3.13. Cartoon displaying the tilting effect produced by moving a HAM HEPI unit horizontally to provide isolation.

vacuum passive stack's resonant amplification of the 1-5 Hz seismic noise. Without HEPI the Livingston detector was typically only reliably run at night, when the anthropogenic seismicity subsides.

Despite the implementation of sensor correction, high microseismic activity in the winter time or from strong weather systems on the Atlantic or Gulf coasts could prevent detector operation for prolonged periods. To combat this, a new approach was taken for tuning the sensor correction filters which utilized global signals, the interferometric control forces applied to maintain cavity resonance, and combined seismometer signals from all buildings to improve the subtraction [75]. The possibility of improvement was based on the substantial residual coherence between the control signals and the ground motion after the initial factor of ∼10x isolation from sensor correction. In general, two signals, w and t, must be coherent for a linear filter to subtract one from the other, with the coherence being defined as

$$\gamma_{\mathrm{wt}} = \frac{S^2_{\mathrm{wt}}(f)}{S_{\mathrm{ww}}(f) S_{\mathrm{tt}}(f)} \tag{3.10}$$

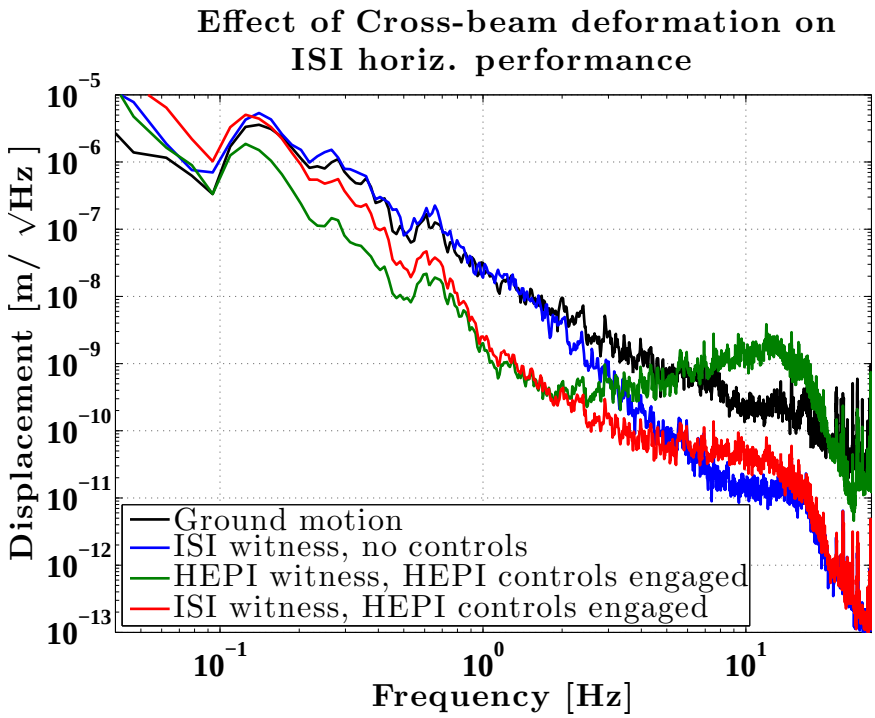

FIGURE 3.14. Effect of HEPI control as seen by two inertial witnesses: the (in-loop) sensors of HEPI and those of the HAM ISI (out-of-loop). While the HEPI sensors report successful reduction in ground motion (compare the green and black traces), the ISI sensors do not experience as much isolation below 1 Hz due to tilting of the platform (compare the green and red traces). The isolation above 1 Hz shown in the blue trace is from the passive transfer function of the ISI, only damping controls are engaged. The blend frequency of the HEPI controller is ∼0.5 Hz.

where $S_{\mathrm{wt}}(f)$ is the cross-spectral density between w and t, and $S_{\mathrm{ww}})(f)$ and $S_{\mathrm{tt}}(f)$ are the power spectral densities of w and t. If the transfer function between w and t, is

$$H_{\mathrm{wt}}(f) = \frac{S_{\mathrm{wt}}(f)}{S_{\mathrm{ww}}(f)}, \tag{3.11}$$

then the error left over from subtraction will be

$$S_{\mathrm{ee}}(f) = S_{\mathrm{tt}}(f) - H_{\mathrm{wt}}(f)^2 S_{\mathrm{ww}}(f,) \tag{3.12}$$

and this can be rearranged to show

$$S_{\mathrm{ee}}(f) = S_{\mathrm{tt}}(f)\left[1 - \gamma_{\mathrm{wt}}\right]. \tag{3.13}$$

In the new scheme, FIR Wiener filters [76] were calculated by solving the equation

$$p_{\mathrm{i}} = \sum_{j=0}^{N} h_{\mathrm{j}} R_{\mathrm{ij}}, \tag{3.14}$$

for the optimal filter h, where R is the auto-correlation matrix of the seismometer signals and p is the cross-correlation between the seismometers (the witnesses) and the interferometric control signal (the target). The resulting filter should minimize the mean square error

$$MSE = \frac{1}{2}\sum_{i}\left[t_{\mathrm{i}} - \sum_{j=0}^{N} h_{\mathrm{j}} w_{\mathrm{ij}}\right]^2. \tag{3.15}$$

The time series of both target and witnesses is first down-sampled to 64 Hz, thereby allowing a filter with a few 1000's of taps to subtract accurately down to a few 10's of mHz. The FIR taps are estimated in MATLAB [77] using a Levinson-Durbin algorithm [78, 79, 80], and then fit, using Vectfit [81, 82, 83], to IIR coefficients for reasonable computation time in the digital controls. Around 1 hour of data is used to train the Wiener filter. Once the IIR version of h has been obtained, the transfer function from the witness summation point to the target signal must be measured, fit, and inverted. Before fitting both the Wiener filter and the transfer function some weighting of the data was applied, to limit the amount of computational resources spent in frequency bands not of interest for microseismic subtraction (most specifically, strong 60 Hz power lines and harmonics). Both the fit of the Wiener filter and the actuation transfer function must be highly accurate, as any

error in measurement and fit contributes to matching error which degrades the subtraction.

During S6, the two most successful implementations of the Wiener filter feed-forward were the reduction in control signal of the power recycling cavity and of the differential arm length. For the PRC, the actuation was performed by the HEPI system supporting the recycling mirror. While several of the seismometer signals in the LVEA were coherent with the cavity control, including the vertical motion, the platform was only actuated along the cavity axis. Figure 3.15 shows the PRC control signal delivered to the suspension, before and after the improved sensor correction, the initial factor of ∼10x isolation was significantly enhanced to the level of ∼100x (99% subtraction). Neither curve includes the effects of low frequency relief provided by passing the control signal on to the error point of the HEPI control loops, which effectively reduces the suspension drive as $1/f$ below 1 Hz (in both sensor correction states).

The length control signal driving the suspension is already quite small in the "off" traces of Figure 3.15, but unwanted side effects of the residual length drive are reduced with the improved subtraction, including:

- Large low frequency signals can cause non-stationary noise in the signal band, a phenomena referred to as *upconversion*.
- Some fraction of the longitudinal displacement is converted to angular motion through imbalanced mechanics and actuation.

The first item is of interest but will be covered in a later chapter. The second item was exacerbated in the eLIGO PRC, since the cavity was close to geometric instability ($g \simeq 1$, where for a two mirror Fabry-Perot cavity $g = g_1 g_2 = (1 - L/ROC_1)(1 - L/ROC_2)$). As such, fluctuating mirror alignments driven by

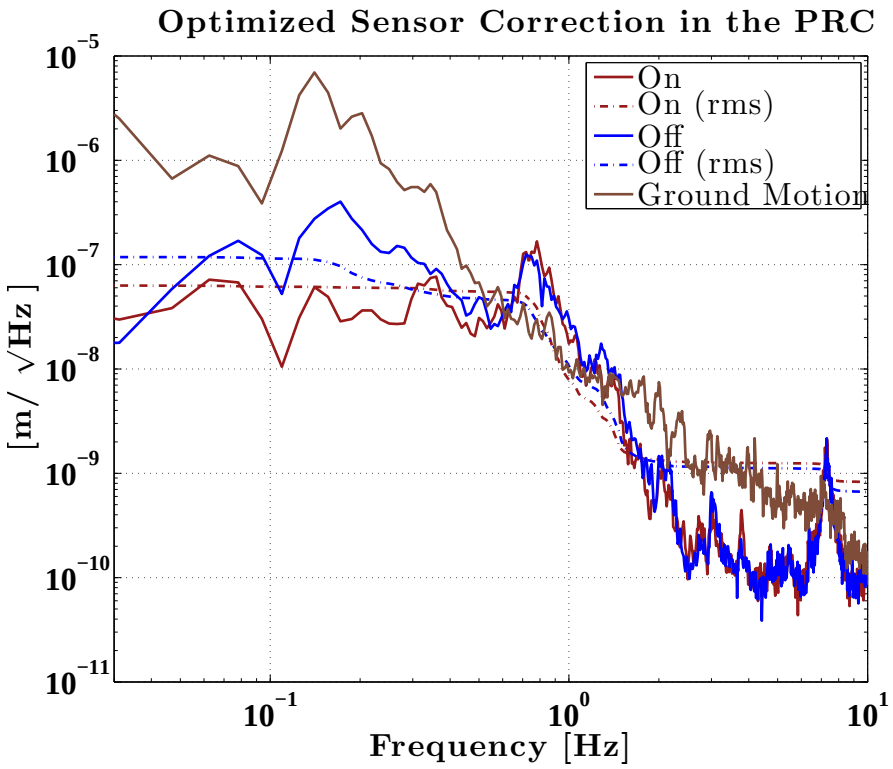

FIGURE 3.15. Further improvement of seismic subtraction gained by using Wiener filters to tune the sensor correction filters, in the eLIGO power recycling cavity. The first reduction, between the brown trace and the blue trace, is gained by use of the sensor correction filter displayed in Figure 3.11. The additional subtraction, between the blue and red traces, is gained via Wiener filtering. The "on" and "off" traces are the control signals applied to the recycling mirror, calibrated as displacement units, but the true residual displacement is suppressed well below these values by the loop gain. The seismic input did not vary significantly during the on/off test displayed here.

seismic motion would cause large power instabilities, and this was a serious obstacle for obtaining high instrument duty cycles during the winter months, when the microseismic activity is high. Figure 3.16 displays the amount of observation time recorded by the Livingston detector, from the summertime start of the run onwards towards the winter of 2009-2010, as well as the rms seismic motion in the 0.1-0.2 Hz and 0.2-0.35 Hz bands.

Seismometers from all three buildings (the corner station and both end stations) were used to tune the DARM sensor correction. This resulted in a factor of ∼3x

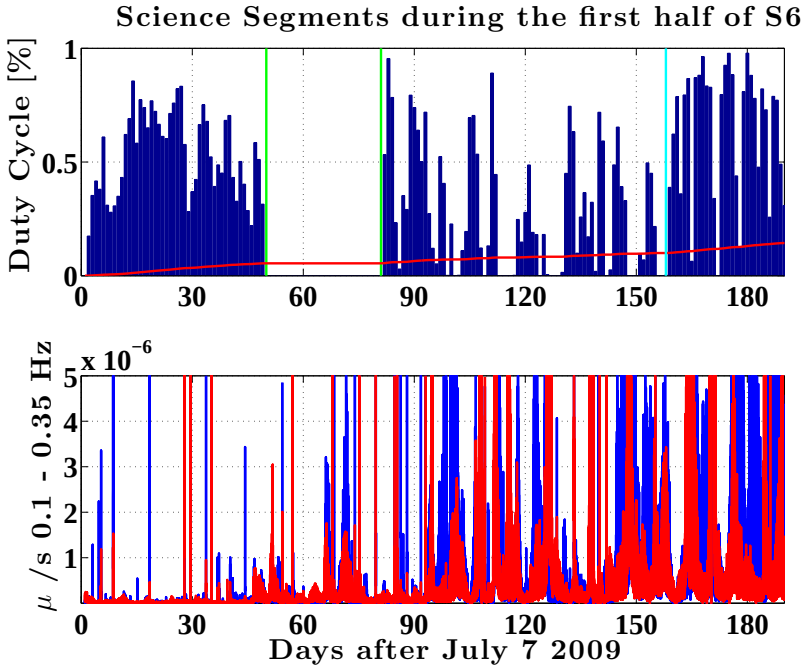

FIGURE 3.16. In the top pane, the daily duty cycle of the L1 interferometer is displayed for the first ∼200 days of the sixth science run, S6. The two vertical green bars represent a planned commissioning break, when the vacuum was breached for detector repairs and data collecting was impossible. The red line represents a running duty cycle average, showing each days contribution to the total amount of science data divided by the total elapsed time during the science run (∼500 days). The vertical cyan line marks the implementation of Wiener filter feed-forward to reduce motion in the power recycling cavity. The bottom pane shows band-limited rms trends of microseismic motion, with the red trace measuring in the 0.1-0.2 Hz band, and the blue trace being in the 0.2-0.35 Hz band. The numerous vertical excursions are from temporary saturations due to earthquakes or facility power outages. This figure is meant to give an idea of the increase in microseismic activity during the winter time, and to show that PRC feed-forward improved the L1 duty cycle when high seismic activity persisted.

reduction in the rms control signal, as seen in Figure 3.17. The HEPI's supporting the end masses of either arm were used for actuation, to avoid injecting any noise into the corner degrees of freedom. Unlike the PRC, amplification of misalignment creating large power fluctuations was not a particular problem of the eLIGO arm cavities, due to their geometry. The cavity axis will become tilted when either mirror in the cavity acquires a misalignment [32] with an amplification factor of

$$\frac{\delta\theta_{\text{cavity}}}{\delta\theta_{\text{mirror}_i}} = \frac{ROC_i}{ROC_1 + ROC_2 - L}. \tag{3.16}$$

For the eLIGO arm cavities, ROC_1 and ROC_2, the ITM and ETM radii of curvature, were $\sim$15 and $\sim$9 km, respectively. For the 4 km long arm this gives a g-factor of $\sim$0.4, and a misalignment amplification of < 1. This effect is more prominent in aLIGO, where the mirror curvatures are both close to 2000 m, and the misalignment amplification is $\sim$10x. This allows for larger beam sizes on the test masses, which reduces thermal noise. The cavity waist is also smaller in the aLIGO arm cavity, so the divergence angle is larger, mitigating the relative mirror misalignment amplification in terms of cavity divergence angle by a factor of several when compared to eLIGO. A more important consequence of the reduction in DARM control signal was the reduction of noise bursts in the signal band, which is detailed in Chapter 5.

3.4.3 HAM-ISI

Until the HEPI beam deformation obstacle is overcome, the single stage in-vacuum systems will be responsible for isolation at low frequencies and at 1 Hz simultaneously. The HAM ISI is suspended from 3 blade springs whose resonance is around 0.8 Hz, with an undamped Q of $\sim$25 [88, 84]. The isolated platform's mass is $\sim$1500 kg. The connection to the payload from these springs is done via flexures, which act as horizontal springs with a resonance of just over 1 Hz, with a similar Q. An engineering drawing of a HAM ISI is shown in Figure 3.18.

The control topology is the same as the scheme shown in Figure 3.10, save for the twist correction which is unnecessary with the HAM ISI, due to its compact and rigid aluminum structure. Indeed, the earliest relevant structural modes of the HAM ISI are at $\sim$100 Hz or higher, allowing for robust control loops with much

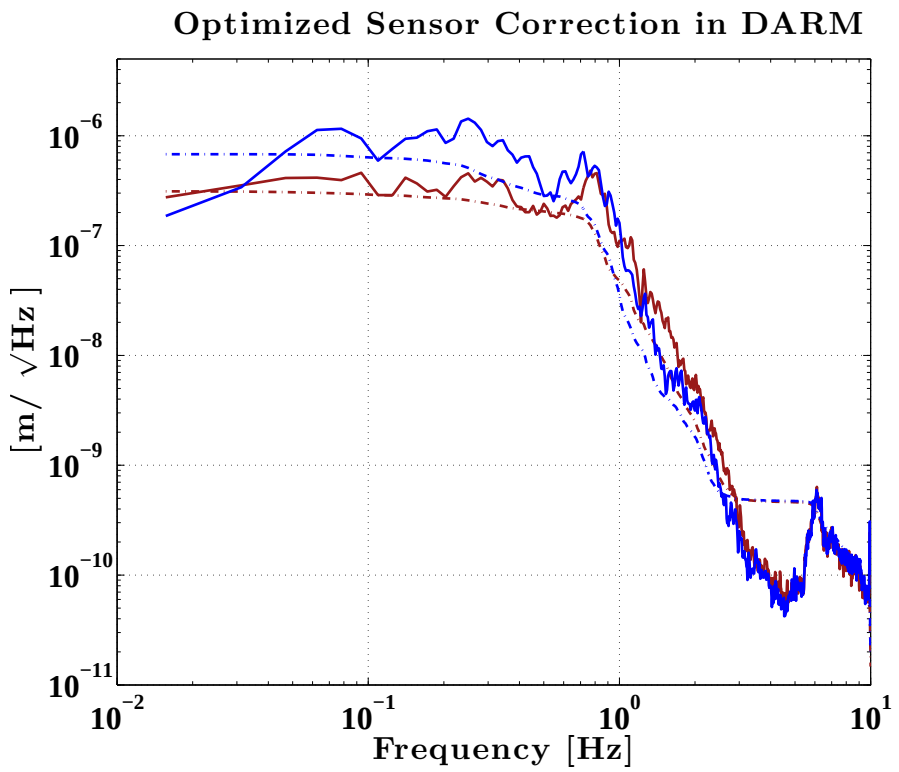

FIGURE 3.17. Tuning of sensor correction using the DARM control signal. Seismic motions along the arm baselines vary from correlated to uncorrelated depending on the source, and at the worst of times can be anti-correlated (differential motion double that of the local motion at either end of the cavity). The seismic input did not vary significantly during the on/off test displayed here.

higher bandwidths than HEPI, and in practice 30-40 Hz UGFs are easily achieved, as shown in Figure 3.19. Apart from tilt-horizontal coupling in the inertial sensors, the HAM ISI can be treated as 6 independent SISO control loops. The isolation loops are accompanied by simple damping loops, which use the inertial sensors on the suspended payload to bring the fundamental resonance in each DOF down to a $Q > 1$.

The relative position and inertial sensors are a little different on a HAM ISI when compared to HEPI. The platform is outfitted with 6 each of

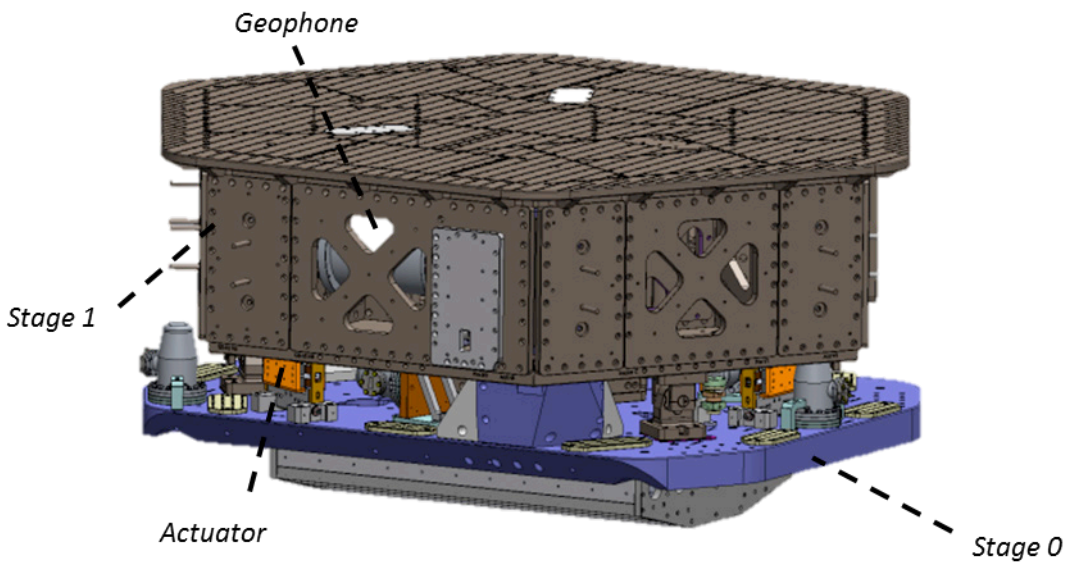

FIGURE 3.18. Engineering drawing of a HAM ISI unit, with the location of the relevant components indicated.

- Capacitive position sensors (CPS), referencing the support frame (which communicates through a vacuum bellows to HEPI) against the isolated platform, made by MicroSense, with a noise floor of roughly 2x10^{-10} m/$\sqrt{\text{Hz}}$,
- Geotech GS-13 seismometers, with a noise floor of slightly less than 1x10^{-11} m/$\sqrt{\text{Hz}}$ at 1 Hz, rising roughly as f^{-3} below this.

Also, there are three horizontal and three vertical actuators, comprised of magnets and coils similar to those which drive the suspensions.

While the rapid increase in low frequency inertial sensor noise is the main consideration when designing the sensor blending filters, the HAM ISI problem is constrained by the fact that the suspensions it supports are all standing up from the isolated table, as well as not being placed at its center of rotation. The lever arm between the table top and the suspension point is ∼1 m, indicating that 1 rad/$\sqrt{\text{Hz}}$ of pitch along the beam direction is approximately equivalent to 1 m/$\sqrt{\text{Hz}}$ of motion. In most instances the coupling of yaw to suspension point displacement is less severe than this, but non-negligible. So, while one may want to

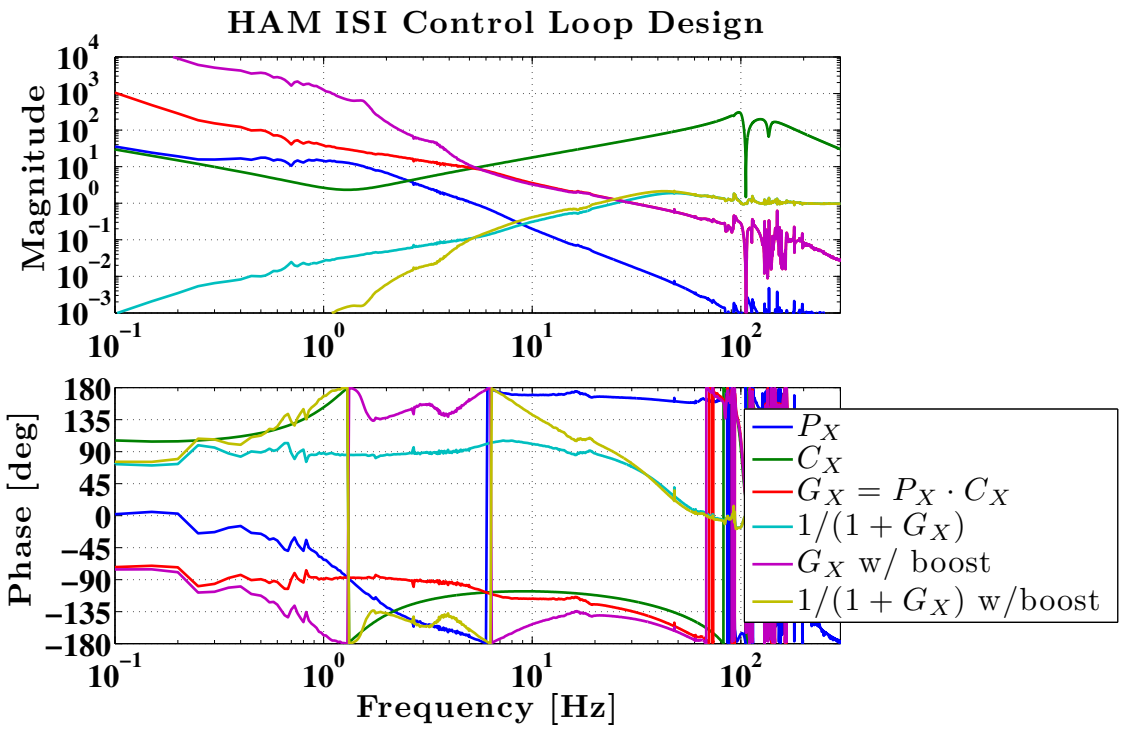

FIGURE 3.19. Frequency responses of an example HAM ISI control loop (see i.e. Figure 3.4 for variable definitions). Up to 100 Hz the plant is well approximated as a simple mass on a spring. Above 100 Hz some structural resonances appear, but are easily accounted for without sacrificing significant loop margin or gain. Gains of ∼1000x at 1 Hz are sufficient to suppress typical seismic disturbances to the inertial sensor noise floor, assuming enough low-passing of the position sensors is employed.

design an aggressive high-pass for the inertial sensor in the RX or RY DOF (tilts), to avoid polluting the horizontal degrees of freedom at low frequency, this will inevitably sacrifice low-passing performance around the frequency of the suspension resonances, which could have Q's of 10's, amplifying the input motion.

A noise budget, incorporating these effects, is shown in Figure 3.20. A performance plot of an installed HAM ISI is shown in Figure 3.21. The main suspension resonance for the mirrors supported by HAM ISI's is ∼0.7 Hz, and at this frequency the horizontal performance approaches the inertial sensor noise. Reducing it further would require more low-passing of the position sensor, resulting in excess low frequency motion, while not improving the suspension point performance which is dominated by direct coupling from tilt. Good coherence between the GS13's and

seismometers placed on the ground allow for a factor of several to ∼10x isolation from sensor correction from 0.1 up to 1 Hz.

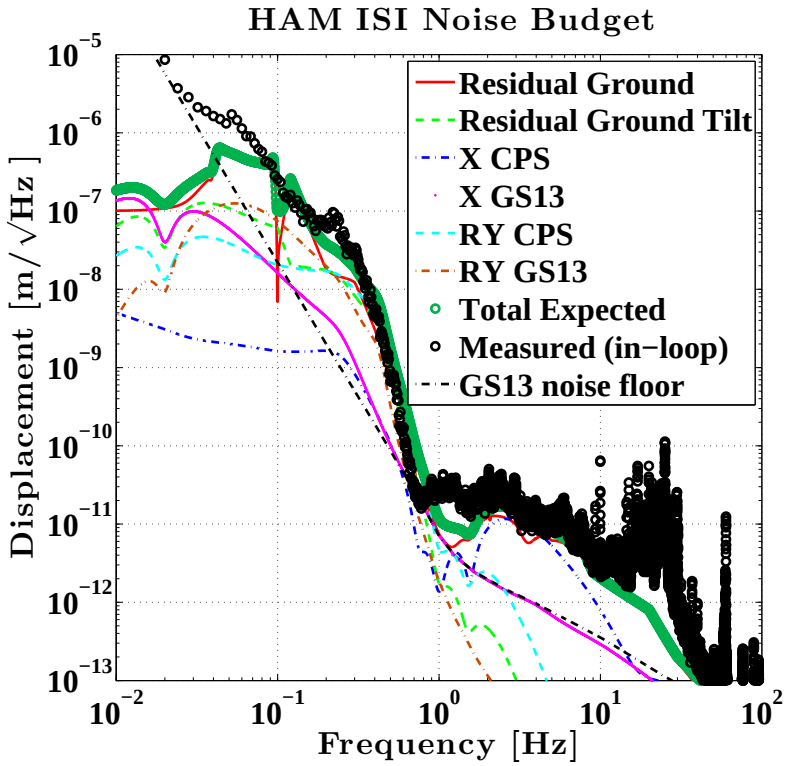

FIGURE 3.20. Noise budget for the horizontal motion of a HAM ISI, with measured motion for comparison. Below 0.1 Hz the witness spectrum is self noise limited, so comparison with the budgeted motion becomes difficult, but above this the measured motion relatively well matches the expectation.

3.4.4 BSC-ISI

Schematically the two stage isolation platform is quite similar to two HAM ISI's, one suspended from the other, although in reality the mechanical assembly is quite a bit more elegant [86, 87, 84]. The two stages, each suspended with blade springs and flexures, have similar actuators to the HAM ISI, and are outfitted with a number of sensors:

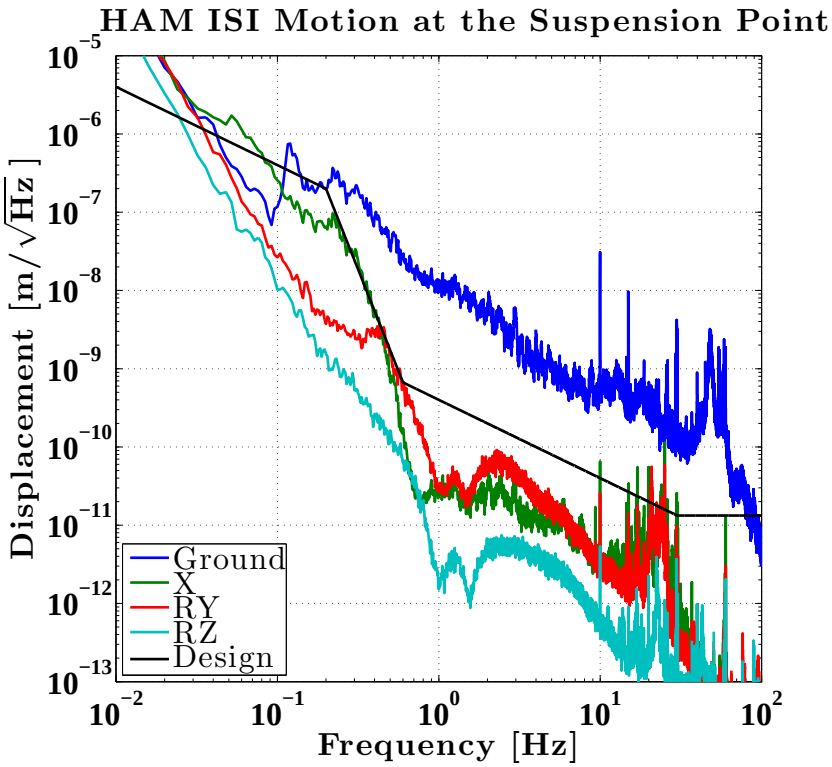

FIGURE 3.21. Typical motion of a HAM ISI platform, as witnessed by the in-loop GS13s. The black curve is the designed performance, which is met or exceeded at all frequencies. At low frequencies, below 0.1 Hz, the requirement is more of an rms goal, and all the spectra here are limited by GS13 noise at these frequencies. The pitch and yaw of the platform are multiplied by their respective lever arms to transfer their motion to that experienced by the suspension point. The excess above ground motion below 0.1 Hz is due to the shape of the sensor correction filter.

- Stage 1 uses 6 of the same capacitive position sensors as the HAM ISI to reference the support, a thick ring of aluminum referred to as Stage 0, which in turn is supported by HEPI.

- Stage 1 also has 3 3-axis, low frequency seismometers, the Trillium T240, which has excellent noise at the microseism (1 nm/$\sqrt{\text{Hz}}$), and a noise which increases only as f^{-1} until $\sim$5 mHz. This is significantly better than the 1 Hz geophones, but the T240 does not perform as well at higher frequencies.

- Stage 1 also has 6 L4-C's, to complement the low frequency performance.

- Stage 2 references Stage 1's position with 6 capacitive sensors, made slightly more sensitive by having a smaller gap spacing between Stages 1 and 2 when compared to Stages 0 and 1.
- Stage 2 also has 6 GS13's.

The total assembly (Stage's 0, 1, and 2) is quite large, with a combined mass of ∼4500 kg. An engineering drawing of a BSC ISI is shown in Figure 3.22.

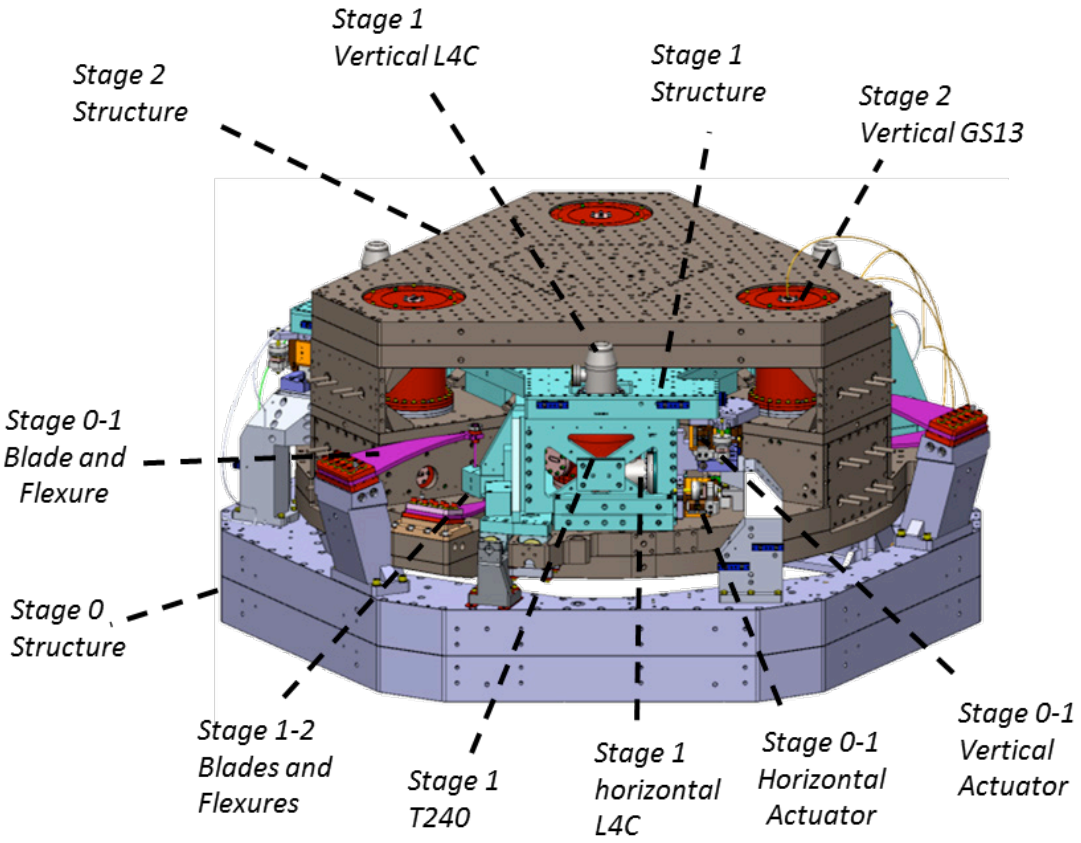

FIGURE 3.22. Engineering drawing of a BSC ISI.

The use of GS13's on Stage 2 places the limit on the performance between 1 and 10 Hz, with the combined effect of both stages' control loops suppressing the input motion to the sensor noise at these frequencies, Figures 3.23 and Figure 3.24 show typical servo shapes. Above 10 Hz the loop gain is not very large but the two stage platform provides the isolation of a double pendulum.

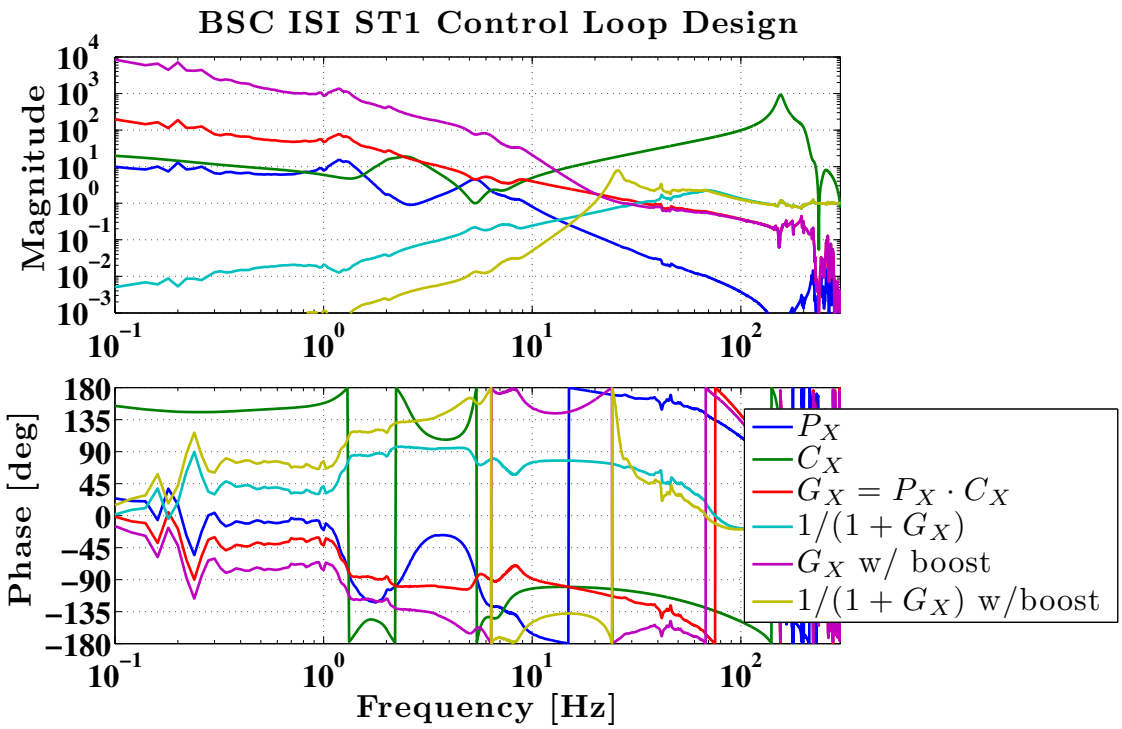

FIGURE 3.23. Frequency responses of an example BSC ISI Stage 1 control loop (again, Figure 3.4 contains variable definitions). The double pendulum dynamics produce some extra features around a few Hz but the unity gain frequency is high enough (∼40 Hz) for these not to matter much.

Below 1 Hz the presence of the low frequency seismometers on Stage 1 allows for a significantly different control topology than HEPI or the HAM ISI. Both of those systems rely on sensor correction to provide isolation at the microseism, whereas a BSC ISI can rely on feedback. The suspensions which the BSC ISIs support have lower primary resonances than those supported by HAM ISIs, with the main test mass suspension resonance being ∼0.4 Hz, making better microseism isolation attractive. Achieving a factor of ∼10x via subtraction is doable, but factors of ∼100's can be gained with feedback, since feedback avoids the necessary gain and phase matching of sensor correction.

The drawback to feedback is, of course, stability, and this is complicated by the use of capacitive position sensors. The vertical sensors are formed by two parallel, horizontal plates (the "probe" and the "target". If there is a misalignment in these

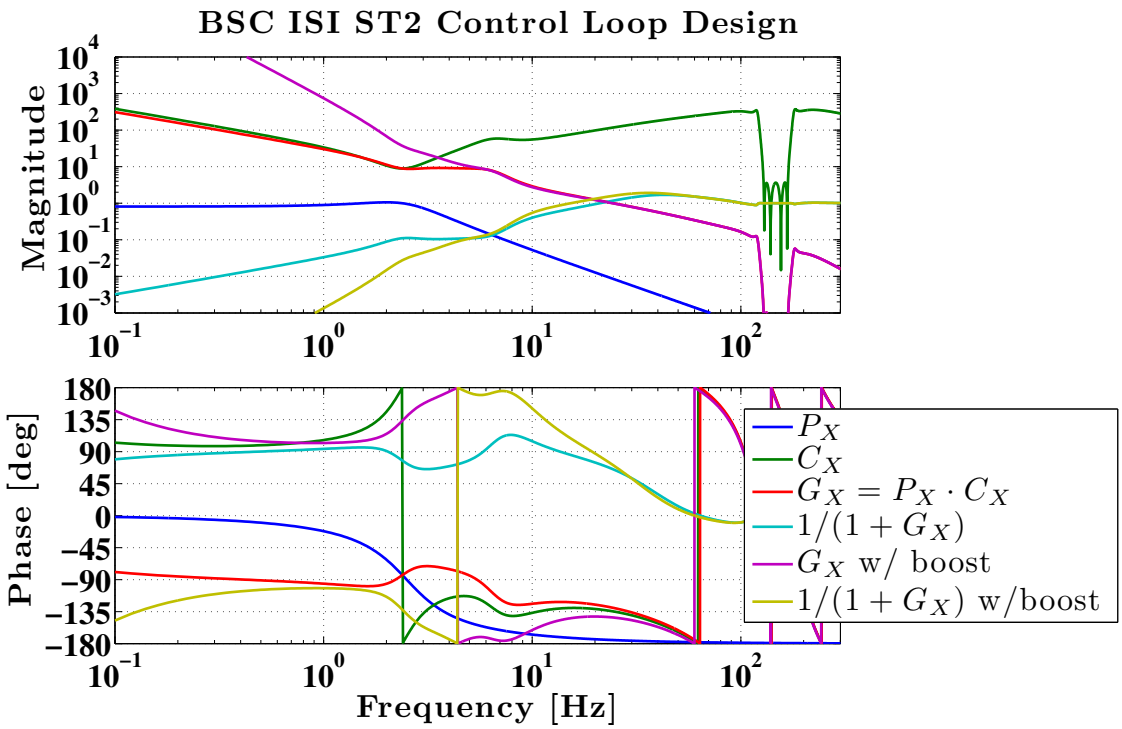

FIGURE 3.24. Frequency responses of an example BSC ISI Stage 2 control loop (again, Figure 3.4 contains variable definitions). When Stage 1 is under control, the Stage 2 plant approaches that of a single pendulum, although number of very high frequency ($f > 100$ Hz) mechanical resonances have to be suppressed to avoid instability.

plates, i.e. a deviation from parallelism, then as the suspended platform moves relative to the support there will be a sensed tilt, see Figure 3.25. This tilt will be immediately impressed into the motion of the platform by the rotational control loops, potentially generating more horizontal motion via tilt-horizontal coupling, generating more sensed tilt in the position sensor, leading to ringing or instability in the relevant degrees of freedom.

When the rotational control loops are engaged, the degree of misalignment can be gauged by measuring the "tilt crossover frequency", f_{txo}. This is done by exciting a large relative motion between Stage 1 and Stage 0 (while HEPI is controlled), at low frequency in the horizontal degrees of freedom. By monitoring the horizontal inertial sensors, their response to the excitation (which should be flat in frequency, i.e. 1 to 1 [m/m]) will evolve into a $1/f^2$ dependence at low frequencies due to

the tilt-horziontal coupling. The frequency where this happens is the tilt crossover frequency. Depending on the sign of the curvature of the trajectory the platform is following, the transition from flat to $1/f^2$ will either be smooth are marked with a notch in the magnitude response (the two effects partially cancel).

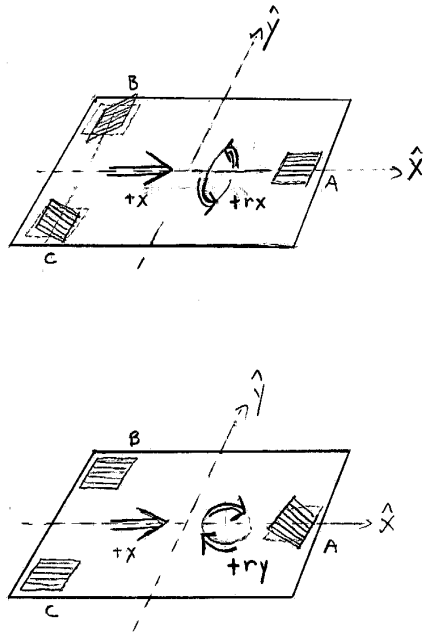

FIGURE 3.25. A sketch showing how deviation from parallelism in the horizontal plates of the vertical position sensors can generate tilts. All credit to the artist: Brian T. Lantz.

Technically this effect exists on a HAM ISI as well, but it is not as important since those units are generally assembled well enough to provide $f_{txo} \sim 45$ mHz. This is far enough below the ∼250 mHz horizontal blending frequency to not cause controls robustness issues. For a BSC ISI , which uses feedback for microseism isolation, the blend frequency is necessarily much lower, as low as 45 mHz. This places the tilt crossover feature squarely in the blending band, and would produce unstable controllers if left uncorrected. Corrections are made by adding small components of the X and Y position sensor signals to the rotational degrees of freedom.

A closer look at this effect in the presence of a low horizontal blend frequency was performed by constructing a simplified Simulink model of the BSC ISI, where

the tilt horizontal frequency was included as a variation on the inertial sensors nominal frequency response. Figure 3.26 shows the additional transfer function for a variety of tilt crossover frequencies, and Figures 3.27 and Figures 3.28 display the resulting changes in the transfer function of horizontal and rotational ground motion to the horizontal motion of Stage 1. For this particular set of blend filters, the development of a peak in the motion amplification around 80 mHz can be seen for less well tuned systems, and a similar effect has been observed on installed units when their CPS alignment adjustment is incomplete; see Figure 3.29.

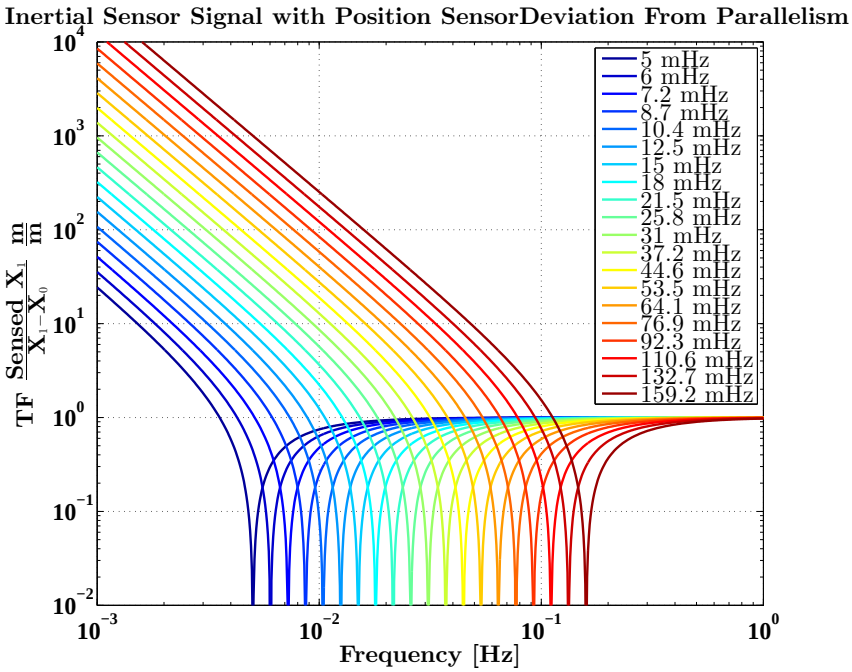

FIGURE 3.26. Modified response of the inertial sensors used for modeling the effect of capacitive position sensor plate misalignment on low frequency feedback control stability. The lowest modeled f_{txo}, 5 mHz, is close to the best achieved on aLIGO BSC ISI units. The highest, 160 mHz, is well above the as assembled tilt crossover of 45 mHz, and was included to explore the model space.

.

Stability and noise injection issues are sufficiently mitigated when $f_{\mathrm{txo}} < 15$ mHz. In practice, all units are tuned at the level of a few in 10^4, corresponding

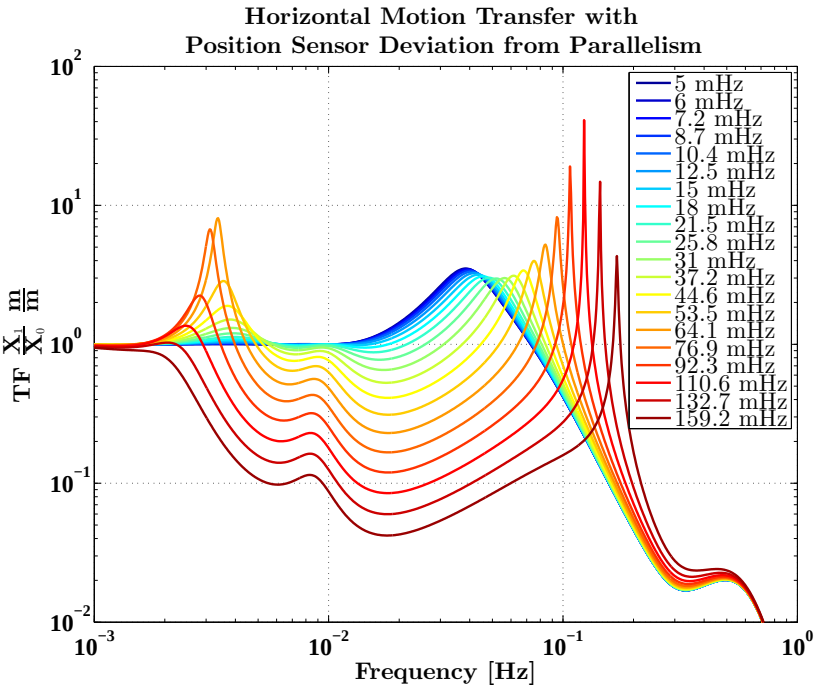

FIGURE 3.27. Transfer function of horizontal ground motion to horizontal Stage 1 motion in the presence of both a low blending frequency and CPS plate misalignment of varying degrees. The lowest tilt crossover curves, in blue, show no significant effect remains from plate misalignment, and the transfer function is simply the frequency response of the blend filter (this filter corresponds to a blend frequency of 45 mHz). As the plate misalignment degrades, significant motion injection occurs both above and below the blend frequency, with a peak appearing in the vicinity of 0.1 Hz, characteristic of low phase margin in the super-sensor formation. As the deviation becomes minimized the transfer function approaches the frequency response of the blending low-pass filter.

.

to tilt crossover frequencies as low as 5 mHz, far enough outside of the Stage 1 blending band. This corresponds to a sensor plate relative angle of ∼100 µrad or less.

In the configuration described above, the isolation provided by the first stage of the BSC ISI is shown in Figure 3.30, and a noise budget of the contributing terms to the horizontal (labelled "X) motion is shown in Figure 3.31. The two traces "RY" and "RZ" correspond to the coupling of platform pitch and yaw to the longitudinal motion of the suspension point. A distinct advantage in this regard,

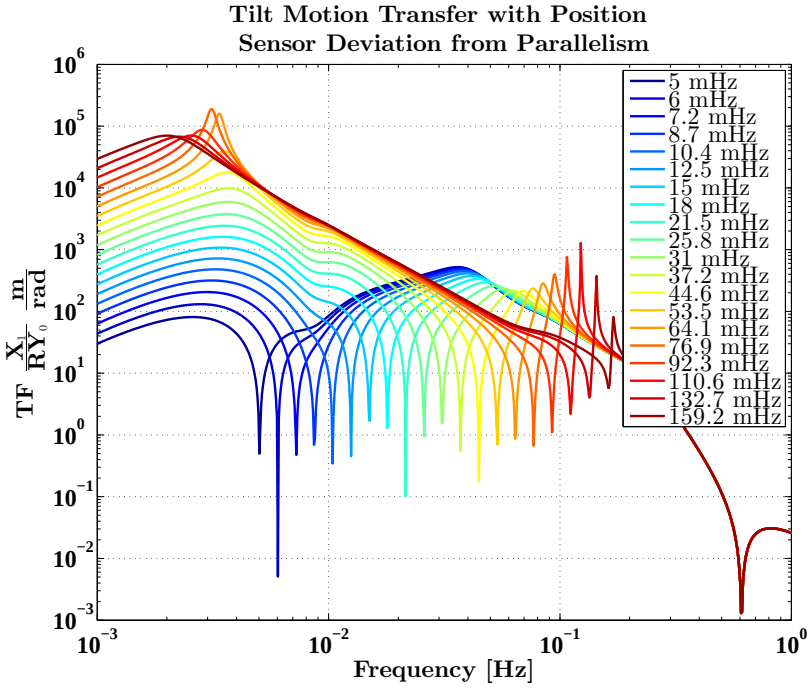

FIGURE 3.28. Transfer function of rotational ground motion to horizontal Stage 1 motion in the presence of both a low blending frequency and CPS plate misalignment of varying degrees. While the 0.1 Hz feature also appears in this modeled interaction, more worrisome is the rapid increase in low frequency noise injection.

.

when compared to the HAM ISI, is that all suspension payloads are supported by connecting their tops to the underside of the seismic platform, providing short lever arms for platform pitch to suspension point horizontal motion (the distance is around 1 meter for a HAM ISI, and around 25 cm for a BSC ISI). The yaw coupling is through about a 20 cm lever arm. A factor of ∼10x isolation is realized at the microseismic peak of 0.15 Hz, rapidly improving to a factor of ∼300x at the primary test mass suspension resonance of 0.42 Hz. At 1 Hz the motion is $\sim$ 1x10^{-10}m/$\sqrt{\text{Hz}}$, leaving about an order of magnitude for the Stage 2 controls to provide to reach the goal displacement.

The degree of low-passing required in the Stage 2 horizontal loop is relaxed considerably by the aggressive Stage 1 controls, with the focus now being on limiting

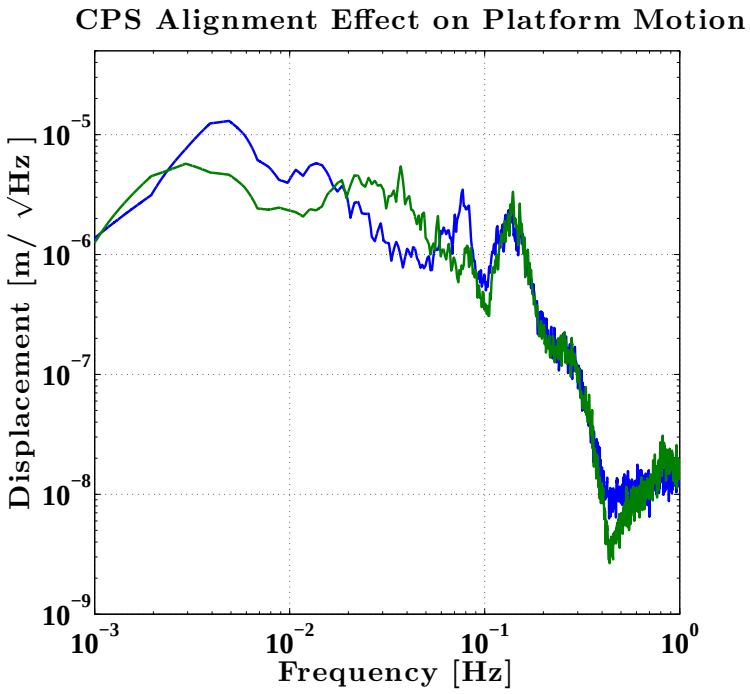

FIGURE 3.29. Comparison of the Stage 1 CPS spectra of two platforms with different tilt crossover frequencies. Above 0.1 Hz the CPS turns into a sensor of ground motion, due to the small motion of the suspended stage. The peak in the blue spectrum around 80 mHz and the excess below 20 mHz resemble the expected features of the modified transfer function when there is a (slight) CPS misalignment.

.

gain peaking around the blend frequency (∼250 mHz) to a few dB's, to avoid giving up the benefits of the 45 mHz blend on Stage 1. The rotational blend frequency must also be kept relatively high, ∼3/4 Hz, to avoid GS13 noise coupling through the Stage 2 tilt controls. Figure 3.32 shows the combined Stage 1 & 2 blend filters' effect on the transmission of ground motion. Also shown is the shape of a sensor correction filter which targets the core optic main suspension resonance, 0.42 Hz, which is used on Stage 1.

Once the tilt coupling from platform controls rivals the tilt coupling of the ground it becomes advantageous to use sensor correction for this extra isolation, instead of further low-passing in the blend filter which would necessarily come at the cost of less high-passing. All of these effects are included in Figure 3.33, which shows

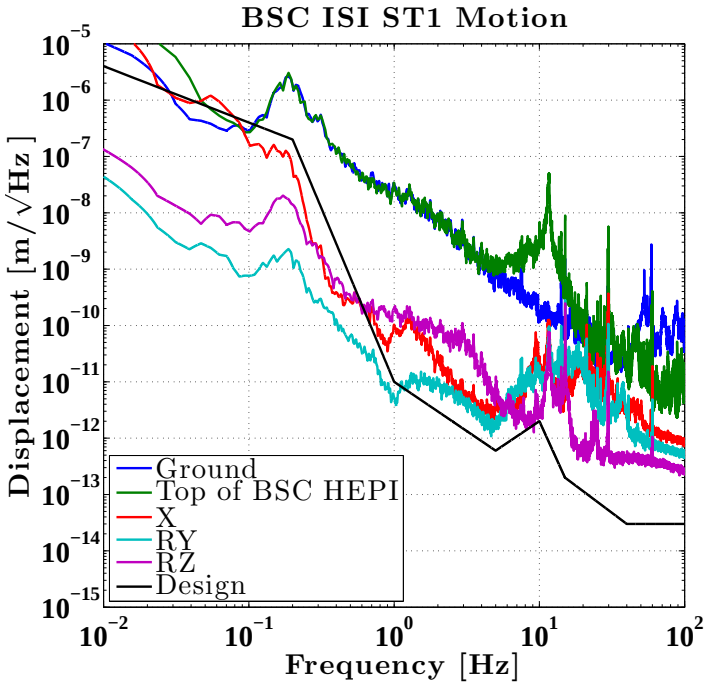

FIGURE 3.30. Motion of the first stage of a BSC ISI, in the units of suspension point displacement along the axis of the laser beam. The blue and green traces are measures of the input motion to the seismic platform, where the blue trace is generated by a sensor on the ground while the green trace is generated by sensors at the top of the HEPI super-structure which supports the in-vacuum payload. The peak at 12 Hz is due to resonant mechanical interactions between the HEPI supports and the chamber, including a significant contribution through the flexibility of the concrete slab itself [85]. The "Design" curve is for both stages of the BSC ISI, and frequencies where the Stage 1 motion exceeds it can be improved by the second stage control and passive isolation.

the in-loop measurement of Stage 2 motion along the beam direction. Figure 3.34 shows the estimated noise, which matches the measurement well.

A driving force in the design of the isolation loops is the reduction of angular motion, generated by longitudinal motion of the platform. This can be examined by bouncing a laser beam off of the mirror surface and measuring the motion of the reflected beam on a quadrant photodetector, a setup referred to as an "optical lever". Figure 3.35 shows the result of such a setup, on a test mass mirror on a BSC ISI, showing the strong effect of longitudinal isolation on the pitch motion, with the added isolation provided by the sensor correction around the suspension resonance.

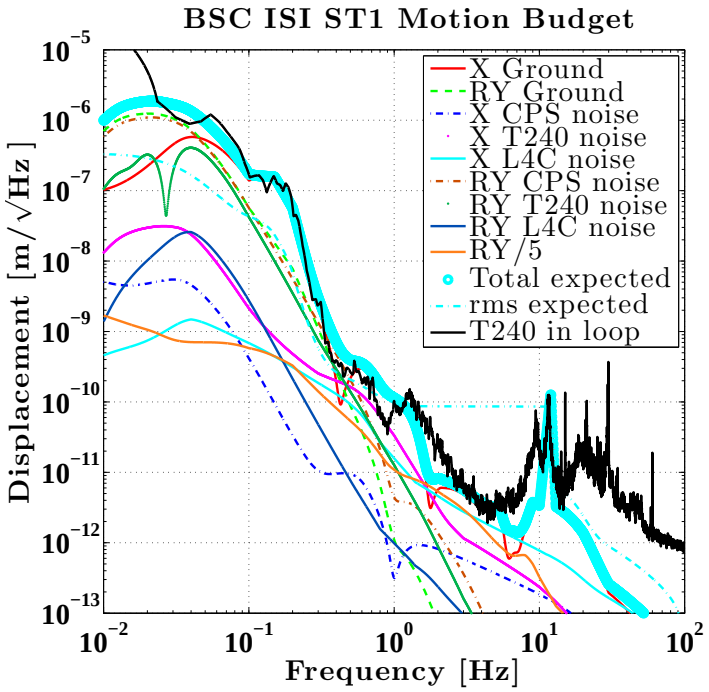

FIGURE 3.31. Noise estimation for the horizontal motion of Stage 1 of a BSC ISI. The total expected noise is the thick cyan curve, to be compared to the in-loop spectrum shown in black. The expected rms motion down to 10 mHz is a few 100's of nm. Residual seismic motion is the limiting contribution between 0.1 and 0.5 Hz, but lowering the blend frequency to isolate further would allow too much tilt injection below 0.1 Hz. Sensor noises compete between 0.5 and several Hz. Above 10 Hz the prediction and measurement diverge significantly. In the simulation the passive isolation rolls off the noise without issue, whereas cabling or other noise couplings dominate in reality. Below 0.1 Hz tilt dominates, with approximately equal contributions from the modeled inertial tilt of the ground, and the noise of the vertical position sensors.

Despite this, the pendulum resonance is clearly visible, due to residual seismic input, and would benefit from an even low blend frequency or a more aggressive sensor correction design. Both of these were avoided due to the unavoidable noise injection below 0.1 Hz, but such a scheme could be considered after interferometer lock is successfully acquired, since the amount of motion engendered would only be a problem for the transient controls and not the steady-state actuation.

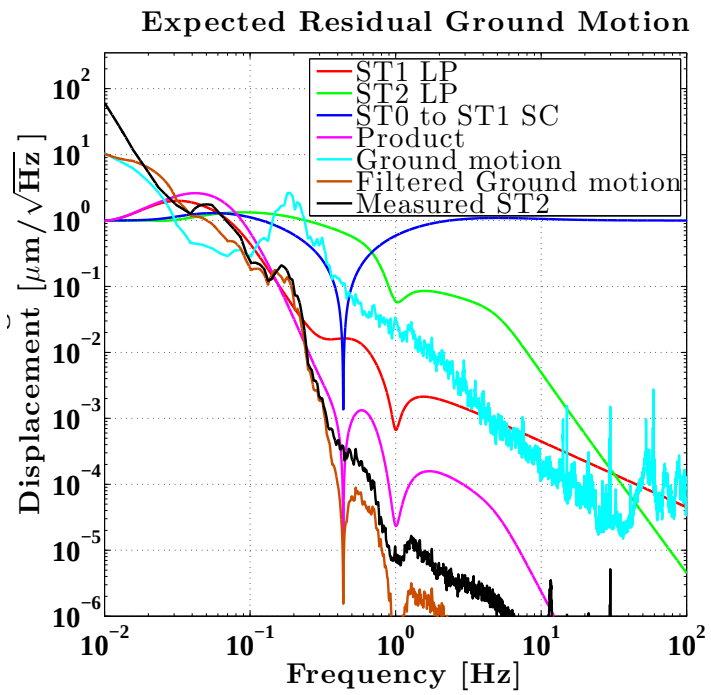

FIGURE 3.32. Effect of Stage 1 and Stage 2 feedback and feed-forward filters on the ground motion, compared to measured residual motion of Stage 2. The Stage 1 sensor correction is designed to provide good gain and phase matching only at the primary suspension resonance of the core optics, with little noise injection at other frequencies, in contrast to the FIR style sensor correction filter used for HAM chambers.

3.5 Integrated System Performance

All measurements presented in the previous section use as witnesses the same sensors used as errors signals in the control loops. But to assess the true effectiveness of the isolation platforms it is necessary to measure the control signals required to maintain cavity resonance, which was not possible during prototyping. A partial schematic of the interferometer's sensing and control scheme is shown in Figure 3.36, with the particular cavity lengths examined in this section highlighted. The cavity control signals serve as an out-of-loop witness sensor, and if there is motion which does not couple to the cavity control it is not of much concern. This section will explore how the cavity signals present the residual seismic platform motion, with the implicit, but important, message that full interferometer lock

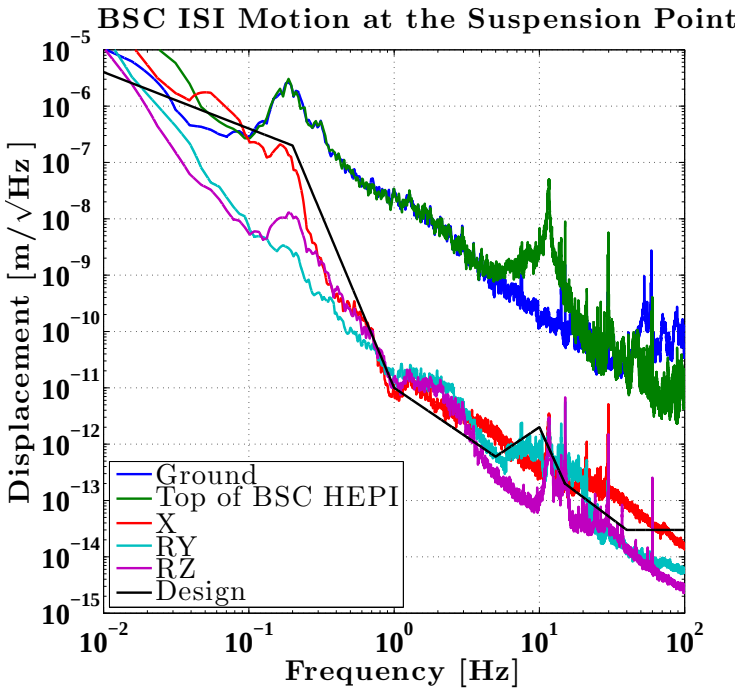

FIGURE 3.33. Motion of the second stage of a BSC ISI, again in the units of suspension point displacement along the axis of the laser beam. An isolation factor of >1000x is provided from ∼1 Hz and above, with the X, RY, and RZ contributions roughly equivalent. The low frequency isolation provided by Stage 1is preserved by carefully limiting gain peaking in the Stage 2 horizontal blend while simultaneously limiting tilt injection from GS13 noise with high blend frequencies in the Stage 2 rotation loops.

in Advanced LIGO was first achieved with the seismic controls scheme described here.

Before entering the interferometer, the laser field is filtered through an auxiliary cavity, the Input Mode Cleaner (IMC). The IMC is a triangular cavity where each mirror is the suspended as the final mass of a triple pendulum. The three mirrors are placed on the first two HAM ISI's in the system, which they share with the power recycling cavity mirrors, see Figure 3.37. The cavity length (one-way) is ∼16.5 m. Truthfully, there is only one mirror which is the "power recycling mirror," the other two mirrors (PR2 & PR3) are curved folding mirrors which both extend the cavity length and act as a telescope which matches the small input beam ($\omega \sim 2$mm) to the mode of the arm cavities ($\omega \sim 5$ cm). This choice

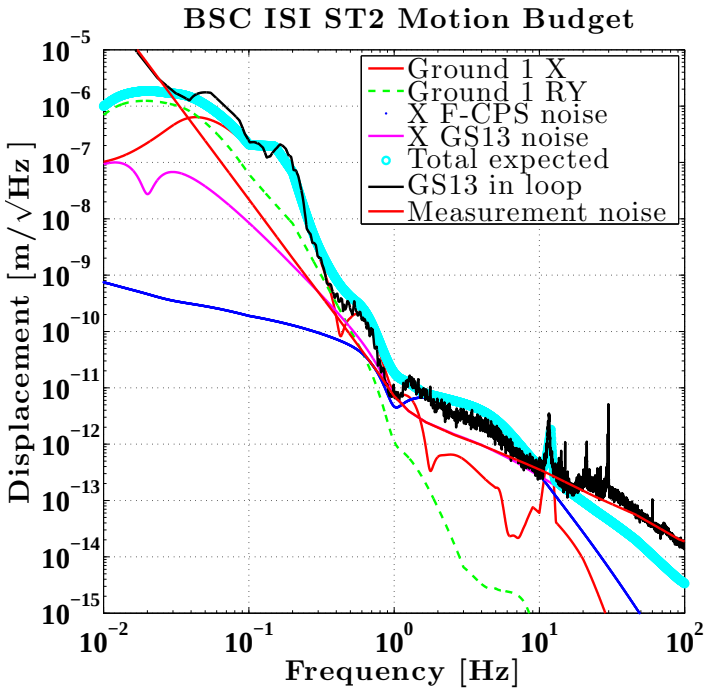

FIGURE 3.34. Noise estimation for the horizontal motion of Stage 2 of a BSC ISI. Apart from the 0.1 to 1 Hz band the measurement is close to the instrument noise of the in-loop sensor. The predicted motion is a good match to the measurement, diverging only where the measurement is sensor noise dominated.

of optical layout is not unimportant for the seismic isolation, since the resonant beam in the PRC will bounce off of PR2 and PR3 twice, doubling their coupling of both displacement noise and angular motion. Also, due to those two mirrors' curvatures there is an additional angular motion amplification, in the basis of the cavity eigenmode.

Figure 3.38 shows an example spectrum of the IMC cavity control signal. The error point for the mode cleaner servo is the frequency discrepancy between the laser input and the cavity length, measured using the PDH technique described in the introductory sections. At frequencies where the isolated mirrors are expected to be less noisy than the PSL frequency, the laser is tuned to match the cavity. Below some frequency, the PSL will be more stable and instead the cavity mirrors are forced to match the input field. The crossover frequency is ∼15 Hz, whereas the

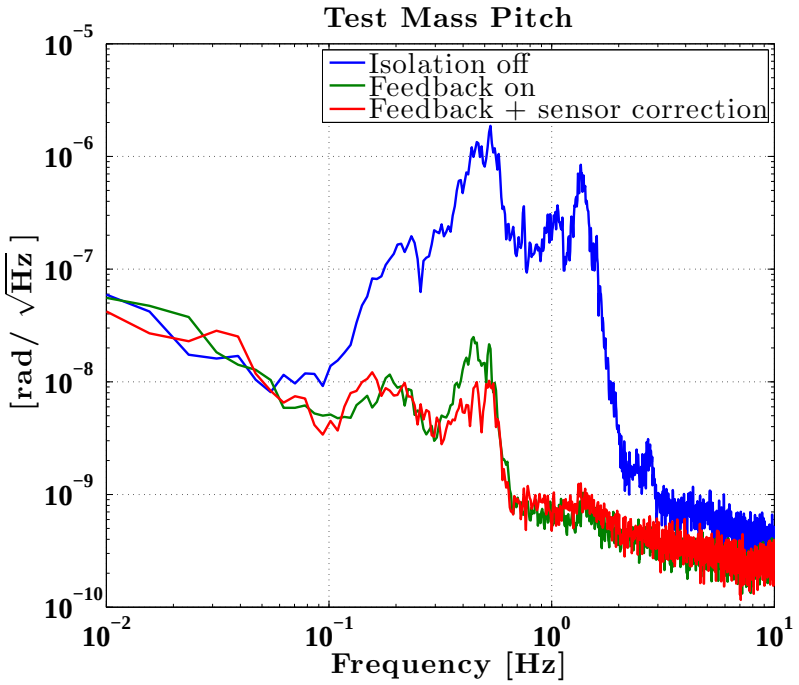

FIGURE 3.35. Angular motion of the test mass as witnessed by an optical lever.

overall stabilization bandwidth is ~ 50 kHz. The length control signal will be due to residual seismic motion as well as noise associated with the suspension damping and controls; the first three pendulum resonances are visible in the spectrum between 0.5 and 3 Hz.

The baseline of the IMC is relatively short, and the motion of the ground is highly coherent between the two isolation platforms. As such, the cavity experiences a high level of common mode rejection, since only differential motions are sensed. In contrast to the other cavities in the corner station, the IMC contains nearly identical suspensions (identical in design, only the slightest of symmetry breaking in mechanical assembly), preserving much of this common mode rejection. If this were reliably true for the entire site, that is, the motion between corner and end stations was also highly common mode and all suspensions resonated at the same frequency, the isolation picture would be somewhat simplified. Unfortunately, common motion of the test masses at low frequencies cannot be counted on,

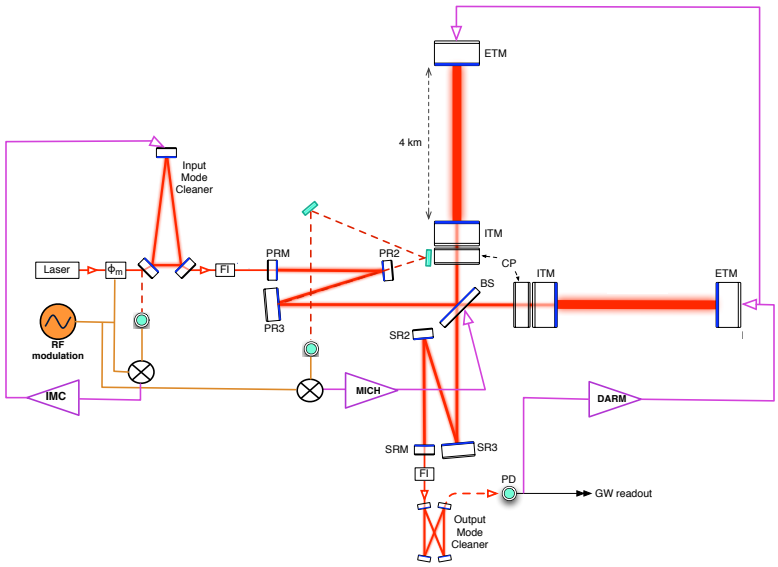

FIGURE 3.36. The interferometer uses both phase modulation and DC readout schemes to sense and control the optical cavity lengths. At low frequencies, the control signals applied to the mirrors to null the interferometric error signals serves as an out-of-loop witness of the platform motion. The IMC is PDH locked in reflection, while the Michelson error signal is derived by demodulating the intra-cavity power of the corner interferometer. In its low noise configuration, the DARM degree of freedom is sensed by a DC signal at the anti-symmetric port.

due to their wide separation, and as such the global reference, especially at the microseism, must be inertia. This has little consequence for the IMC, however, since it rests on HAM ISI's which use sensor correction for microseism isolation, and it is easy enough to utilize the same ground seismometer for both platforms. In this way, the unavoidable noise injection below 0.1 Hz is common to both tanks and the cavity is relatively immune; compare the in loop ISI witness (red trace) with the cavity control (green trace) below 0.1 Hz in Figure 3.38. The rejection is limited by the rolled-off sensor noise of the platform controls, the chief contributions being $H_{\mathrm{X}} N_{\mathrm{GS13-X}} + (H_{\mathrm{X}} H_{\mathrm{RY}} N_{\mathrm{GS13-RY}}) g/\omega^2$,also projected in Figure 3.38, both individually (labeled "horizontal" and "rotation" GS-13 noise) and their quadrature sum. Here rotation specifically refers to the table pitch (RY), since the beam axis is almost completely aligned with the interferometer's X axis.

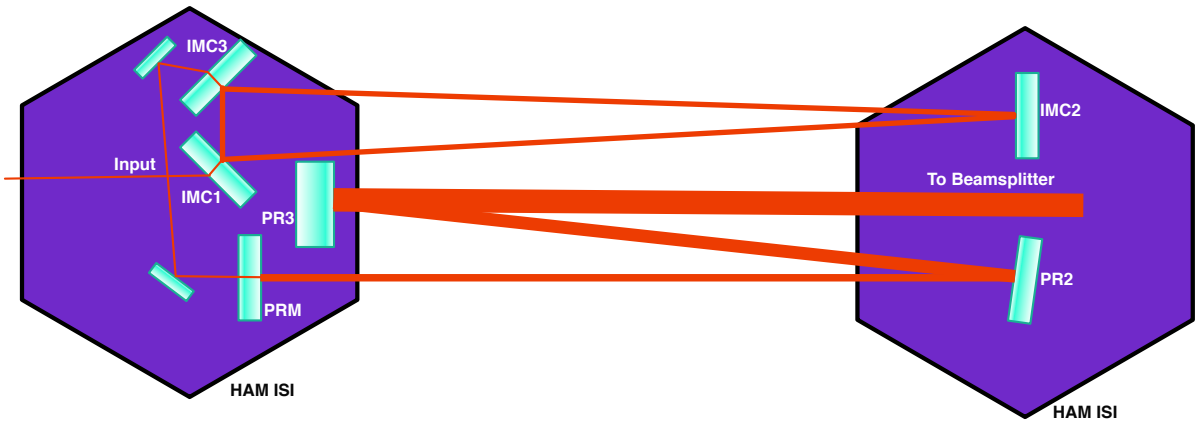

FIGURE 3.37. Optical layout of the interferometer front-end. The input is from the Pre-Stabilized Laser (PSL), which is briefly described in the Appendix. The three suspended Mode Cleaner mirrors are IMC1, IMC2, and IMC3. The filtered beam is then routed to the power recycling mirror (PRM), and towards the corner Michelson via PR2 and PR3. The PRC mirrors are also suspended as triple pendulums.

The Michelson cavity motion at low frequencies is larger than the IMC, ranging from several 100's of nm to 1 µm rms, and chiefly due to tilt injection (frequencies less than 0.1 Hz dominate the rms), from both the ground and platform sensing noises. The similarity between the spectrum of the cavity control and the Stage 1 CPS is of significance and will be revisited in the following chapter. The cavity control falls off rapidly above 0.1 Hz, due to both the active isolation and the multiple suspensions (quadruple for test masses, triple for the beamsplitter), see Figure 3.39. The difference in transfer function between these two species of suspensions interferes with any common mode rejection this short cavity might experience. The hope is that the control signal would approach the platform motion, filtered through the passive isolation of the suspension, but there is some excess above the microseism indicating the presence of another noise source, a misunderstood mechanical coupling, infidelity of the witness sensors, or some combination of all of the above. Motion in the recycling cavities is similar to the Michelson below 0.1 Hz and above a few Hz, but is significantly higher in the important microseism frequency band. This is due to the relatively less isolated HAM platforms, some

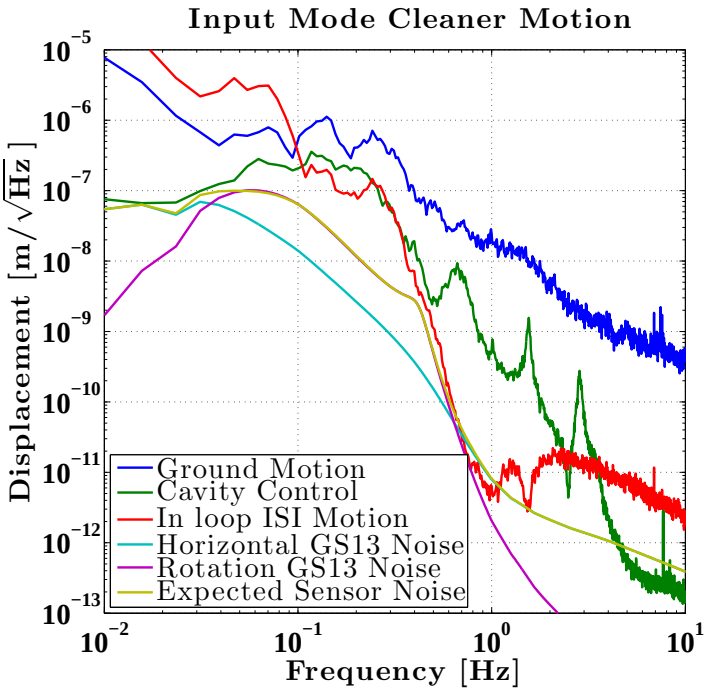

FIGURE 3.38. Spectrum of the control signal applied to the mode cleaner mirrors to maintain cavity resonance, as well as some of the motion sources. Noise expectation from the platform sensing limits is also shown, and the control signal approaches this level at very low frequencies, below 0.1 Hz. The rms control is between 50 and 100 nm, well below the range of the suspension actuators.

of which contribute multiple times to the cavity motion due to multiple reflections on the mirrors they support and due to supporting multiple mirrors in the folded cavity.

With the seismic controls scheme described here the differential arm cavity motion should resemble the short Michelson cavity motion to a high degree, since the direct longitudinal coupling effectively involves the same number of platform motions (four), each tilt dominated below 0.1 Hz. At frequencies above 1 Hz there will be a significant difference due to the inclusion of only quadruple suspensions in the DARM DOF, whose isolation is increasingly more powerful than the triple suspension supporting the beamsplitter in the short Michelson. Figure 3.40 shows that the expected low frequency similarity is present, with the cavity control below

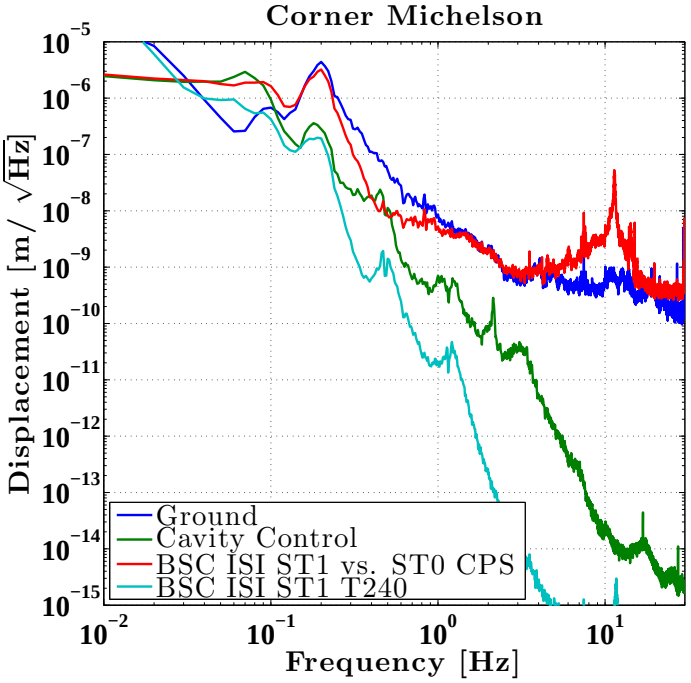

FIGURE 3.39. Spectrum of Michelson cavity control signal, as well as the ground input and isolation platform witnesses. Below 0.1 Hz the cavity control is due to platform noise, and is in excess of the ground motion. Above 0.1 Hz the cavity control rapidly reduces, due to both the active isolation and suspension roll-off. The isolation is not as good as expected by the inertial witness on the isolation platforms. The position sensors make a good witness of the injected motion below 0.1 Hz, and above this they are dominated by input noise (except for the region around 0.5 Hz, where some sensor correction is implemented). For this graph the ST1 T240 was filtered through the triple suspension of the beamsplitter.

0.1 Hz roughly corresponding to an incoherent combination of the 4 platforms motions (there is not much correlation between the ground motion/tilt over the long arm, except in the presence of earthquakes), again using the Stage 1 CPS signal as a witness of the injected horizontal motion. Above 0.1 Hz, as with the short Michelson, there is also an excess motion reported in the DARM control signal, when compared to the in-loop inertial sensor on Stage 2 of one of the involved platforms (all are similar in their performance), and identifying exactly the source of the control signal will most likely be an important feature of the near-future commissioning.

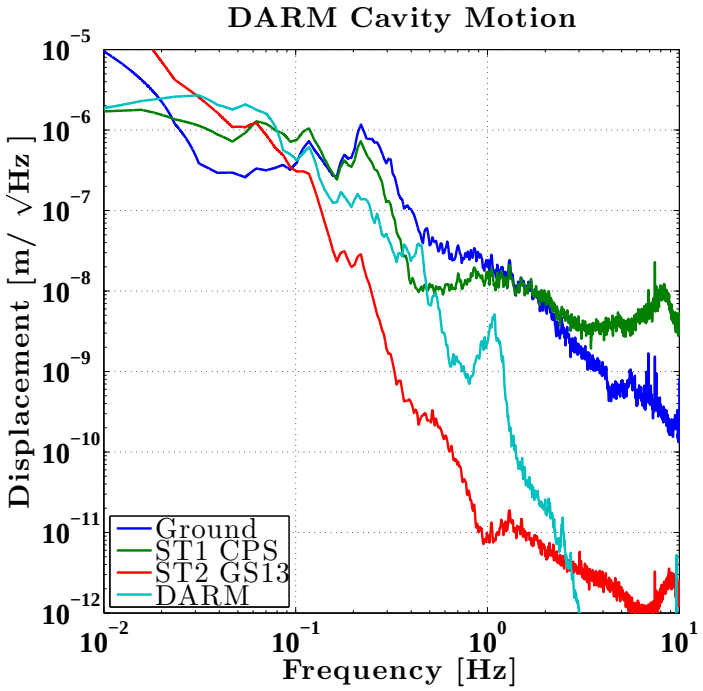

FIGURE 3.40. The DARM cavity control signal as well as example platform motions. Similar to the short Michelson, which includes the same number of BSC ISI longitudinal DOFs, the Stage 1 CPS signal is a good prediction of the cavity motion below 0.1 Hz, where the majority of the control signal rms exists. While the control signal reports motion less than the ground at all frequencies above 0.1 Hz, the isolation witnessed by the in-loop inertial sensors on the second stage of the isolation platform is not a very good match for the mirror motion.

.

4

Low Frequency Controls Improvement

A running theme of the previous chapter was the difficulty created by tilt of the ground or the platform in reducing the low frequency (< 0.1 Hz) motion of the mirrors. We seek to maximize duty cycle and minimize technical noise injection at the lower edge of the detection band; each of these goals is helped with improved low-frequency disturbance control. The duty cycle issue stems from the reliance on stochastic locking procedures, where the initial resonance conditions of a cavity are arrived upon by the chance positioning of the mirrors followed up by a rapid application of feedback control. This was somewhat alleviated in second generation detectors, see the brief aLIGO lock acquisition description in Appendix E and the references cited there.

Noise concerns center on bandwidth requirements of auxiliary (that is, not differential arm length) control loops creating in-band noise couplings to the gravitational wave readout DARM. Examples of this are the corner length controls, i.e. MICH and SRC, and the angular control servos which maximize the circulating power and signal build-up by holding an optimal mirror alignment. While the angular servos typically have bandwidths below the signal band, stability requirements will always limit the amount of filtering above the unity gain frequency

which is allowable. Other servos which need suppression requiring control bandwidth at signal frequencies, as is the case for MICH and SRC, then their noise coupling must be subtracted either in real-time or in post-processing [89]. With the aLIGO design expecting to realize high sensitivity all the way down to 10 Hz these technical noises are serious obstacles, and anything which can be done in pre-isolation to relieve the controls can help.

4.1 Intermediate Mass Black Holes

From the astrophysics perspective, one of the motives for pushing the detection band lower is the possibility of studying intermediate mass black holes (IMBHs). The term "intermediate" is applied because such an object would have a mass greater than a stellar mass black hole (resulting from the collapse of a star), but less than a super-massive black hole (formed at the center of a galaxy), that is to say, 25 $M_\odot \lesssim m_{\rm IMBH} \lesssim 10^5$ $M_\odot$. Potential IMBH formation mechanisms include a chain of collisions inside a cluster of stars [1] or even density fluctuations in the early universe, when the absolute density was very high (not only producing IMBHs, but gravitationally collapsed regions over a wide mass range)[90]. Studies of X-ray sources can be used to locate compact objects in the mass range of IMBH's [91], with a ∼400 solar mass object discovered this way [92].

Inspiral chirp signals don't increase in frequency indefinitely, with the process stalling either when the objects begin to merge or when their separation reaches that of the "inner-most stable circular orbit" (ISCO). The gravitational wave signal amplitude is also largest when it reaches this configuration, and the frequency (in Hz), $f_{\rm ISCO}$, is roughly given as

$$f_{\rm ISCO} \sim 4400 \frac{M_\odot}{M}, \tag{4.1}$$

where M is the total mass in the binary system. For a binary system where one of the constituents is an IMBH, the combined mass could potentially be 100's or 1000's of $M_{\odot}$, with a f_{ISCO} in the 1 to 100 Hz region.

4.2 Improved Sensing

The most effective combatant against low frequency motion would be good sensing of inertial tilts. This could be achieved through dedicated tilt sensors, or by the combination of vertical seismometers. Low noise, low frequency inertial tilt meters has been an active topic of research within the precision measurement community for some time [93, 94], and the proposed requirements specifically regarding LIGO isolation systems has been examined in some detail [95].

While the vertical sensors used should be considered low-noise, low-frequency devices, the tilt coupling is such that even sensing noise limited rotation controls will produce tilt dominated horizontal controls, as visible in the noise budgets of the previous chapter. There has been some progress in what may be called ultra-sensitive seismometers, which forego the more common electrical readout schemes of commercial seismometers for an interferometric readout [96]. There is, additionally, the possibility of making use of the horizontal seismometers themselves as a component of the vertical control loop's error point. The platform rotation controls are largely sensor noise limited at low frequencies, whereas the tilt signal has very high SNR in the horizontal seismometers.

Using the noise budget model of the previous chapter it is possible to estimate the motion of a platform outfitted with improved tilt sensing, after designing some new control filters, and this section will compare the three potential schemes mentioned above. A modified signal diagram for the first stage of the BSC ISI, using the horizontal signals as both seismometers and tilt-meters, is shown in Figure 4.1. A noise

budget projection, assuming a tilt-meter meeting the proposed requirements was placed somewhere on the technical slab next to the seismic platform, is shown in Figure 4.2. Figure 4.3 assumes several interferometrically sensed seismometers are placed on the isolation platform as the vertical motion sensors, spatially separated and to be combined for tilt sensing. In this order, these futuristic configurations will be referred to as A, B, and C. The dedicated tilt-meter of configuration B is left on the technical slab due to its probable size, whereas the optically sensed seismometers of configuration C have form factors which are almost (if not truly) identical to the units already able to be placed on the platforms as designed. No hardware change is required for configuration A.

The success of configuration A rests on effective discrimination of tilts from horizontal signals in the seismometer output. If both the low frequency horizontal motion and tilt motion are assumed to be roughly flat with respect to frequency, then a good estimate of the tilt component of the signal can be made with the known coupling. The assumption that the horizontal motion becomes flat is not without merit, since this is commonly seen in the less tilt-corrupted vertical readout. Nevertheless, any true statement about this model for the seismometer output would need to be tested, ideally, with one of the interferometric cavities.

Taking for granted that tilt signals generate the low frequency turn up of the seismometer output, a typical seismic spectrum from the Livingston site would have a $\sim$75 mHz crossover frequency. In order to enable the tilt sensor application of the horizontal seismometer, an extra set of complementary filters must be added, where the blend frequency is the tilt-displacement crossover of 75 mHz. Once this split is made, the low-passed component of the signal is converted to angular motion via $RY = X\omega^2/g$, and then filtered for addition with the rotation loops CPS and inertial sensors via a band-pass filter. An immediate problem arises,

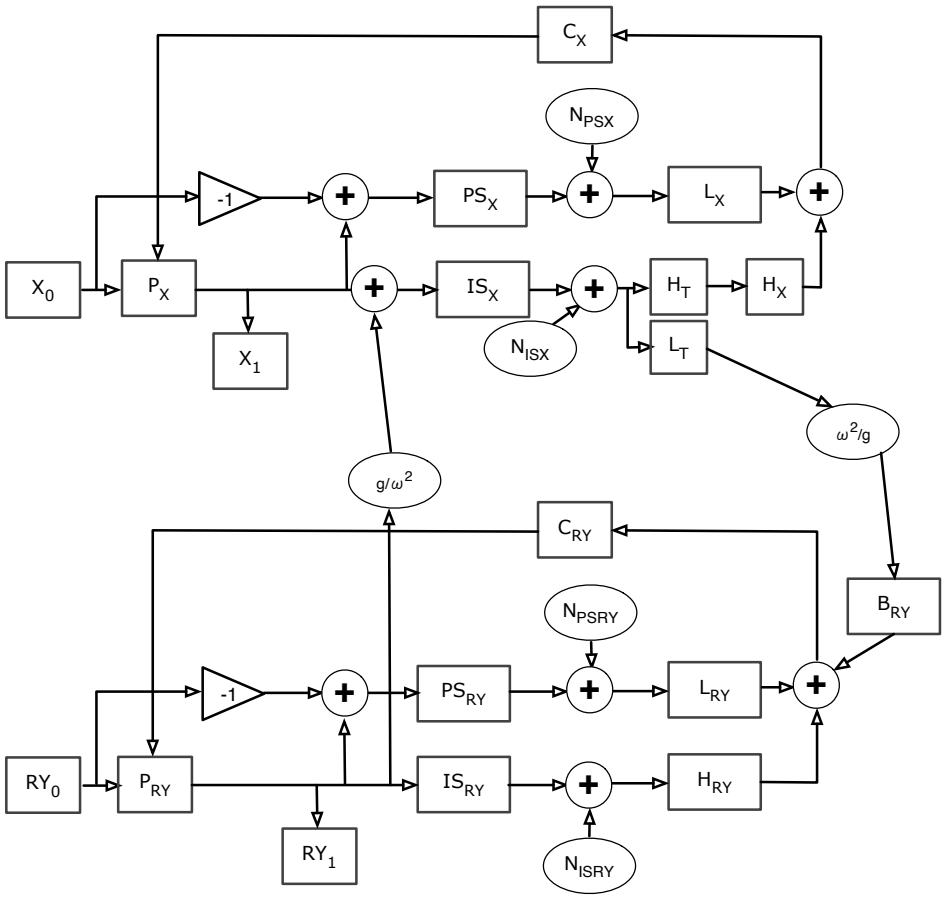

FIGURE 4.1. The two loop model with the inclusion of a "tilt-meter" formed by the low frequency (and assumedly tilt-dominated) horizontal inertial sensor's signal. An extra pair of filters, H_T and L_T, such that $H_T + L_T = 1$, are added to split the signal into its displacement and tilt regimes. After converting m to rad another filter, B_{RY} blends it into the error point of the rotation control loop. In order for the horizontal loop to remain stable, H_X must be modified with $1/H_T$, sacrificing some filtering.

however, in that in order to maintain stability in the horizontal control loop the high-pass filter, H_X, must be corrected with the inverse of the tilt-displacement blend H_T. Inevitably this results in less filtering of the platform tilt, partly or wholly defeating any improvement in the inertial tilt motion of the platform. This unfavorable trade-off, coupled with the relatively severe SNR comparison between the band-passed horizontal signal and the vertical sensing, as well as issues of control stability, make the successful pursuit of such a scheme unlikely.

Configuration B's use of the ground-based tilt-meter is most likely best achieved by first cleaning the horizontal sensor correction signal of tilt corruption before combining it with the Stage 1 CPS. With sensor correction providing the isolation at the microseism the horizontal blend frequency is shifted upward to around 100 mHz, with the additional high-pass filtering moderating the coupling of platform tilts. Any higher and the horizontal isolation around the suspension resonance would begin to be unacceptably compromised.

Again, the tilt-meter noise curve used for the calculation in FIgure 4.2 is simply the requirement curve posted in [95], and the propriety of the requirement can be seen by the tilt meter noise coupling neatly tucked beneath the residual ground motion. This model uses approximately a median input seismic spectrum for the Livingston observatory. While some reduction in the rms control of the table is achieved over the already available sensors, the vertical sensing limits of the platform interfere with effective rejection of tilts. This can be seen by examining the narrow gap between the coupling of Ground RY and the RY CPS noise in Figure 4.2. Since the RY T240 noise is barely below either of these couplings, neither blending higher nor lower will succeed. During times of large ground tilt, produced for example by strong sustained winds, the efficacy of the ground-based tilt-meter will scale well, and it may be appropriate to employ them for this reason alone.

Regarding configuration C, given the very low noise of the instruments reported in [96], the rotational blend design immediately becomes somewhat foreign to the experience gained so far with the aLIGO active isolators, in that the crossover frequency between position control and inertial control can seemingly be very low, 1 mHz or less. The projected noise budget uses a rotational blend around this frequency, although there is still a significant gap between the position sensor noise and interferometric sensor in this configuration (that is to say, the blend could be

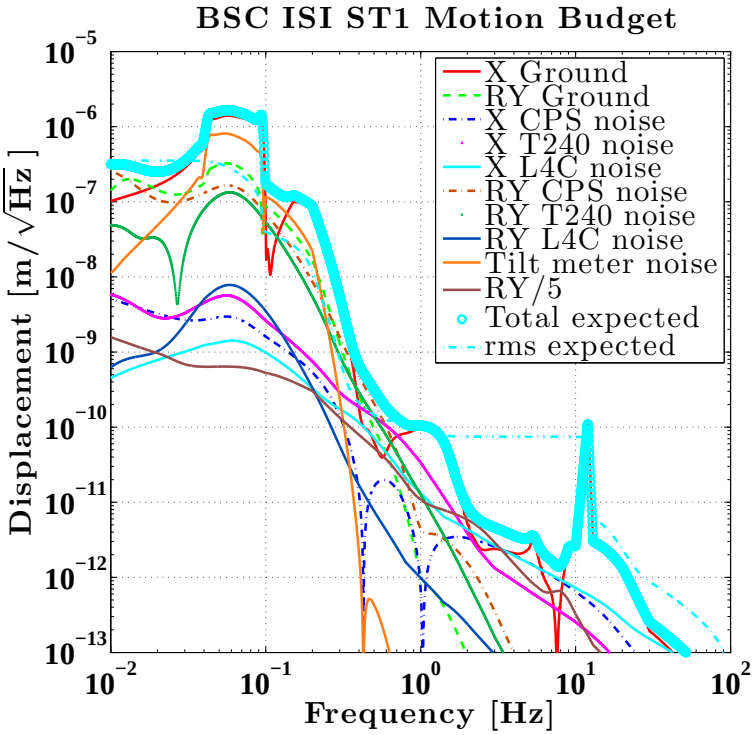

FIGURE 4.2. A projected noise budget for a BSC ISI where the use of a ground based tilt-meter generates a filtered seismometer signal to be used for sensor correction. The horizontal blend frequency increases to make use of the sensor correction at the microseism, but sensing of rotations by the platform's on-board sensors creates difficulty in realizing greatly improved performance.

lower from a noise perspective). It is not known what practical problems could occur when inertially isolating tilts down to such low frequencies with feedback, although notably the range of the actuators should *not* be a problem. It follows that the blend frequency in the horizontal DOFs can also be lowered, since its chief restriction in the first place was unwanted tilt at low frequencies. The improvement over current sensing schemes around the microseism is a factor of several to ∼10x, and the overall rms motion in horizontal decreases from several 100's of nm to several 10's of nm. Around the suspension resonance there is a more modest improvement, and above this the motion is not much changed. The direct coupling of tilt to suspension point motion via the lever arm between the center of rotation of the platform and the optic's attachment is suppressed to negligible levels.

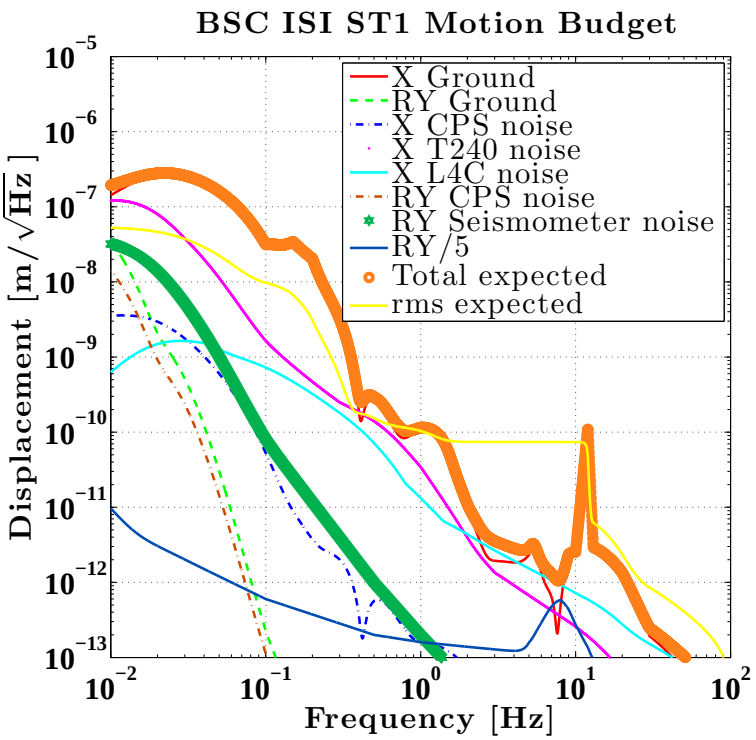

FIGURE 4.3. A projected noise budget for a BSC ISI where the vertical inertial sensors on Stage 1 possess noise floors similar to interferometrically sensed seismometers described in recent literature. The increase in vertical sensing performance allows for the isolation of inertial tilts down to very low frequencies, which relieves some of the filtering demands on the horizontal controls and pushes the overall platform motion to lower levels.

4.3 Suspension Point Interferometer

Probably the most comprehensive effort to alleviate the problems of low frequency controls is the *suspension point interferometer* (alternatively referred to as a *seismic platform interferometer*, but both abbreviated as SPI). The goal of such a system is not necessarily to suppress the motions of the platforms with respect to inertia, but to establish their relative motion, as will eventually be done by the interferometric controls, and suppress that instead. Very low range, low noise actuators could then be used for the mirror positioning. Several prototype systems have been developed using auxiliary laser beams between two platforms separated by ∼10 m [97, 98].

Logistically, deployment of a suspension point interferometer in a LIGO interferometer would most easily be achieved in the corner station, so the length scales of those prototypes is relevant. The rms residual motion of such systems has been demonstrated to be 1 nm or less [97], on the order of 1000x less than the rms control signals of the LIGO cavities.

As with the main interferometer, there are several noise sources which must be considered for effective use of an SPI. One of the main obstacles for obtaining residual motions less than $\delta x = 1$ nm over $L = 10$ m is the frequency stability requirement of the light source, which must be stabilized to

$$\delta\nu = \frac{\delta x}{L}\nu, \tag{4.2}$$

or around 30 kHz rms for a $\lambda = 1$ µm source. For the low frequencies where an SPI tries to operate even a generally high-quality source will need some guard against thermal drift.

In the absence of a dedicated system for differential isolation of the platforms, there exists the possibility of utilizing combinations of the sensors already on the platforms in the corner station. Below 0.1 Hz the Stage 1 CPS is a good witness of the platform motion, since it is dominated by tilt and sensing noises both of which will always be formed as relative signals. The "Michelson" combination of platform sensors proves to be a strong predictor of the same cavity's control signal, see Figure 4.4. Unfortunately, the nature of the CPS does not allow it to be useful for subtraction from an individual platform's motion, since above 0.1 Hz it measures mostly the input motion (the other half of its reference, the platform motion, being much smaller), such that significant re-injection of ground motion would occur in a subtraction scheme. However, for the short cavity, where the

ground motion is common mode, the "Michelson" combination of CPS signals preserves the tilt injection information with much less danger of seismic motion re-injection. By constructing the differential CPS signal in the real-time software, and feeding it to the cavity mirrors, before the optical feedback loop is closed, lock acquisition can be eased by "slowing down" the Michelson fringe. Once locked this path can be ramped down, since the CPS is considerably more noisy than the optical sensing above 1 Hz, see Figure 4.5 and Figure 4.6.

Once combined, the CPS signals must be filtered with an approximate inversion of the suspension plant. The penultimate stage is used for this actuation, so the plant can be modeled as a double pendulum, with the primary longitudinal resonance around 0.4 Hz. Several structural resonances of the seismic platform's support (i.e. HEPI) must also be notched out, since they are sensed very loudly by the CPS and would inject too much motion around the suspensions vertical ("bounce") and roll modes. Although in theory no diagonal coupling should exist between the length drive and these modes, in reality some amount of coupling exists and they can be rung up by the application of control signals and generate instability in the feedback loops.

For clarification, the effectiveness of such a scheme is not from the improvement of the inertial motion of the cavity mirrors. Indeed, they are moving *more* with respect to inertia when the CPS feed-forward is enabled, but much less with respect to each other. In the corner recycled interferometer, feedback control of the cavities is dynamically engaged, by triggering on the intra-cavity power when resonance conditions are met, by accident, when the mirrors swing through the appropriate positions (referred to as a cavity "flashing"). The control bandwidth must be sufficient to stop the mirrors in place, overcoming their relative velocities at that moment. The CPS feed-forward can assist in this process, since the relative

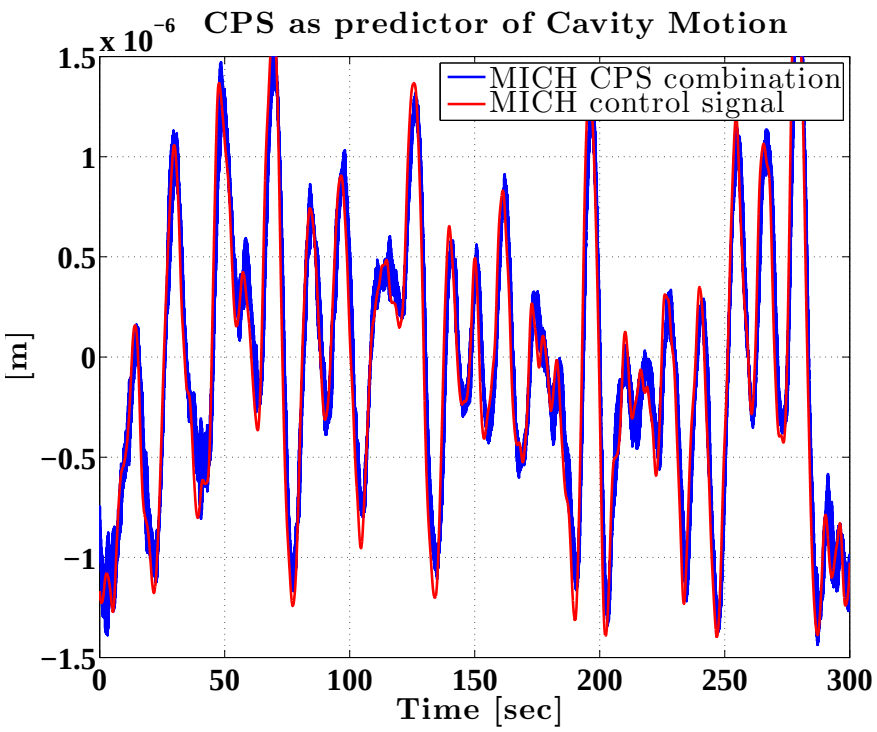

FIGURE 4.4. Time series of the Michelson cavity control signal, as well as the "Michelson" combination of position sensors, that is: $ITMX_{\mathrm{X}}$ vs. BS_{X} minus $ITMY_{\mathrm{Y}}$ vs. BS_{Y}. The motion is dominated by frequency components below 0.1 Hz, due to tilt-horizontal coupling, with the tilt itself sourced by both the ground and the platform controls.

velocity is decreased before acquisition, relieving the bandwidth requirements of the feedback loops by reducing the size and slope of the locking transient. This is especially important for servos, such as the Michelson, which have limited bandwidth due to actuating not on the mirrors itself, but on the higher stage pendulum masses.

Investigation of the recycling cavities' motion did not yield such useful results. These cavities compare the motion of mirrors supported by HAM ISI's against mirrors supported by BSC ISI's, and the weaker performance of the HAM ISI's around the microseism, exacerbated by the multiple reflections off two of the three cavity mirrors, results in controls signals which are not dominated enough by low frequency tilt-injection. As such, the "PRC" and "SRC" combination of CPS sig-

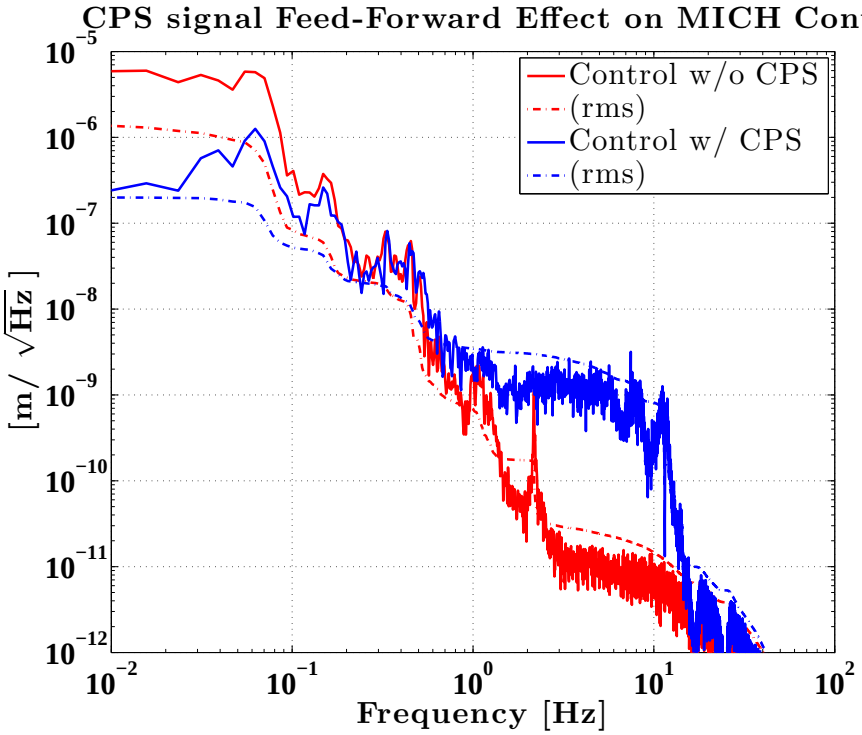

FIGURE 4.5. Spectrum of Michelson control with the CPS feed-forward engaged, and without. The rms reduction of ∼8x is provided to the cavity previous to lock acquisition, but the extra noise from CPS sensing requires that the feed-forward be ramped down after lock is achieved.

nals is a poor predictor of their cavity motion. The PRC and SRC feedback loops use the bottom stages of the recycling mirrors as actuators, and correspondingly their bandwidth is significantly higher than the Michelson DOF, by a factor of ∼5-10x. With the Michelson loop being the limiting factor in fast and reliable locking, an improvement in locking of the Michelson DOF via CPS feed-forward may prove an important defense against excess low frequency motion, for instance during times of high wind.

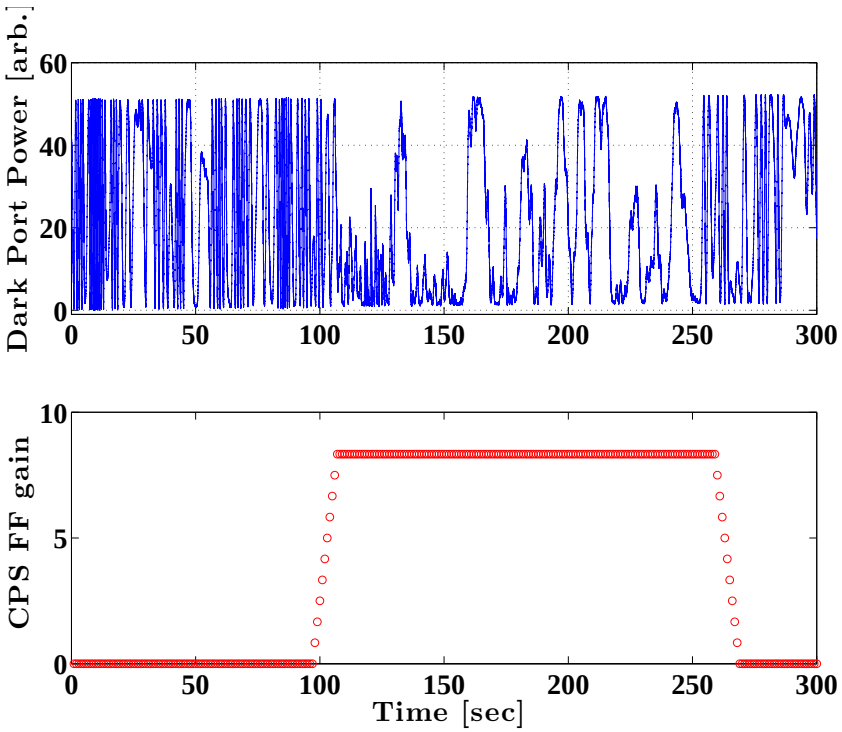

FIGURE 4.6. Time series of the Michelson cavity freely fringing, as seen at the dark port. When the CPS feed-forward is engaged, the fringe slows down visibly.

5

Backgrounds

Detector performance is not only gauged by the stationary sensitivity or duty cycle, but also by the amount of background events produced which compete with true events in the signal searches. Any experimental result relies on some estimation or measurement of the background, which gives a statistical significance and confidence for each claimed real event. For LIGO it is not possible to make a dedicated measure of the instrument background, since there is no way to "turn off" astrophysical signals as a null test. In the absence of a background measurement a number of cuts or *vetoes* are applied to reject background events, including the timing coincidence between separated detectors, and, for the searches with modeled waveforms, the degree to which the detected signal fits the expected waveform. Some number of potential false alarms remain, and any technical modification which can reduce them may increase our ability to make detections, even if not specifically lowering the noise floor of the instrument.

As mentioned in Chapter 4, the performance of the isolation systems below the signal band is not only important for maintaining a high detector duty cycle, but also because large signals at low frequency may couple into the signal band via non-linearities, a process referred to as *upconversion*. Several classic examples of upconversion exist, with perhaps one of the best known being the "flicker noise"

generated in certain kinds of resistors, which manifests as a $1/f$ voltage noise spectrum, proportional in size to the DC current applied [99]. This noise is due to current dependent fluctuations in the resistivity of the resistor material, and is in excess of the thermal (Johnson) noise $V_{\mathrm{thermal}} = \sqrt{4k_{\mathrm{B}}TR}$, where k_{B} is Boltzmann's constant, T is the temperature of the resistor, and R is the resistance.

For LIGO this phenomenon often, although not exclusively, occurs in the low noise electronics, when they are pushed outside of their region of linear operation, sometimes referred to as a "soft saturation". Also, the multitude of servo loops used to operate the detector can complicate matters by converting pulses into broader-band, frequency shifted noises via the controller's impulse response. Residual couplings (both linear and cross) between the servos often leads to a situation where a presumably auxiliary channel interferes with the sensitivity of the DARM measurement (everything is connected to everything else, and if its not our servos will make it so).

5.1 Template Searches

In contrast to the previous chapters, different measurement tools than the spectrum are needed to characterize which are typically non-stationary. Spectrograms are useful for displaying the time evolution of the spectrum, and there is an additional tool in template searches similar to the software used to find gravitational wave signals. When performing such a search the decision must be made what kind of waveform best epitomizes the kind of transients which are being investigated. When the signal being searched for corresponds to a well known waveform, as is the case with binary inspiral signals, matched filtering can be used to maximize the signal-to-noise ratio [100]. On the other hand, when modeling is computationally difficult or a physical phenomena is not well understood, an un-modeled approach to finding

burst signals relies on waveforms which only constrain the signal over some time period and to some frequency band. In general, the search involves constructing an orthogonal set of waveforms or wavelets and calculating an overlap with the signal time series at every time span of the waveform bank. Once each of these time-frequency "pixels" is calculated, with loud bins (exceeding some pre-defined threshold) being identified as triggers.

Useful waveforms for un-modeled bursts include both hard-edged square wave packets [101, 102] and smooth, sine-Gaussian wave packets [103, 104], the latter of which was chosen to serve as the basis for characterization the isolation system. A sine-Gaussian waveform has the form

$$y(t + t0) = y_0 \sin(2\pi f_0 t) e^{-t^2/\tau^2}, \tag{5.1}$$

where y_0 is the characteristic amplitude of the waveform, t_0 is the peak amplitude time, f_0 is the center frequency, and τ is the time constant of the exponential envelope. The center frequency is so called because the Fourier transform of $y(t)$ is Gaussian and peaked at the frequency f_0. Taking the Q parameter to be $Q = \sqrt{2}\pi\tau f_0$, the standard deviation of the Gaussian in the Fourier plane will be $\sigma = f_0/Q$.

Since the sine-Gaussian is characterized by a time, frequency, and Q (or bandwidth), these can be used a consistency checks when searching for the same signal in two data streams, like the separated LIGO detectors. This is analogous to the consistency between modeled waveforms for the inspiral search. These consistency checks also allow for the estimation of the background rate, using a time-shifted analysis of the two data streams. By shifting one data stream with respect to the other, by an amount much larger than the conceivable coincidence window ($\sim$10

s for the two LIGO detectors),and counting how many triggers pass all of the consistency checks, since by definition such a coincidence must be accidental. By comparing the counts for a variety of timing shifts the distribution of background estimates can be formed, and a mean rate quoted with some error.

Often times the strength of a signal identified by a search is given in terms of the waveforms root-sum-square value, which for a sine-Gaussian is given by

$$y_{\rm rss} = \sqrt{\frac{y_0^2 Q}{4\sqrt{\pi} f_0}}, \tag{5.2}$$

when the Q is more than a few. Importantly, y_{rss} has the same dimension as an amplitude spectral density. An example basis waveform is shown in Figure 5.1, where $y_0 = 1$, $f_0 = 10$, and $Q = 10$.

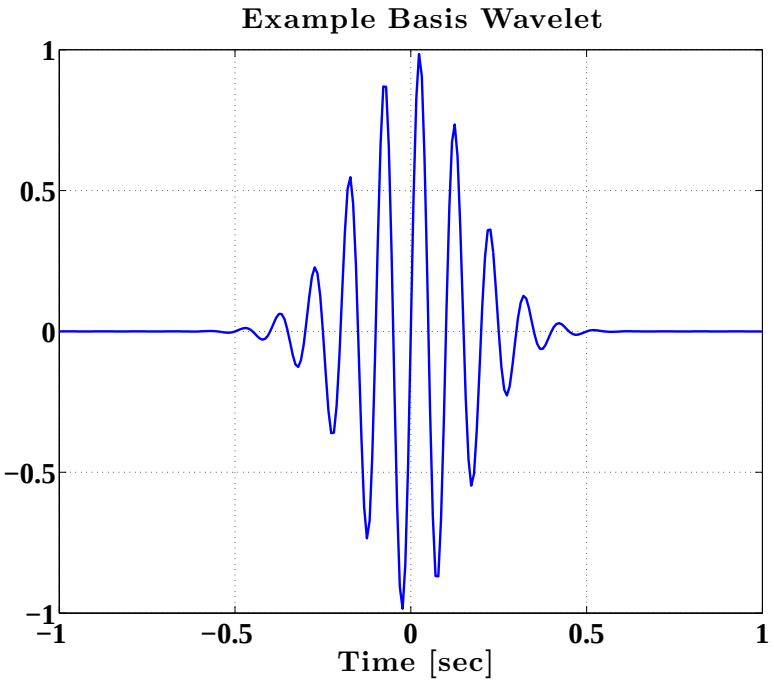

FIGURE 5.1. Example basis waveform for template search.

The search analysis is performed by combining the wavelet, a windowing function, and the signal time series in a calculation called the Q-transform [103]

$$X(t_0, f_0, Q) = \int_{-\infty}^{\infty} x(t) w(t - t_0, f_0, Q) e^{-2\pi i f_0 t} dt \tag{5.3}$$

where $w(t - t_0, f_0, Q)$ is the windowed wavelet, $x(t)$ is the signal time series, and the calculation is cycled over a template space populated with enough resolution to provide time and frequency localization. If the time series $x(t)$ consists of a signal, $y(t)$, in addition to some background noise, $n(t)$,

$$x(t) = n(t) + y(t - t_0, f_0, Q), \tag{5.4}$$

then the signal to noise ratio can be approximated as,

$$\rho^2 \simeq \frac{|y^2_{\rm rss}|}{S_{\rm nn}(f)}, \tag{5.5}$$

where $S_{\rm nn}(f)$ is the power spectral density of the background. If the Q-transform of $S_{\rm nn}(f)$ in the absence of $y(t)$, is $N(t_0, f_0, Q)$, then the signal to noise ratio can also be written as

$$\rho^2 = \frac{\langle |X(t_0, f_0, Q)|^2 \rangle}{\langle |N(t_0, f_0, Q)|^2 \rangle} - 1, \tag{5.6}$$

where the $\langle\ \rangle$ represent averaging over the relevant time-scale.

A Gaussian background will produce a number of triggers governed by $p(x) \propto e^{-\rho^2}$, and the amount of non-Gaussianity in the signal $x(t)$ can be gauged by how much it deviates from this power law.

5.2 Barkhausen Noise during eLIGO

Continuing on the discussion of Chapter 3's Section 4.2, one of the main achievements of the Wiener filter feed-forward to HEPI during S6 was the mitigation of upconversion effects. Figure 3.17 showed the reduction in feedback signal sent to

the mirrors to control the DARM degree of freedom, with the Wiener filter feed-forward providing an additional factor of ∼3x isolation. By reducing the size of the low frequency currents flowing through the suspension actuators below 1 Hz, a significant improvement in the burst rate at higher frequencies was realized. To characterize this improvement, a search, in line with the method described in the previous section, was run on the DARM signal for two consecutive 30 minute periods, one with the feed-forward enabled and one without. The input (seismic) noise did not change appreciably over the course of the test, and the results of the search show the improvement as fewer triggers during the feed-forward enabled period, see Figure 5.2. Each trigger removed in this fashion is one which can no longer compete with a true gravitational wave signal, so the overall background has been reduced. A spectrogram of DARM during the test also reveals a cleaner detector output signal, extending above 200 Hz, see Figure 5.3.

A possible cause of this upconversion is inherent in the design of the mirror actuators. They consist of a ferromagnet, glued to the back of the mirror, around which a loop of wire is placed, attached to the frame which supports the suspension. As the current flows through the coil winding a magnetic field is generated around the ferromagnets, exerting a force on the mirror. As the ferromagnetic domains flip their orientation, following the polarity of the applied field, their discrete nature manifests itself as Barkhausen noise [105].

Instead of a smooth response to the external field, the magnetization is a concatenation of small jumps corresponding to domain transitions, with the rate of pulses dependent on the derivative of the magnetization, see Figure 5.4, which is a reproduction of Figure 9.10 from [105]. The degree of Barkhausen noise introduced can mitigated by careful choice of magnetic materials or, as presented here, by

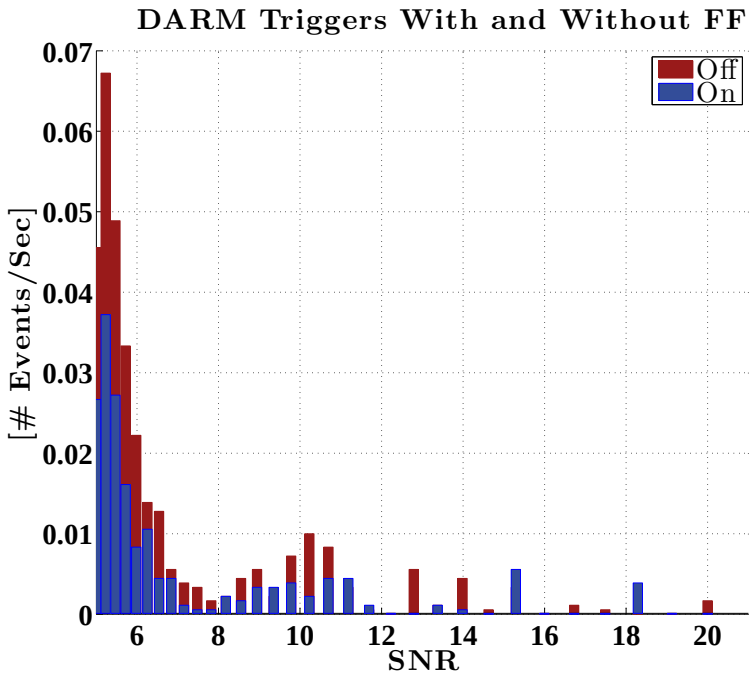

FIGURE 5.2. The output of templated search of the DARM channel during two time stretches when the optimized feed-forward was on and off. The threshold SNR for the search is 5, and as might be expected the majority of events are detected near threshold in both cases, but with ∼2x fewer when the feed-forward is enabled. The number of events with SNR > 10 is not significantly changed, suggested that they may be generated by a phenomenon apart from large low frequency current.

off-loading the control signal from the coil current to the HEPI actuators the rate of Barkhausen jumps will decrease, resulting in fewer bursts in the detector.

5.3 Background Rates in aLIGO Sub-Systems

One signal which can be relied upon to contain a large amount of transients is the output of the seismometer placed on the ground (or, more accurately, the concrete technical slab which itself is on the ground). While the overall rms variation is dominated by slow effects such as the weather at higher frequencies ($f > 1Hz$) pulses in the seismic sensors are caused by variations in local traffic patterns and gusts of wind. Given such a variable input, the isolation platform can also be judged on its ability to reject seismic pulses. On site activity can, of course, significantly

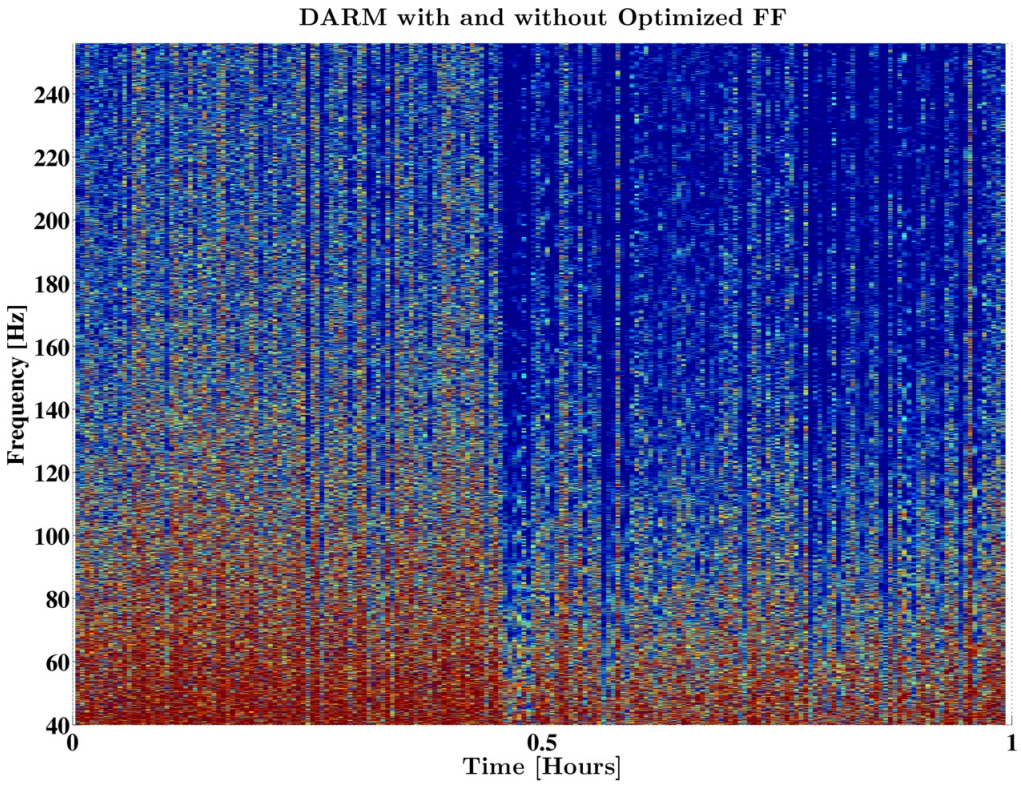

FIGURE 5.3. A spectrogram of the DARM signal during the feed-forward on/off test. Each row corresponds to a 10 second long power spectrum. At $t = 0$, the bottom of the y-axis, the feed-forward is disabled, and remains so until about 30 minutes into the test. From $t = 1/2$ hours and onward the feed-forward is enabled. The color scale represents the value of the spectral density, where the frequencies above 40 Hz have been somewhat whitened to reduce the dynamic range display requirements. This is only to display the relative spectral content, and to point out the breadth of the frequency band which improves when reducing drive currents around 0.1 Hz.

contribute to transient seismicity, but this is widely prohibited during data taking and so is inconsequential from the systems performance viewpoint.

Figure 5.5 is a spectrogram of the horizontal ground sensor in the corner station, spanning 10 hours, beginning around midnight. The onset of morning traffic is easily picked out around 6:30 AM, and the persistent microseismic activity can be seen dominated the spectrogram throughout its duration. Also visible is some wind activity beginning around 8 AM and characterized by its 20-30 Hz velocity. A burst search of this data set obligingly produces numerous loud transients, as can be seen in Figure 5.6.

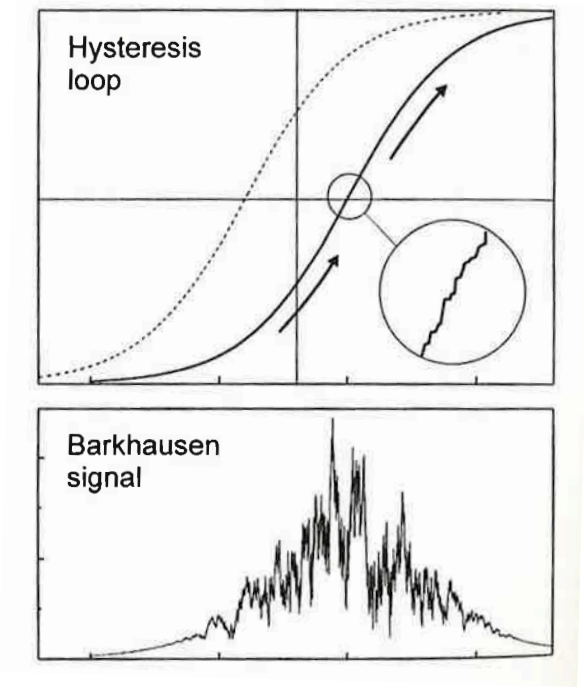

FIGURE 5.4. Depiction of the phenomena of Barkhausen noise. Magnetization by an smooth, continuous external field results, at small scales, in a discontinuous response made of jumps. The rate of Barkhausen pulses is maximum when the derivative of the magnetization is maximum. This figure is a reproduction of Figure 9.10 from Bertotti's book, *Hysteresis in Magnetism*.

Figure 5.7 shows the same set of triggers, calibrated into m_{rss}, and displayed against log frequency as is the "transient" amplitude spectral density. The binning (column separation at low frequency) is due to the tiling resolution in frequency space of the search, that is, all triggers between 1 Hz and ∼1.3 Hz are grouped into the first column on the left, etc. The separation between loudest and quietest trigger decreases as the frequency of the trigger increases, with most of the non-staionarity experienced below 10 Hz, consistent with the spectrogram in Figure 5.5.

The design of the Stage 1 BSC IS controls, and to a lesser extent the HAM ISI controls, specifically incorporates the day-time increase in $f > 1Hz$ seismicity. This is done by allotting enough low-passing in the CPS blend filter as well as overall loop gain at these frequencies to suppress the day-time 1 Hz motion to the Stage 1 sensor noise, or, in the case of the HAM ISI, as close as possible

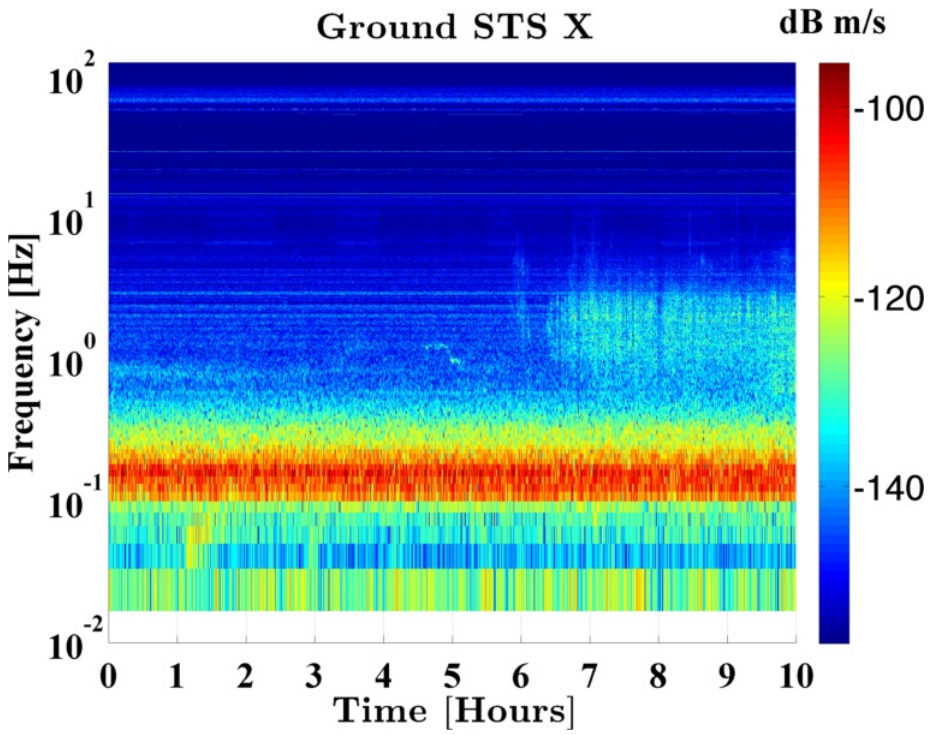

FIGURE 5.5. Spectrogram of 10 hours of seismic activity measured by the STS-2 sensor on the LVEA slab. Time zero, at the beginning of the X axis, corresponds closely to midnight. Local traffic begins around 6.5 hours into the data, marked by the ∼10 fold increase in 1-3 Hz seismicity. The red band which spans the entire data set is the secondary microseismic peak.

without compromising microseismic isolation. This extra isolation is largely useless during the night-time, and it could conceivably be optimal to rearrange some filter coefficients for dedicated night-time operation, but this is probably a task better suited to handling variation in the microseismic and even low frequency disturbances, which are more problematic due to their large amplitude.

Figure 5.8 contains the spectrogram of the Stage 1 in-loop inertial seismometer (the T240) for the same time period as the ground data above. Notably absent is the onset in 1-3 Hz motion around 6.5 hours into the data stretch, due to controls suppression. Also significant is the redistribution of the low frequency motion from the microseism, which is suppressed by the Stage 1 controls, at the cost of the even lower frequency tilt injection which now dominates the spectrogram.

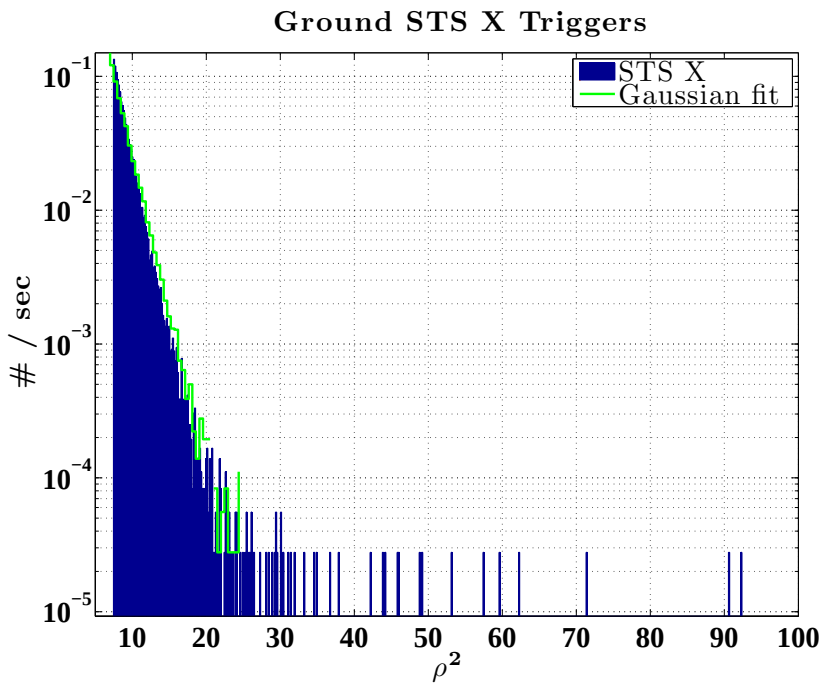

FIGURE 5.6. Result of a search for burst in the ground data, unsurprisingly populated with non-Gaussian transients due to local seismicity.

The persistently loud line at just over 10 Hz comes from resonances in the HEPI support structure and is a feature which is worth addressing. The 30 Hz line is from the fans in the building HVAC system, and, while loud in the spectrum, is less interesting due to the extreme isolation provided by the quadruple suspension at this frequency.

Figure 5.9 shows the output of the transient search, and although not totally reduced to a Gaussian background the number of loud triggers from the ground has been thinned out somewhat. Ideally the loop gain and blend configuration would be sufficient to completely suppress this channel into sensor noise except in the most extreme seismic disturbances.

Taking into account the contents of Figure 5.10 it seems that the ∼12 Hz resonant is both a standout feature in the spectrum as well as in the transient distribution, perhaps indicating that more efforts need to be applied at suppressing this. The

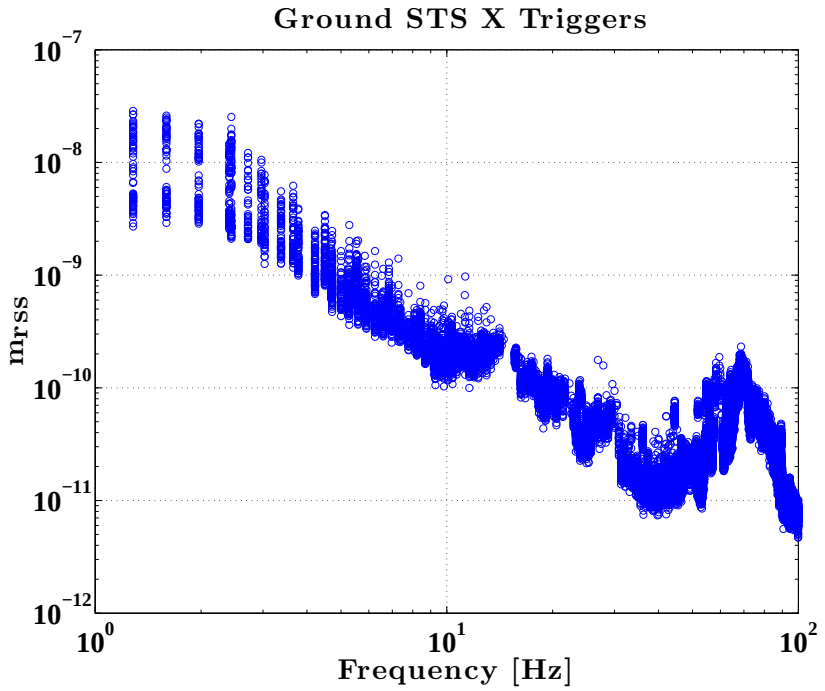

FIGURE 5.7. Plotting the triggers in the same style as an ASD (m_{rss} having the same unit) shows some variation in strength around 1-3 Hz, as might be expected from the spectrogram. The column separation at lower frequencies reveals the resolution of the search's frequency space tiling.

chief difficulty comes from limited bandwidth on Stage 1 due to imperfect plant inversion. A truly inverted plant transfer function is not ideal for other reasons, since the inevitable tuning of high frequency, high Q factor resonances will be required and these features are not static but will vary with temperature, leading to a high bandwidth but less robust controller.

With Stage 1 pushed generally to its sensing noise the Stage 2 loop design is less aggressive, although for the reasons stated above this is somewhat of a false optimization. In the error point, however, it is both hoped and expected that in the presence of both stage's control loops Stage 2 would not detect any transients, and this is close to the reality. Figure 5.11 shows the Stage 2 in-loop horizontal GS13 spectrogram, almost devoid of features except for the microseism, and the search result shown in Figure 5.12 confirms a relative lack of excess triggers. Figure 5.13

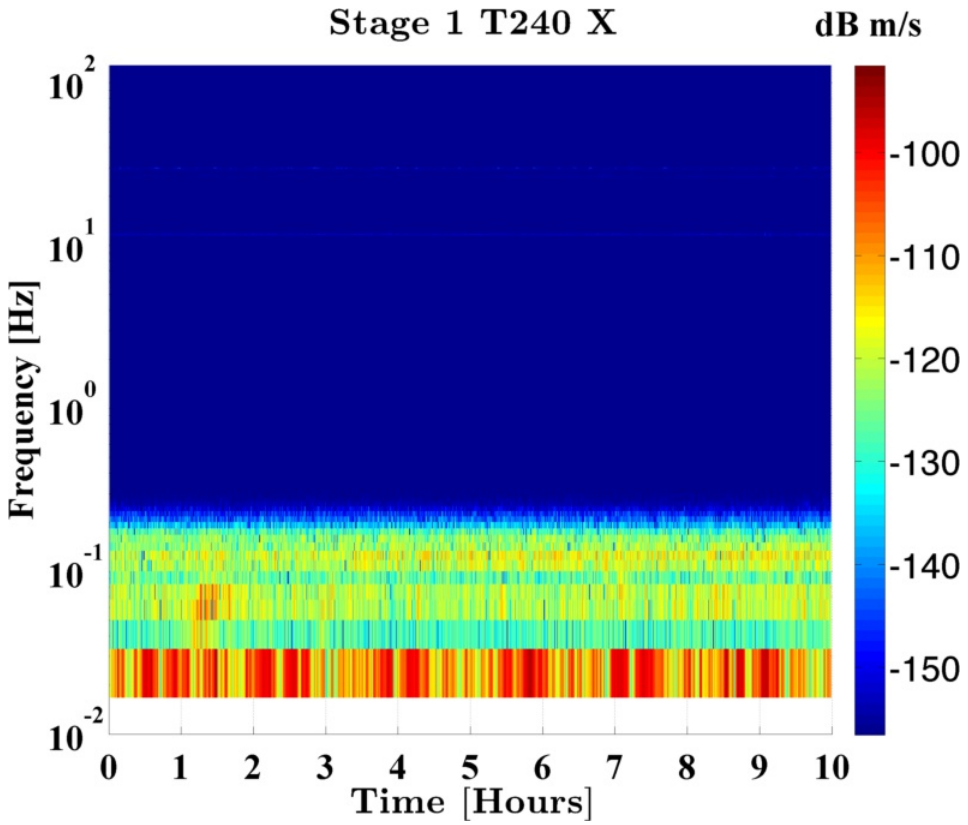

FIGURE 5.8. Spectrogram of the Stage 1 T240 horizontal signal, over the same 10 hours as above. Interesting contrasts include the absence of the transition to 1-3 Hz traffic induced motion, as well as the redistribution of low frequency motion from the secondary microseism (suppressed by the controls) to amplified lower frequency motion (impressed by the controls).

shows that, like Stage 1, a major feature is the 12 Hz resonance. In general, over long time scales spanning the day-night seismicity transition the isolation platform can be said to suppress transients effectively.

Using the data displayed in Figure 5.13 and the design isolation transfer function of the quadruple suspension supported by the BSC ISI a projection can be made for how detectable the loudest events sensed by the GS13 would be in the DARM signal, this is shown in Figure 5.14. Over 10 hours of data the loudest event is still significantly below even the most sensitive design curves available for aLIGO, assuming 125 W of input power.

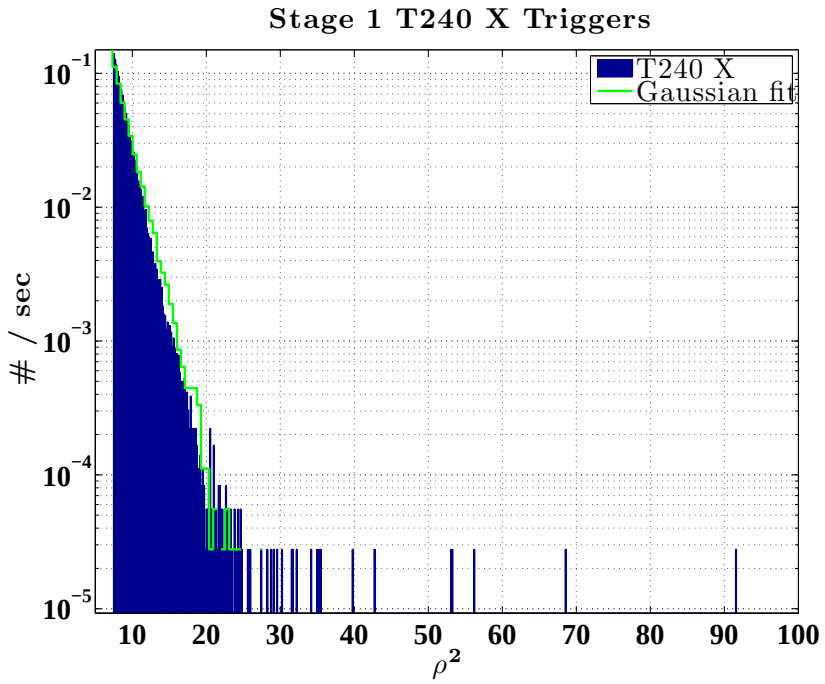

FIGURE 5.9. Result of a search for burst in the Stage 1 data. Since this is the error point of the control loop the presence of any non-Gaussian transients is undesirable.

With less passive filtering, and less overall loop gain, the story is somewhat different for the HAM ISI, although the conclusion is generally similar. Figure 5.15 shows the rate of triggers in a undisturbed HAM ISI, over 4 hours, with a similar event rate as the first stage of the BSC ISI, shown previously. This is not surprising, as the first stage loop gain is similar to a HAM ISI loop gain, and the chief differences between them occur below 1 Hz.

As a further test of the HAM ISI, a series of injections were performed, at various frequencies and amplitudes, to see if the local sensors could produce and traces of non-linearity from upconversion. The excitations were at 0.11, 0.51, 1.13, and 10.2 Hz, all frequencies where the ground input can vary significantly, and the uppermost drive levels were at least as large (or, in some cases, significantly larger) than the highest amplitude ground motion expected at the Livingston site. Figure 5.16 shows the amplitude spectral density of the HAM ISI in-loop GS13

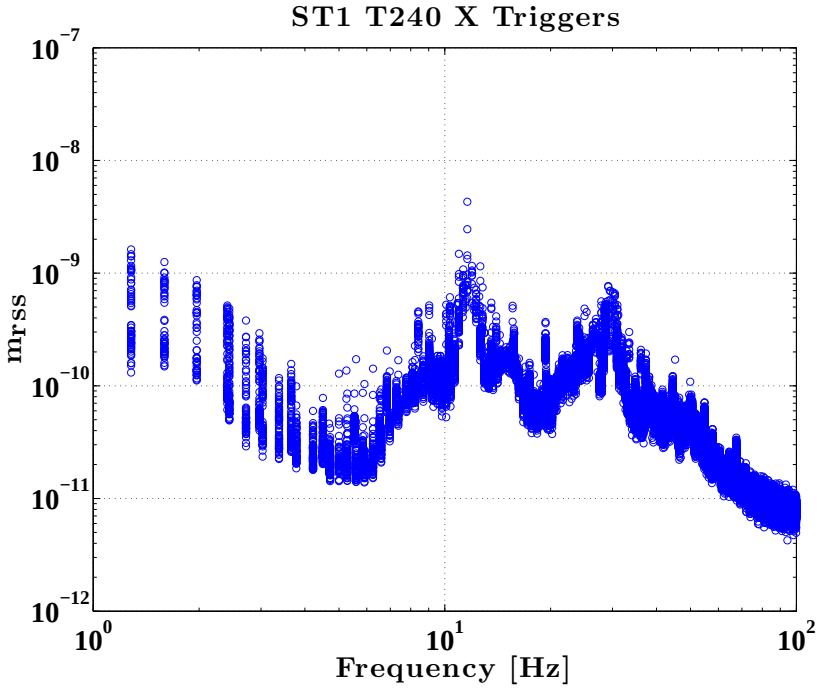

FIGURE 5.10. Transient size plotted against frequency. The ∼12 Hz support structure resonance shows significant variation. It is somewhat difficult to reconcile the degree of variation in the few Hz triggers with the spectrogram and the trigger distribution, and this may need further investigation although it is admittedly well below the signal band.

during all of these excitations, revealing little to no difference between data sets outside of the band of excitation. The only test with visible upconversion from the excitation is the drive at 10.2 Hz, although this is most likely not of any concern since the drive level was so large compared to the ambient motion, and the input seismicity never approaches this level of disturbance. Figure 5.17 shows the spectrogram of the inertial sensor for the duration of the microseism (0.11 Hz) injection, with the amplitude ramping up approximately every 15 minutes. In spite of the increased excitation, the spectrogram only reveals the decreasing anthropogenic seismicity during the test, due to the time of day it was performed at.

Figures 5.18, 5.19, 5.20, and 5.21 show the results of burst searches, for each test (frequency and amplitude). The rate of loud bursts is not shown to be particularly

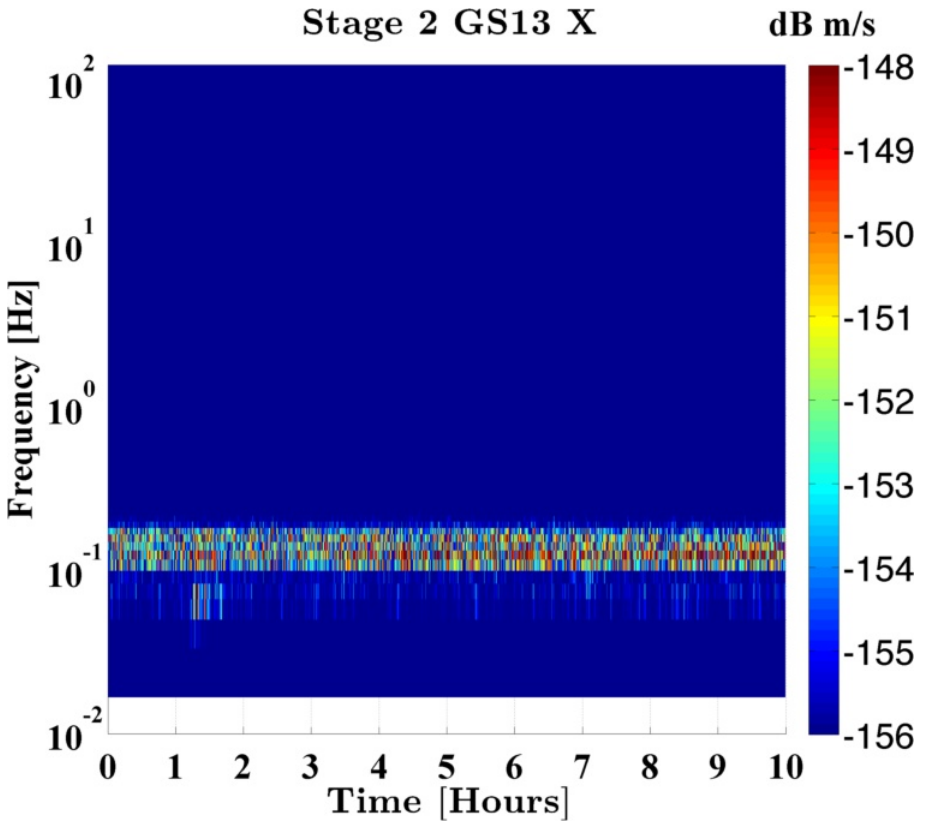

FIGURE 5.11. Spectrogram of the Stage 2 horizontal GS13 signal, for the same 10 hours as presented for the ground and Stage 1. Except for some microseism it is largely quiet during the entire stretch, with the low frequency tilt attenuated in this channel due to the uncompensated roll-off of the geophone (signals below 1 Hz are not as interesting for the transient analysis).

dependent on the presence of the excitations, and the overall rate of triggers is not significantly altered by the drive, except perhaps with the exception of the loudest injection at 0.51 Hz (Figure 5.19). Taking the calibrated amplitudes of all these triggers and plotting them against frequency shows a similar result for each set, and the loudest drive level of each excitation is plotted in Figure **??** (with some scaling applied to separate the data sets for visibility). With all of the data sets being comparable, one of them was chosen and propagated through the expected isolation transfer function of a triple suspension (the most common kind supported by HAM ISIs), producing a set of triggers with such small amplitudes that they would be difficult/impossible to detect with the sensitivity available in

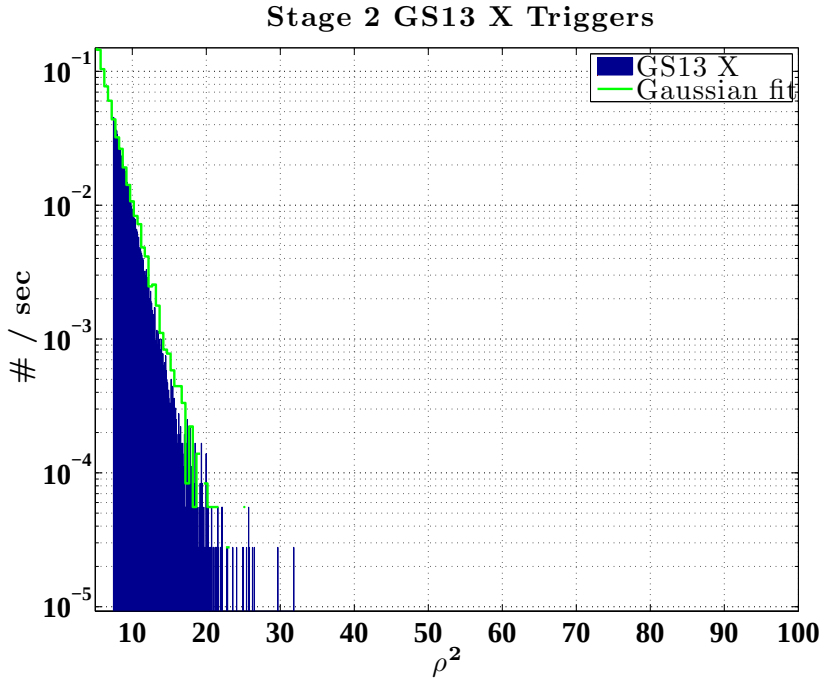

FIGURE 5.12. Result of a search for burst in the Stage 2 data. No significant excess of triggers is detectable in the most isolated stage.

the recycling cavities (the interferometric cavities which HAM ISIs directly couple to).

5.4 Upconversion in the PRMI

During the commissioning of the corner cavities, the Power-Recycled Michelson specifically, the available sensitivity was high enough that a series of injection tests for upconverted noise was made, using the interferometric signals as witnesses. The general idea was to examine the instruments sensitivity to large low frequency current drives on the mirror actuators, at the lowest (least isolated) stages of the triple suspensions in the PRC, searching for similar non-linearties as seen during iLIGO and eLIGO and described earlier in this chapter, and putting the conclusion of the previous section to test. While the corner cavities are, of course, interferometrically coupled to the quadruple suspensions of the input test masses, it

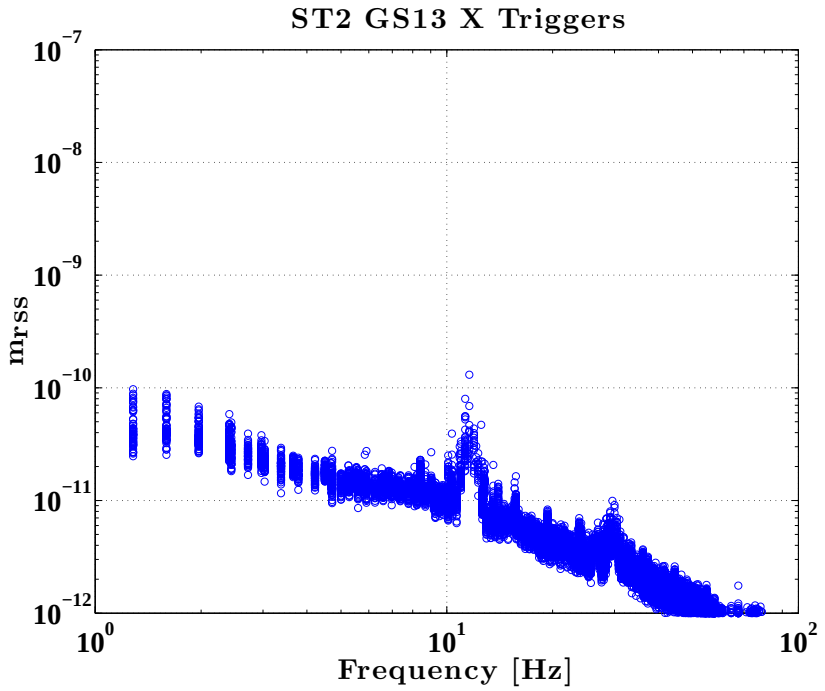

FIGURE 5.13. The 12 Hz feature leaks through the Stage 1 isolation into the Stage 2 motion, and is responsible for the few excess triggers visible in the Stage 2 search output.

was not possible to actuate the bottom stages of those suspensions and drive would have to be through at least a double pendulum, both complicating the experiment and making the PRMI sensitivity fairly poor for the task.

Initially the interferometer showed no response to the presence of the excitation, but this was due to the PRC's sensitivity to frequency noise (unlike the Michelson DOF, it does not experience common mode rejection by comparing two arms, but instead acts as a single Fabry-Perot cavity). Recall that the quiet frequency reference used for the gravitational wave measurement is the common length of the long arm cavities, which is not available with only the corner interferometer. Indeed, in this state the frequency servo consists of a wide-bandwidth (∼500 kHz) servo locking the main laser frequency to an isolated, in-vacuum reference cavity (a suspended fixed length spacer), and then feeding the error point of that servo with the less speedy but still fast ∼50 kHz) lock to the IMC.

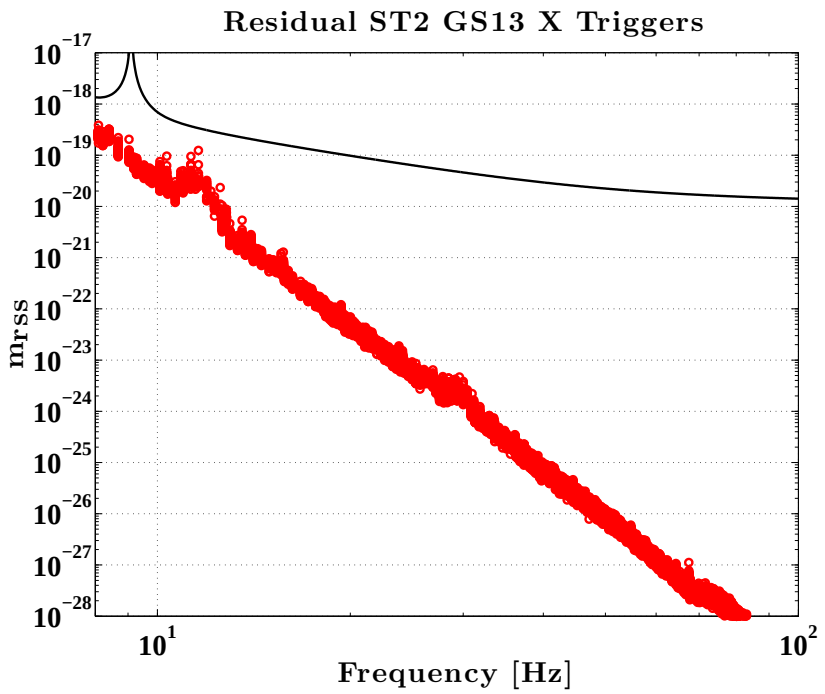

FIGURE 5.14. Propagating the data from Figure 5.13 through the quadruple suspension transfer function and comparing to the full power (125 W injection) sensitivity curve shows that even the loudest event in 10 hours is significantly below the design curve.

Also recall that the IMC splits its actuation at some crossover frequency ($f_x \simeq$15 Hz), forcing the cavity length to match the laser below f_x and the laser to match the cavity length above f_x. The cutoff between these two paths is not infinitely sharp, and if the cavity is sufficiently quiet the frequency noise can accurately be measured by tracking the control signal sent to the mirrors above f_x. The suspicion that the IMC length control at higher frequencies is dominated by frequency noise in the main laser source was confirmed by its high degree of coherence with the PRC length signal at frequencies ranging from 10 Hz up to 100's of Hz (the PRC acts a more sensitive frequency discriminator than the IMC due to its length (56 m vs 16.5 m), and could conceivably be used as an intermediate reference cavity but this is not needed).

By constructing a Wiener filter, using the code developed for feed-forward subtraction in HEPI, the IMC length signal was used as a frequency noise witness

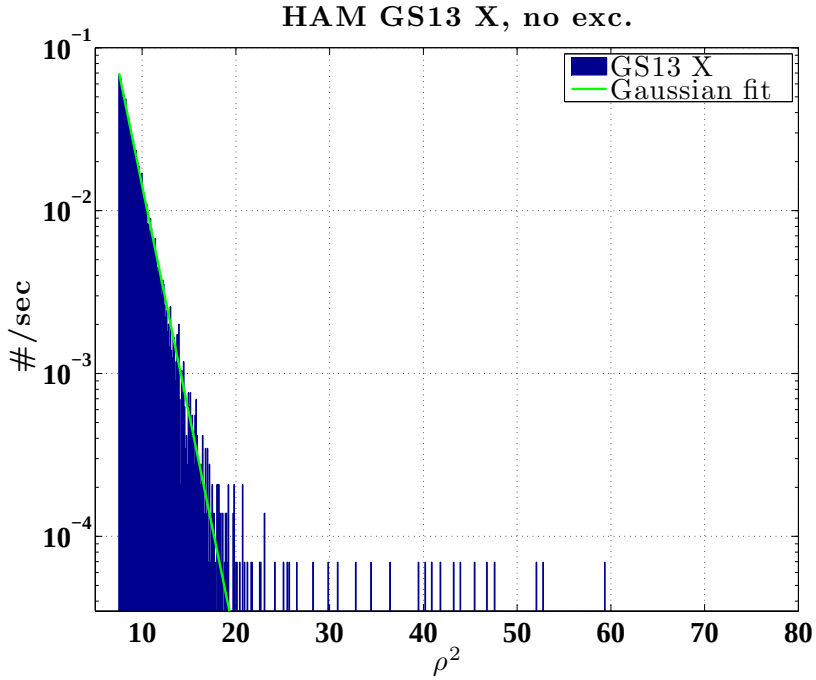

FIGURE 5.15. Result of a search for burst in a HAM ISI's horizontal GS13. The similarity to a similar analysis on the first stage of a BSC ISI is not surprising due to similarities in the controls of the two systems.

and subtracted from the PRC length signal. After cleaning, there was a visible response to the excitation in the 50-100 Hz band, with the excess noise following a $1/f^2$ slope. With evidence of some non-linearity, a dedicated experiment to rule in/out Barkhausen noise was devised. If Barkhausen noise in the actuator's magnet was truly the responsible mechanism then there should be a strong dependence on the applied current's maximum slope, and only the presence of current, not necessarily motion, should be required to induce bursts. There are four actuators on the mirror, laid out in a square to provide length, pitch, and yaw control. The fourth degree of freedom, the constrained or "butterfly" mode, to first order produces no motion of the mirror, despite current flowing through the coils. While symmetry of the applied force cancels the motion at the fundamental drive frequency, any upconverted noise in the actuator response would be uncorrelated and leak through as a displacement, providing a clean test of the actuator without the fear

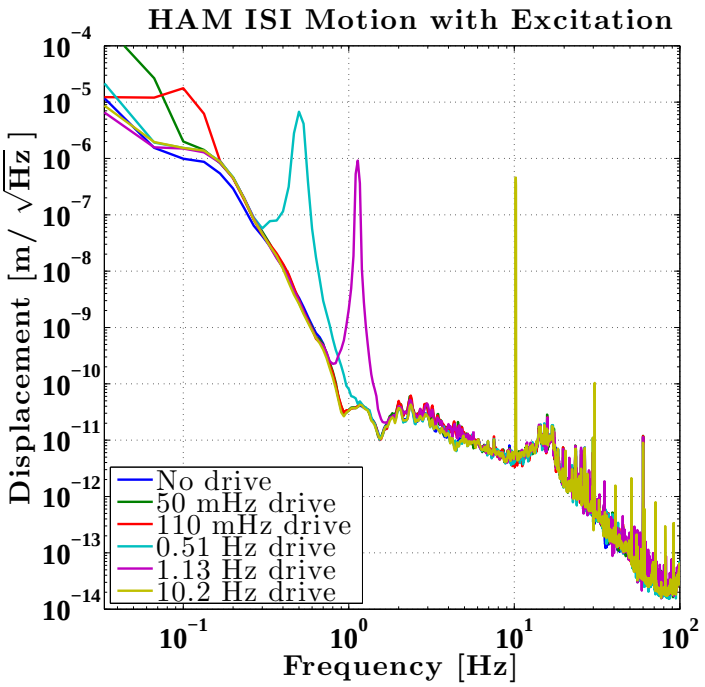

FIGURE 5.16. Spectrum of the in-loop inertial sensor on a HAM ISI as it is being excited at different frequencies in excess of the ambient motion.

that a large signal at the drive frequency might produce non-linearities elsewhere in the system. As such, the drive excitation was formed in the over-constrained DOF, with a frequency of 0.16 Hz to mimic the most consequential ground motion: the microseism. Figure 5.24 contains the spectrum of the PRC motion with and without the excitation, and Figure 5.25 shows the spectrogram for the entire experiment with several on/off transitions included.

While the initial test was performed with a drive amplitude corresponding to 50% of the actuator range, Figure 5.26 shows a similar measurement done at 1/6 and 1/3 of the actuator range as well. Interestingly, there is not much variation in the level of excess noise for different drive amplitudes, indicating perhaps that the non-linearity is some kind of threshold effect in the electronics and not due to Barkhausen noise in the magnets. The drive signal is generated in the real-time software running the detector, and the drive electronics chain includes:

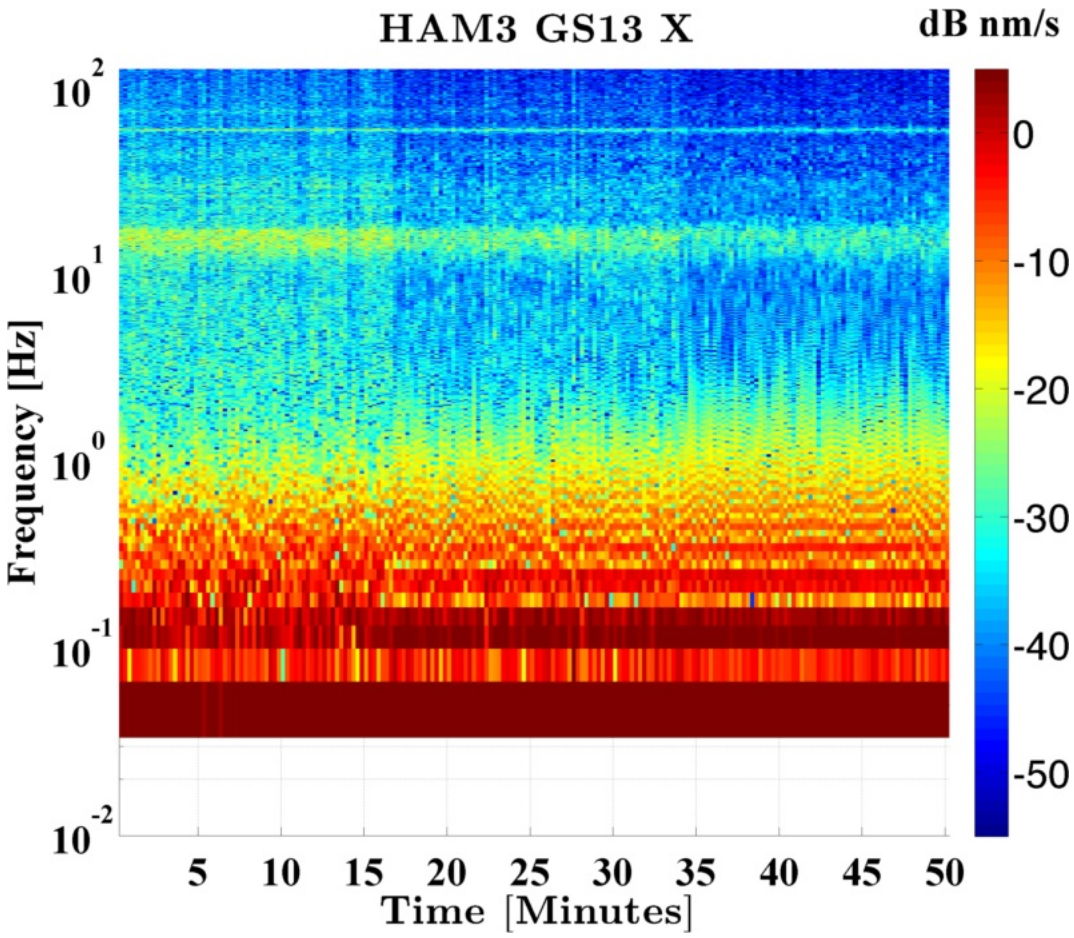

FIGURE 5.17. Spectrogram of HAM horizontal GS13 during excitation test, at microseismic frequencies (0.11 Hz). The amplitude of the excitation is ramped up every ∼15 minutes, although the spectrogram becomes progressively cleaner due to the slowly reducing day-time traffic.

- A digital-to-analog (DAC) conversion card, 18-bit resolution with ±10 V output range, driving differentially.

- An anti-imaging filter, differential received and driven, with at 2^{nd} order Butterworth low-pass filter, corner frequency at 10 kHz.

- A "coil driver", taking the digital signal and then filtering it with a remotely selectable set of low-passes and/or band-stop filters, as well as containing the amplifiers which actually push the coil.

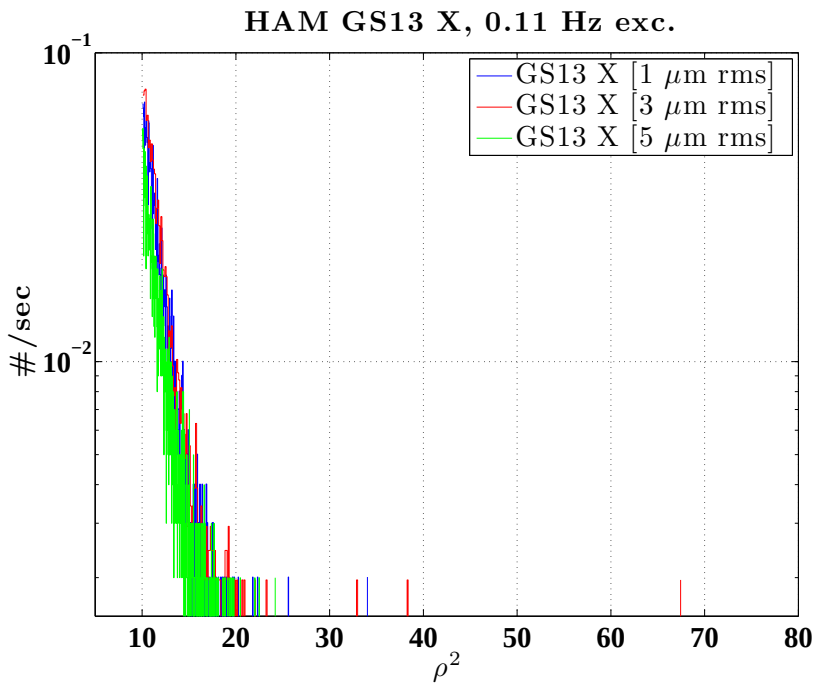

FIGURE 5.18. Result of a search for burst in a HAM ISI's horizontal GS13, in the presence of varying levels of drive at 0.11 Hz.

It should be noted that drive schematics for the suspension actuation may also include a separate field box, the "satellite amplifier", but this is actually used for the local shadow sensor readout, and the actuation connection inside is only a differential pass-through (just wires). The connection is made to concentrate signals onto fewer cables, thus minimizing the number of connectors required at the vacuum chamber's electronics feed-through.

Starting closest to the chamber, an isolated test of the coil driver was made to determine if it was the cause of this non-linearity. A test unit was loaded with a bridge circuit, mimicking the impedance of the in-vacuum coil, and fed into a differential voltage amplifier. The goal of this setup was to provide good common mode rejection at the fundamental drive frequency, such that any noise, which would appear differentially in the two legs of the coil driver, can be detected with

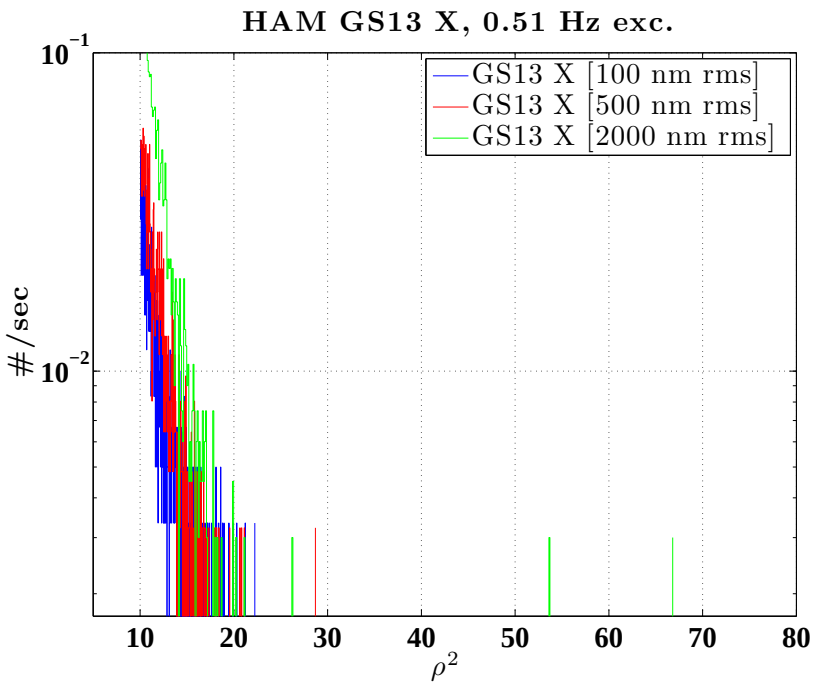

FIGURE 5.19. Result of a search for burst in a HAM ISI's horizontal GS13, in the presence of varying levels of drive at 0.51 Hz.

a sensitive spectrum analyzer, the SRS SR785 [106]. An ultra-low distortion source provided the excitation, the SRS DS360 [106].

The result of this test, for the same drive frequency and similar drive levels as the PRMI test, is shown in Figure 5.27. The V_{rms} labels in the legend do not correspond to the driver output, but rather to an internal voltage monitor, with 3 V_{rms} corresponding to $\sim$1/2 of the driver range. Most of the measurements are limited at the noise level of the analyzer circuit, which corresponds to a displacement well below the PRMI sensitivity, and only a mild increase in voltage noise is produced at the largest drive level. The trace labeled "detector noise" is the noise of the analyzer circuit when driver directly at a similar signal level as the residual coil driver output, that is, after the common mode rejection, to ensure there is no upconversion in any of the electronics readout chain. Figure 5.28 shows the noise

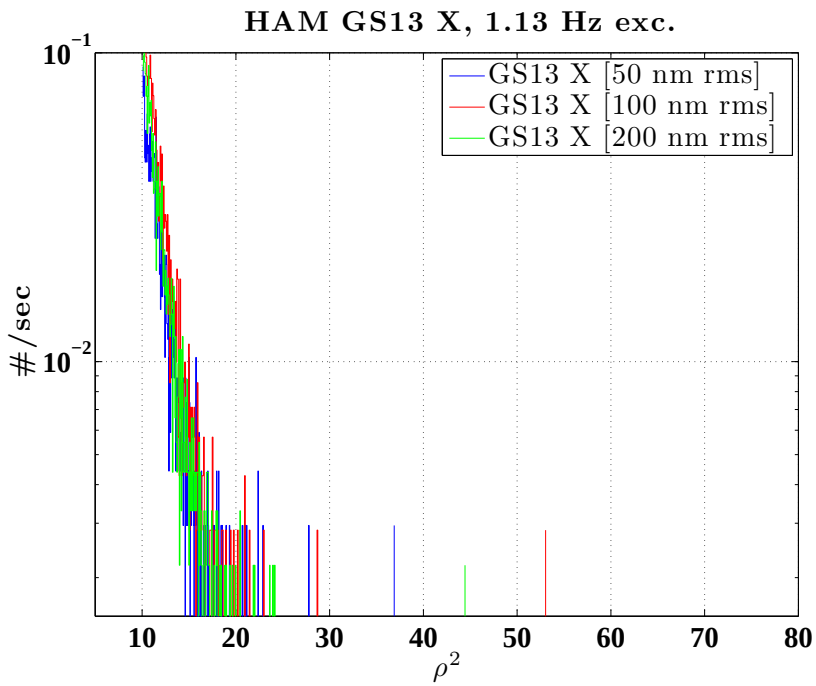

FIGURE 5.20. Result of a search for burst in a HAM ISI's horizontal GS13, in the presence of varying levels of drive at 1.13 Hz.

measurement converted through a modeled suspension chain transfer function into displacement noise, which is well below the measured interferometric signal.

While upconversion from the coil driver was effectively ruled out, an independent study of pulses caused by one of the IMC suspensions revealed a problem with the DAC cards used to control the suspensions [107]. Transients in the DAC card's output voltage occur when the signal crosses certain bits, specifically at zero output (crossing from positive to negative or vice versa) and half-range (65536 counts for an 18-bit DAC) of either polarity. The problem is most likely inherent to the segmented DAC architecture, and solutions are being investigated at the time of writing (this kind of DAC controls all suspensions except for a small number of singly suspended steering optics). The isolation platforms are controlled by 16-bit DACs and do not seem to suffer from this bit flipping transient. For the PRMI upconversion experiment this seems a plausible cause of the increased noise in the

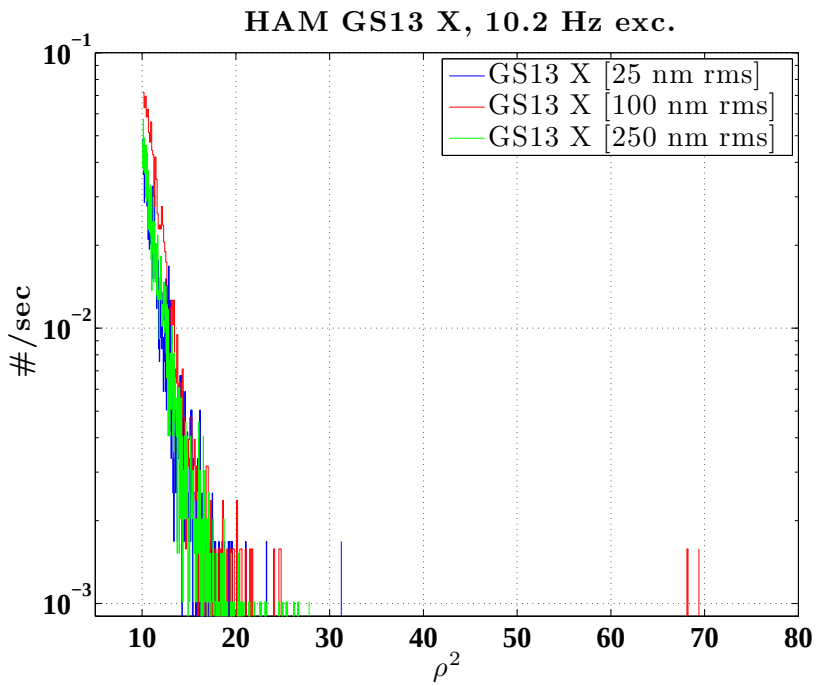

FIGURE 5.21. Result of a search for burst in a HAM ISI's horizontal GS13, in the presence of varying levels of drive at 10.2 Hz.

presence of drive, since the excitation increases the threshold crossings, a test with higher frequency drive could expose this.

Figure 5.29 shows the output of a heavily whitened, AC coupled noise monitor on the drive channel (a digital readback of the DAC output), showing the pulses on zero crossing and half-range crossing. The "UL","LL", etc. labels correspond to the upper left, lower left, etc. actuator positions on the mirror. Figure 5.30 shows the same UL actuator data, zoomed in. The noise monitoring channel is sampled at 2048 Hz, and the rise time of the bit flipping pulse is less than one sample, indicating that the pulse is relatively fast and that its frequency content is probably broad-band. This concurs with the interferometric measure of the upconversion, whose $1/f^2$ slope resembles a broad-band white noise source filtered through the bottom stage of the suspension.

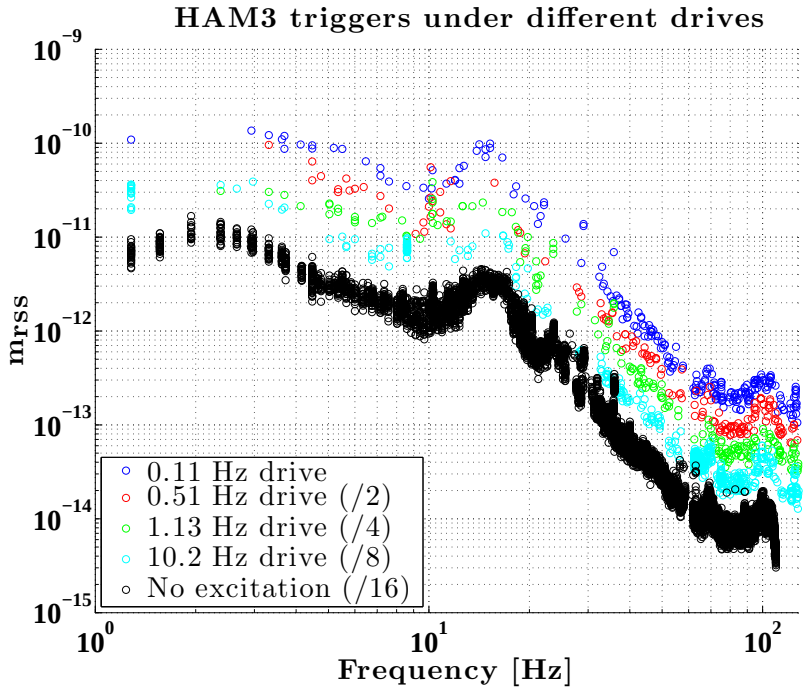

FIGURE 5.22. Calibrated trigger amplitudes for the injection tests, with the largest amplitude drive for each frequency shown. The data sets are scaled as described in the legend to separate them for visibility, their contents are very similar.

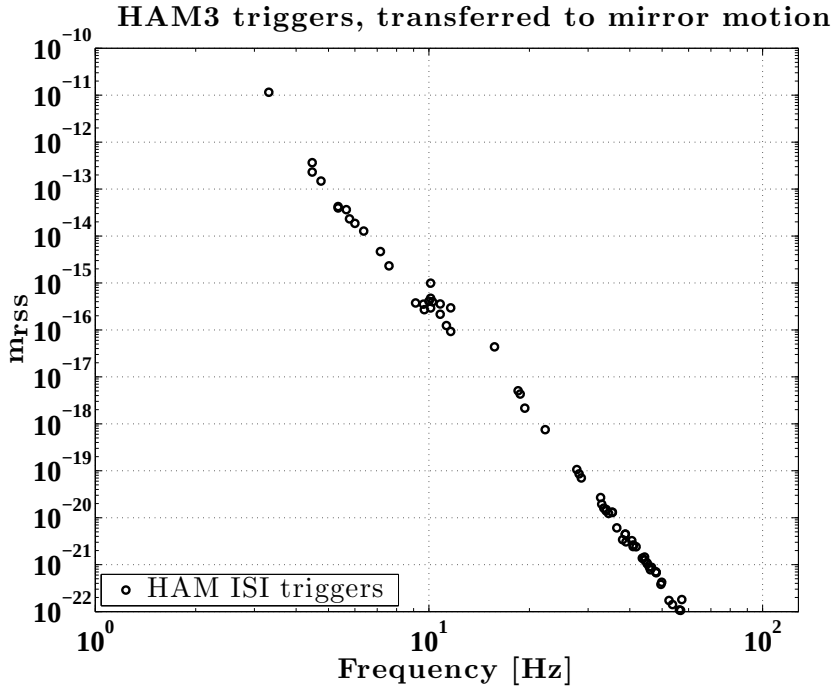

FIGURE 5.23. The 0.51 Hz data set from the previous figure, propagated through the HAM ISI triple suspension transfer function to expected mirror motion. The value of the residual motion expected is so small there is little hope of witnessing such an event in the recycling cavities.

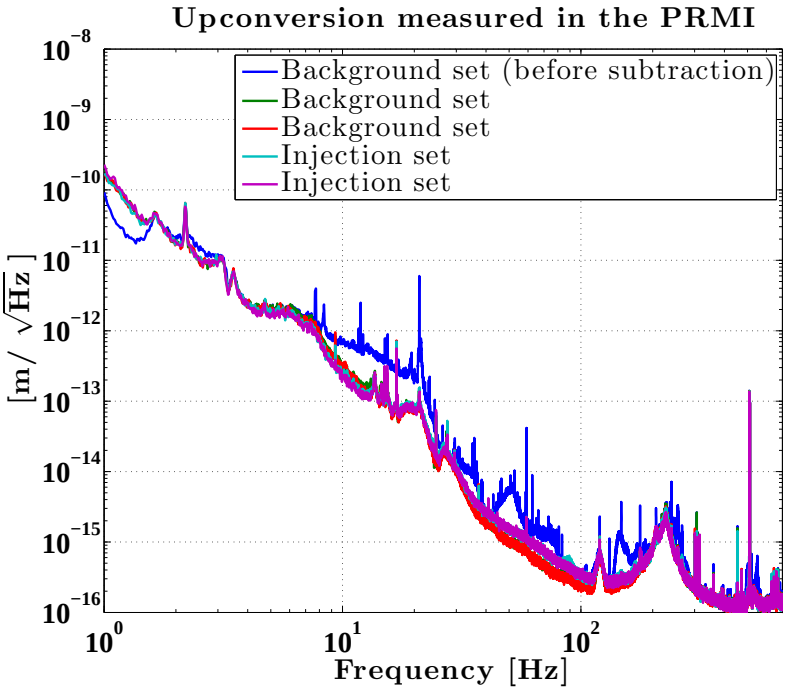

FIGURE 5.24. Spectrum of the PRC length noise with and without a low frequency drive in the over-constrained DOF at the bottom stage (mirror) of one of the triple suspensions. After subtraction of frequency noise measured by the IMC an excess becomes visible between 50 and 100 Hz.

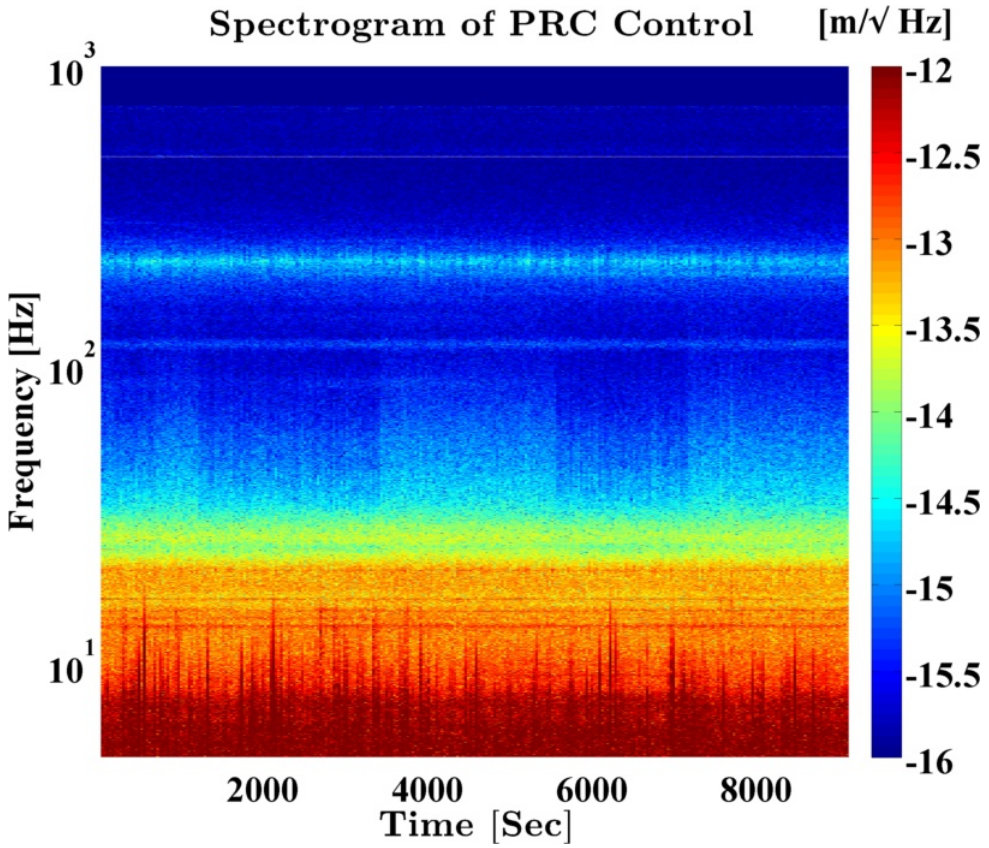

FIGURE 5.25. Spectrogram of the first batch of PRC upconversion measurements, the on/off transition of the drive excitation is clearly visible in the 50-100 Hz band.

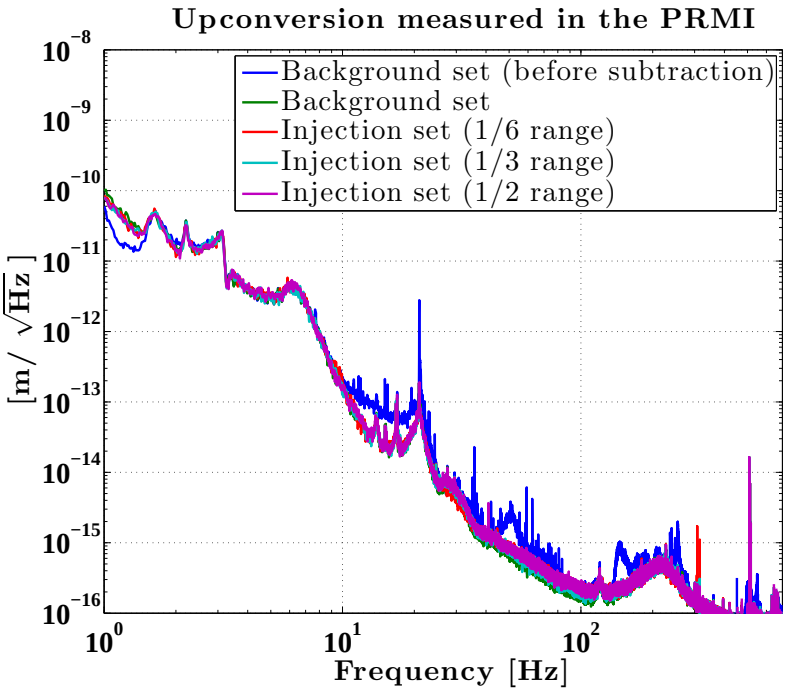

FIGURE 5.26. Repeat of the upconversion test, with different amplitudes of the excitation. Not much variation between amplitudes is observed.

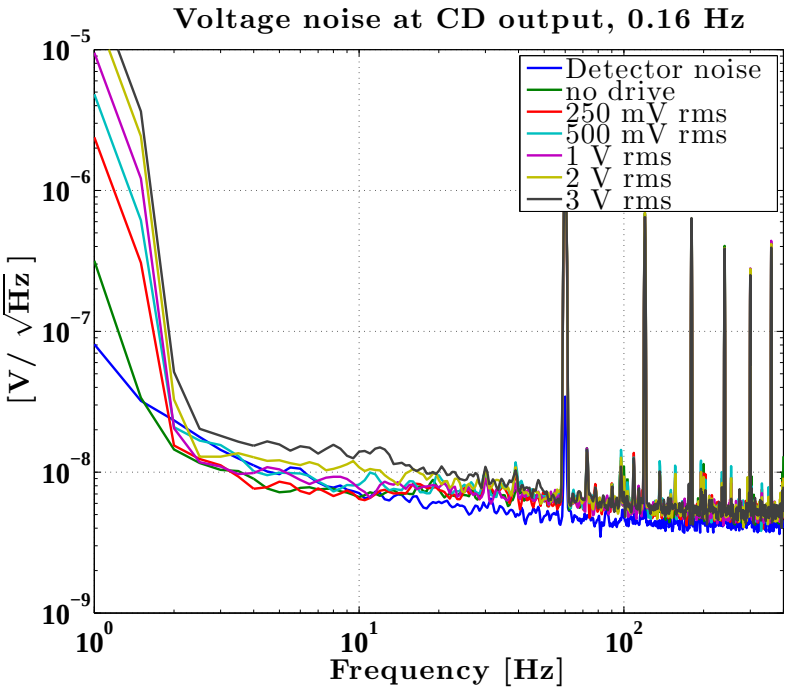

FIGURE 5.27. Dedicated test of upconversion in the suspension coil driver, with a range of drives corresponding to the similar measurement made with the PRMI. Only a small excess is visible at close to maximum drive range, and in general the test is limited by the sensing floor of the analyzer circuit.

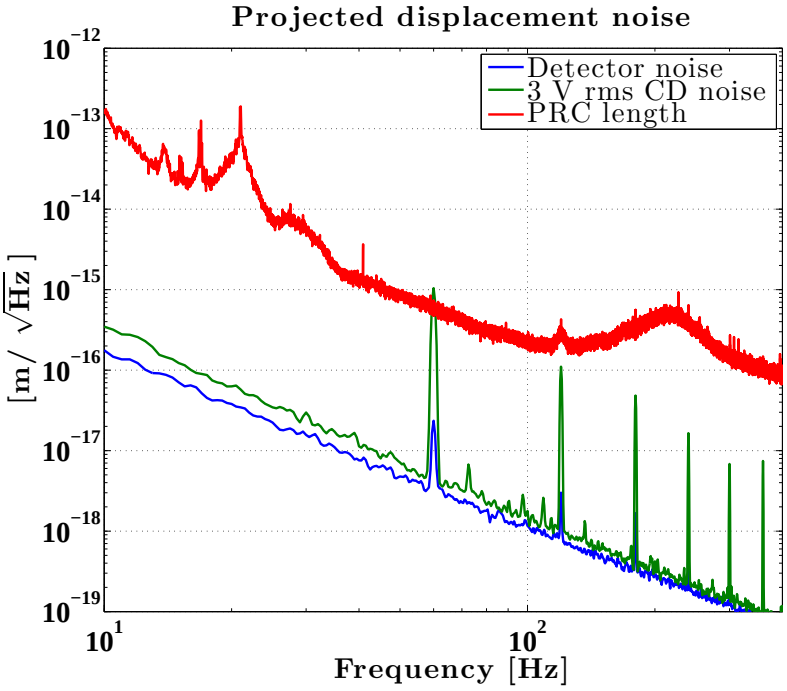

FIGURE 5.28. Converting the voltage noise measured at the output of the coil driver into displacement shows that it is well below the interferometric sensitivity. The 60 Hz harmonics are most likely present in the spectrum analyzer, which is plugged into a standard AC power socket.

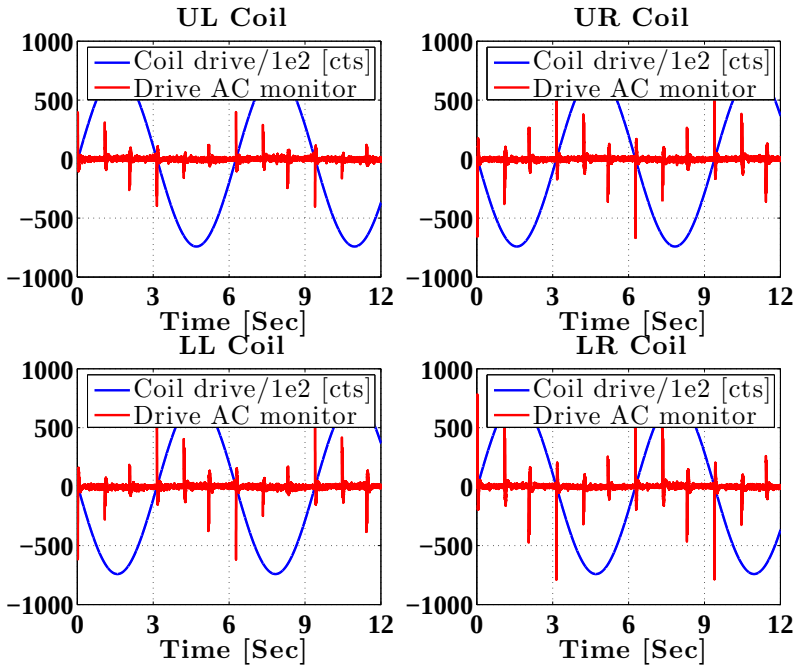

FIGURE 5.29. Monitoring the drive to the suspension with the butterfly excitation used to uncover upconversion. When each channel crosses either 0 or ±65k counts (half-range) a transient appears in the noise monitoring channel with the pulse polarity corresponding to the sign of the crossing. The pulse is one sample or less in duration, with a sample of this channel being ∼0.5 ms.

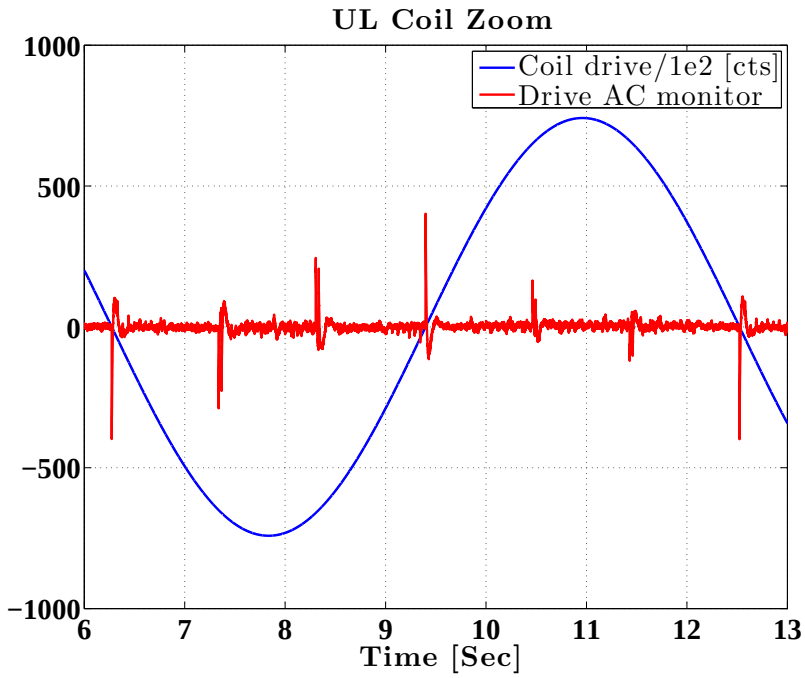

FIGURE 5.30. The same data as in Figure 5.29, zoomed in to show the crossing transients.

6

Piezoelectric Actuators

As mentioned in the introduction, at the dark port of the interferometer there is an small (L ∼0.5 m) suspended filter cavity, the Output Mode Cleaner (OMC). A prototype system was deployed and tested during eLIGO [58, 59], and a similar system was prepared and installed for aLIGO. Both cavities are laid out in a "bow-tie" configuration, a cartoon representation is shown in Figure 6.1, and both had a finesse of $\mathcal{F} \simeq 400$. Although the beam entering the interferometer is relatively pristine, being filtered by the IMC, various imbalances and imperfections in the interferometer conspire to produce some higher-order TEM mode (HOM) content at the dark port. Light which is not in the fundamental mode contributes noise on the photodetectors, but no signal, degrading the gravitational wave SNR. The chief responsibility of the OMC is to strip this "junk" light away, leaving only the TEM_{00} mode in transmission. Also, when a macroscopic offset is placed in the DARM servo to leak some carrier light to the dark port as the local oscillator of the DC readout scheme [58, 108], the OMC removes the RF sidebands as well.

To maintain optical resonance the length of the cavity must be controlled, and in eLIGO this task was performed by two actuators:

- A piezoelectric actuator (piezo for short), providing high bandwidth control (up to ∼100 Hz) but lacking enough range to position the cavity at the fringe

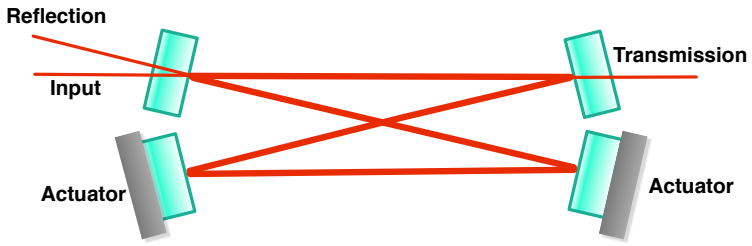

FIGURE 6.1. A schematic cartoon of the OMC's bow-tie cavity. The cavity FSR is ∼300 MHz, and the length is controlled by actuators attached to two of the mirrors. In eLIGO one was a piezo and the other a heater, in aLIGO both are piezos. The transmission of the cavity is split and sensed by two photodiodes, forming the DARM signal after digital processing.

maximum (the maximum piezo stroke was ∼1/3 of a FSR). The piezo was epoxied to a cavity mirror and was annular in shape, allowing for the beam leaking through the mirror to be collected for detection or dumped on a low-scatter surface.

- A heating element attached to an aluminum spacer is glued to another cavity mirror. The speed of this actuator is quite slow comparatively, but given time it can sweep the cavity through numerous fringes.

For aLIGO the decision was made to install two longer-throw piezo elements, to speed up cavity locking by providing bandwidth and range with the same actuator (and a backup). The part chosen is the Noliac NAC2123 [109], a multi-layered ceramic PZT (lead-zirconate-titanate) unit.

While shape, size, and maximum stroke of the piezo are the chief characteristics governing the choice of actuator, for LIGO any displacement noises related to the actuator can also become an important factor. Although the piezo is not technically in the interferometer, its displacement can nevertheless confuse detection by creating power fluctuations in the transmitted beam of the OMC, which is converted to the gravitational wave signal. The motion of the piezo couples to the transmitted power by the relation

$$P_{\text{trans}} = \frac{P_{\text{incident}}}{1 + \left[\frac{2\mathcal{F}}{\pi}\right]^2 \sin^2(kx)}, \tag{6.1}$$

where $\mathcal{F}$ is the finesse, k is the wave number, $k = 2\pi/\lambda$, and x is the motion of the mirror. For this analysis, the OMC has been approximated as a two mirror Fabry-Perot cavity with $r_1 = r_2$, which is a good approximation of the real OMC (the input and output coupler have transmission of ∼8000 ppm, the other two mirrors are high reflectors). Differentiating P_{trans} with respect to the mirror motion, and then dividing by P_{trans} we find that the RIN in transmission depends on the mirror motion as

$$\frac{\mathrm{d}P_{\text{trans}}}{\mathrm{d}x}\frac{1}{P_{\text{trans}}} = \frac{\mathrm{d}RIN_{\text{trans}}}{\mathrm{d}x} = \frac{-\left[\frac{2\mathcal{F}}{\pi}\right]^2 k \sin(2kx)}{1 + \left[\frac{2\mathcal{F}}{\pi}\right]^2 \sin^2(kx)}. \tag{6.2}$$

When the cavity is positioned at fringe maximum, the motion around the fringe will couple quadratically to the transmitted power fluctuation. When there is some residual offset, x_0, perhaps due to the limitations of the length servo,a linear coupling appears and dominates, such that

$$RIN(f) = \left[\frac{4\mathcal{F}}{\lambda}\right]^2 2\delta x(f) \cdot x_0, \tag{6.3}$$

where $\delta x(f)$ is the spectrum of fluctuations in the mirror position. The goal displacement noise for the piezoelectric actuator is easy enough to set: the displacement noise is acceptably low when it does not significantly compete (a factor of several to ∼10x below) with the RIN in transmission due to the shot noise of the detected current, i_{DC}, such that

$$\left[\frac{4\mathcal{F}}{\lambda}\right]^2 2\delta x(f) \cdot x_0 < \frac{1}{\rho}\sqrt{\frac{2e}{i_{\text{DC}}}}, \tag{6.4}$$

where e is the fundamental charge, and ρ is the safety factor. For aLIGO the intended detection current is ∼100 mA, at maximum input power, corresponding to a RIN of ∼1.8x10^{-9} $1/\sqrt{\text{Hz}}$. Assuming the length servo can maintain the fringe maximum to ∼0.5 pm (this was the estimated offset in eLIGO), this places the limit on δx of, with a ρ of 10, at $\sim 10^{-16}$ m$/\sqrt{\text{Hz}}$, at all frequencies where the detector expects to be shot noise limited.

As far as the author knows, such a tight limit has not been placed on the displacement noise of piezo ceramic actuators, at least at audio band frequencies, and so as a matter of interest and of technical noise risk mitigation an experiment was designed to either measure such a displacement noise or establish a suitable upper limit. Studies of piezo noise have been performed as part of the design of commercial accelerometers [110], which often use piezos as the force (acceleration) to voltage transducer. Assuming thermal noise as the fundamental displacement limit, an estimate can be made following the analysis of a material whose loss stems from internal damping [39]. Here, we posit that the piezo, as an oscillator, obeys a modified Hooke's law, where the stiffness acquires an imaginary term to characterize the loss,

$$F = -k\left[1 + i\varphi(\omega)\right]x, \tag{6.5}$$

where F is the restoring force, k is the piezo stiffness, x is the piezo displacement from its nominal size, and $\varphi(\omega)$ is the "loss angle", a material property of the piezo ceramic. Determination of the value of $\varphi(\omega)$ comes from its relationship to the material's Q,

$$Q = \frac{1}{\varphi(\omega_0)}, \tag{6.6}$$

where ω_0 is the piezo's mechanical resonance. The frequency dependence of the loss angle for the piezo is not known, and is assumed (perhaps mistakenly so), to be frequency independent, that is $\varphi(\omega) = \varphi(\omega_0) = 1/Q$, and it will be written simply as φ.

Combining the loss angle, mass, and stiffness of the piezo, the spectrum of the thermally driven motion is given by

$$x(\omega) = \sqrt{\frac{4k_B T\omega_0^2\varphi}{m\omega\left[(\omega_0^2-\omega^2)^2+\omega_0^4\varphi^2\right]}}. \tag{6.7}$$

For the piezo's in question, the mass is $m \simeq$1.5 g, the stiffness is $k \simeq$ 4x10^8 N/m, the mechanical resonance is at $\omega_0 \simeq 2\pi \cdot 80$ kHz, and the quality factor is $Q \simeq 50$. With these parameters, the thermal noise of the piezo at 100 Hz is expected to be roughly 4x10^{-17} m/$\sqrt{\text{Hz}}$, with a $1/\sqrt{f}$ slope below the resonance, where all frequencies of interest lie. Figure 6.2 shows the computation of Equation 6.7 from 1 Hz to 1 MHz. This places the thermal noise below the desired measurement sensitivity and, consequently, indicates that it is not an issue even when operating at maximum design current.

6.1 Characterization Experiments

Along with the piezo displacement noise it is also important to characterize the amount of angular deviation created by length drive, since a mirror will be attached to it and the beam in reflection could become misaligned. Also worth measuring is the piezo hysteresis, although this is not of crucial significance since during operation the piezo will not be driven through a significant fraction of its range. For displacement noise, a small Michelson interferometer was designed and built. For hysteresis and angular deflection a combined Michelson interferometer and optical lever was built, using a shorter wavelength source than the displacement

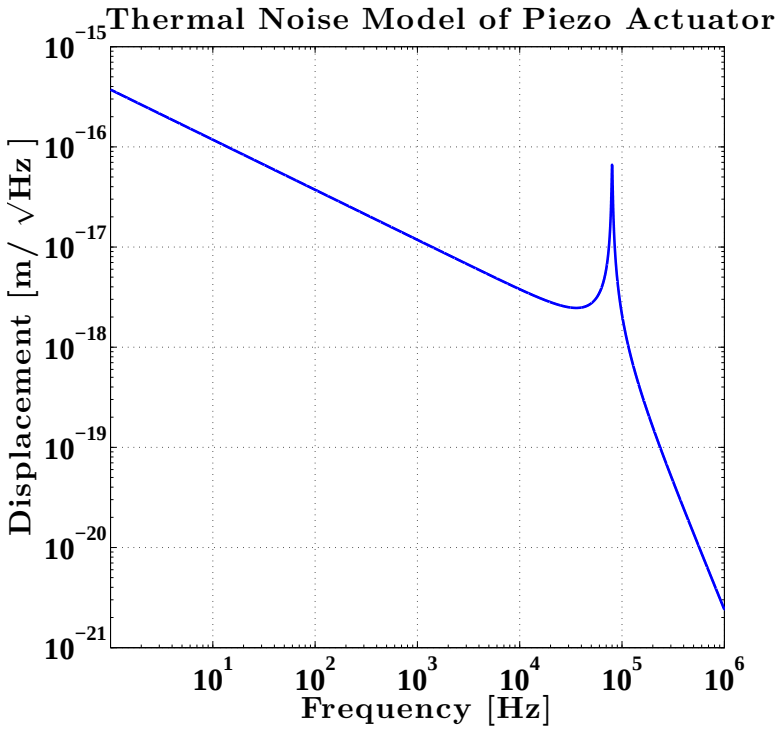

FIGURE 6.2. Thermal noise estimate, following Saulson [3, 39], for a piezo actuator with the parameters of those used in the aLIGO OMC. The transmitted RIN limit on the displacement noise of 10^{-16} m/$\sqrt{\text{Hz}}$ is exceeded only at frequencies below the band of interest, and the mechanical resonance of the piezo exists above this band.

noise Michelson, to facilitate more fringe crossings when sweeping the piezo from rail to rail. Also, a simple electrical circuit was assembled to characterize the mode of actuation of the piezo once attachment of the mirror and mounting plate is complete.

6.1.1 Hysteresis and Angular Deflection

Non-linearity in the actuation was measured by actuating one mirror of a Michelson interferometer, illuminated by a HeNe laser, with the piezo. Analogous to ferromagnetism, the piezo is a ferroelectric material so some amount of hysteresis is expected. At the same time, an auxiliary beam is reflected off the piezo mirror at an angle and sensed on a quadrant photodiode (QPD) to establish the amount of

angular motion caused by the length actuation. The hysteresis is clearly visible in Figure 6.3, note the asymmetry in the Michelson dark port signal. The dark port power usually depends on piezo drive via the relation $P_{\mathrm{AS}} = P_{\mathrm{BS}}\sin(k\alpha V)$, where α is the actuation coefficient and V the applied voltage. To quantify the hysteresis, the dark port power is instead fit with a non-linear expansion of the drive voltage. Including the βV^2 and γV^3 terms is enough to produce a good fit, and as much as a 30% deviation from linearity is observed. The linear coefficient, α, for the several dozen units tested averages $\sim$14 nm/V. In practice, once the piezo positions the OMC at fringe maximum, only a small percentage of its range is required for the length servo, and this much hysteresis is most likely not an issue.

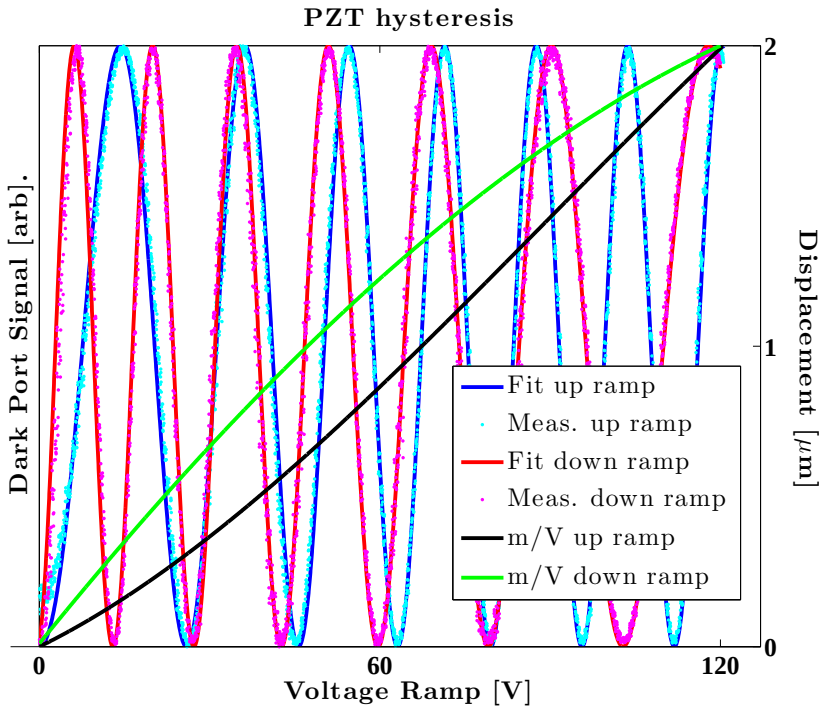

FIGURE 6.3. Measurement of piezo non-linearity due to hysteresis. Instead of tracing out a linear relationship between drive voltage applied to the piezo and displacement of the mirror, a curved path with significant quadratic and cubic terms is more realistic.

Angular deflection of the mirror attached to the piezo occurs due to some asymmetry in the expansion and contraction of the actuator when a voltage is applied. Of the roughly two dozen units tested there was a significant variation in their performance in this regard, and units were selected for inclusion in the production OMCs on this basis. An example test output is shown in Figure 6.4. A good unit produces ∼6 µrad per µm of actuation, a bad one ∼5x this amount. The waist size of the OMC is $w_0 \simeq 0.5$ mm, corresponding to a cavity divergence angle of $\theta_{OMC} = \lambda/\pi w \simeq 0.7$ mrad. As such, a unit with large length to angle coupling, if swept from nominal alignment by a displacement on the order of a fringe size, would begin to misalign the cavity several per cent of the divergence, perhaps not a large effect but best to be avoided due to various noise couplings such a misalignment permits.

6.1.2 Mode of Actuation

Ideally the mode of piezo actuation only creates a displacement perpendicular to its surface, and therefore the attached mirror, referred to by the manufacturer as the "thickness" mode. Fortunately, the material's piezoelectricity allows for the mechanical response to be tested electrically, with a simple capacitive bridge circuit, a schematic of which is shown in Figure 6.5. Ideally, the un-loaded response of the piezo is a combination of a simple capacitive impedance, $Z_{\mathrm{C}} = 1/i\omega C$, and a series-parallel resonance from the oscillator, and this is what is observed.

Measurement of $H = V_{\mathrm{Out}}/V_{\mathrm{In}}$ can be converted to the piezo impedance by the relation

$$Z_{\mathrm{PZT}}(\omega) = Z_{\mathrm{C}}(\omega)\frac{H(\omega)}{1 - H(\omega)}, \tag{6.8}$$

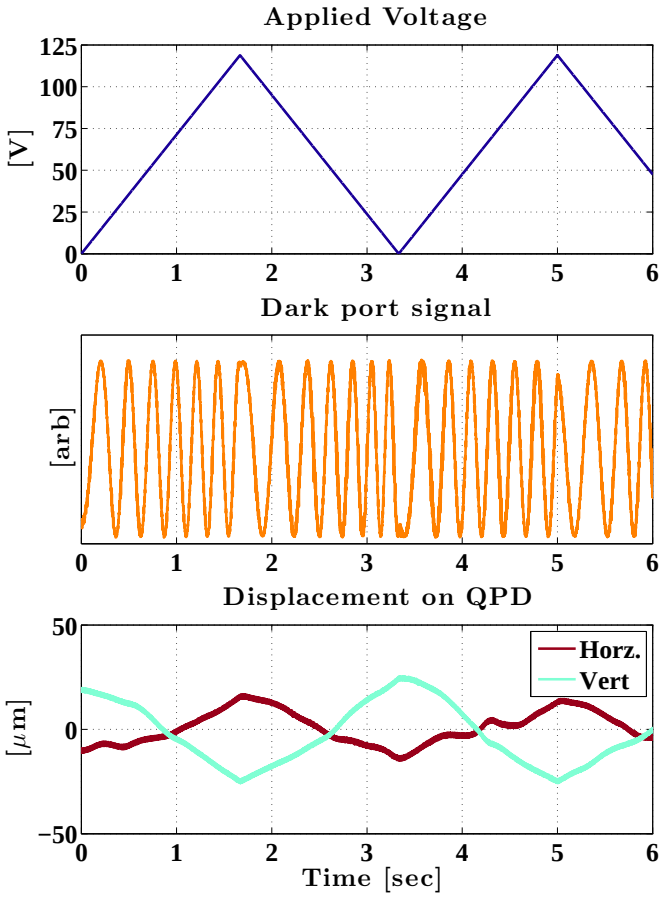

FIGURE 6.4. Angular deviation of a beam reflected off of the piezo mirror as the actuator sweeps from minimum to maximum voltage. The change in position of the beam on the quad photodiode is converted to mirror angle via the 1 m lever arm.

where $Z_{\mathrm{C}}(\omega)$ is the impedance of the reference capacitor. Figure 6.6 shows several measurements of $Z_{\mathrm{PZT}}(\omega)$, each in a different mechanical configuration. As mentioned, the free piezo (dark green trace) is along the line of what is expected, that is, it resembles greatly the plain capacitor of similar capacitance (light green trace) with the addition of a series-parallel resonance around 80 kHz, presumably in the thickness mode. A mirror is then attached to one side of the actuator, and the other side is attached to a metal support (in the production OMC the piezo is attached to a mirror and a fused silica "tombstone" block which juts out from

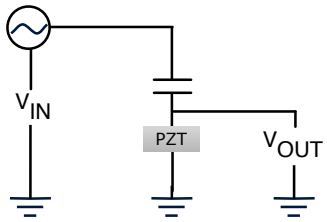

FIGURE 6.5. A simple capacitive bridge circuit used to invert the electro-mechanical transfer function of the piezo actuator in different loading configurations. By comparing these transfer functions, it can be seen if the mode of actuation is disturbed.

the fused silica OMC breadboard). The important feature in Figure 6.6 is the difference between the black and red traces, which correspond to adhesion with cement (black) or epoxy (red). The relatively soft epoxy produces a transfer function which is almost unchanged qualitatively from the free piezo, with the mechanical resonance shifted upward in frequency by the increased mass load. The relatively hard cement, however, introduces number features from 60 kHz to 100 kHz, which indicate pollution of the mechanical mode of actuation. Epoxy was used in the production OMC fabrication, with a layer of $\sim$100 µm diameter silicon microspheres mixed into the adhesive to create a uniform bond spacing (the alignment of the cavity mirrors is performed while the adhesive is still uncured, and is intended to be permanent afterwards).

6.1.3 Displacement Noise

A schematic of the Michelson interferometer used to measure the piezo displacement noise is shown in Figure 6.7. The interferometer was read out and controlled with an aLIGO style digital input/output system and custom real-time code, clocked at 16384 Hz. Each arm of the interferometer is folded, to double the coupling of actuator noise to the phase change in the arm. While one folded mirror is always attached to a piezo, the other is connected either to a heater and aluminum spacer or another piezo depending on various test plans. The fold mir-

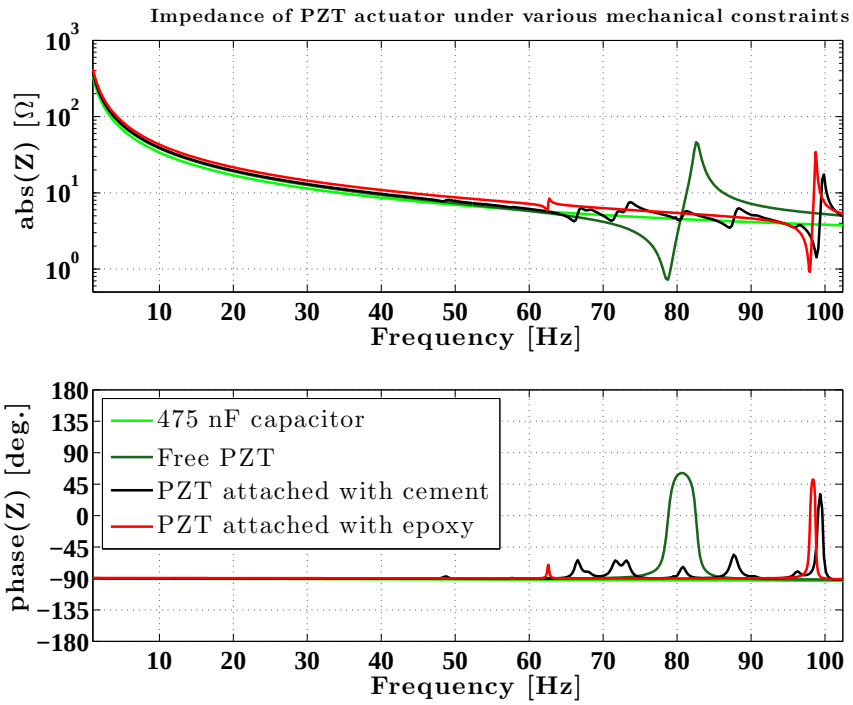

FIGURE 6.6. Effects of mechanical configuration on the impedance of the piezo. A plain capacitor of similar capacitance is plotted for reference.

rors, end mirrors, beamsplitter, and dark port photodiode are all housed inside a vacuum chamber and are supported by a double isolation stack made of two 3/8" thick stainless steel plates, with 4 RTV silicone rubber corks in between each stage. The stack provided passive isolation about ∼15 Hz.

The chamber was housed on an optical table, where the rest of the optical setup was positioned. The laser source is a LightWave 126 NPRO [118] (non-planar ring oscillator) capable of outputting 250 mW of $\lambda = 1.064$ µm light, and run for this experiment at slightly less power, ∼225 mW. The beam propagates through an acousto-optic modulator (AOM) before being routed into the interferometer, with a small % of the light diffracted out of the main path and onto a black glass beam block. A small part of the laser is picked off downstream, directed to a photodiode, and this signal is then fed back to the AOM as a power stabilization servo. Figure 6.8 shows the loop shape of the intensity servo, which was able to

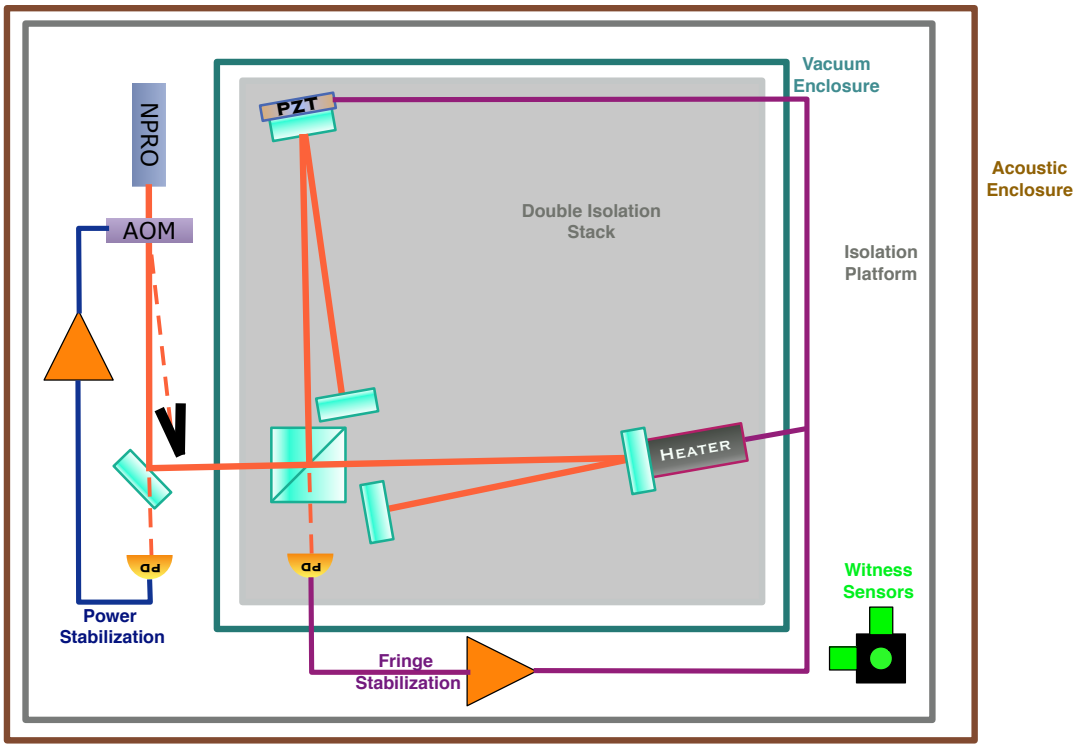

FIGURE 6.7. Layout of the small Michelson used to measure piezo displacement noise. Not included is the digital data acquisition system (DAQ), which also providing analog outputs for servo control of the Michelson fringe. The power stabilization servo bandwidth was beyond the speed capabilities of the DAQ, so the servo was completely analog. Also not shown is a microphone, used as witness in conjunction with the X,Y,Z accelerometers.

suppress the power fluctuations almost to the shot noise level of the detected photocurrent, see Figure 6.9.

Also on the optics table are 3 uniaxial accelerometers, aligned to the "X,Y,Z" directions of the setup, and a microphone. These auxiliary sensors served as witnesses, and any signals coherent with the Michelson output were filtered in post-processing, again using the optimal Wiener filtering code developed for HEPI, mentioned in Chapter 3. The whole table is isolated by floating it on a layer of pressurized air, suppressing ground motions above 1 Hz but enhancing the coupling to acoustic noises, so the whole setup was built inside an acoustic enclosure made of stiff panels combined with absorptive foam padding.

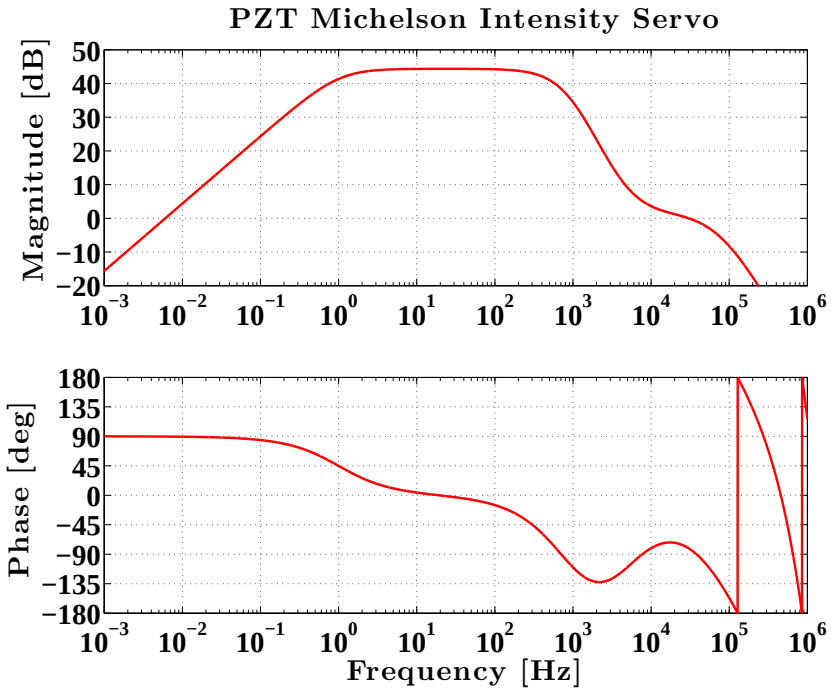

FIGURE 6.8. Open loop gain of the intensity servo used to stabilize the laser illuminated the piezo Michelson. The sensing photodiode is biased and loaded with a resistor to readout the photocurrent. This signal is then filtered with passive elements buffered by SRS SR560 voltage amplifiers before being fed to the RF amplifier which drives the AOM. A 30 kHz servo was sufficient to suppress the noise in the band of interest to just above the shot noise level of the detection photocurrent.

In order to minimize the coupling of power fluctuations to the dark port the Michelson is operated close to the dark fringe, typically 1 mW out of the 160 mW which make it to the beamsplitter. There is some finite contrast defect which limits how low the dark port power can be, in this setup it was reliably 10^{-3}, via manual alignment. A 3 mm, high quantum efficiency ($\eta > 0.9$) InGaAs photodiode was used for the dark port detection. Capable of producing several mA of current in photovoltaic mode, the photodiode was operated without external bias and a low-noise front-end readout circuit for the photodiode was designed with this in mind. The low operating current also allows for a high transimpedance resistor, without stressing the DC levels of the sensing circuit, a schematic of which is shown in Figure 6.10, and the expected dark noise compared to shot noise is shown in

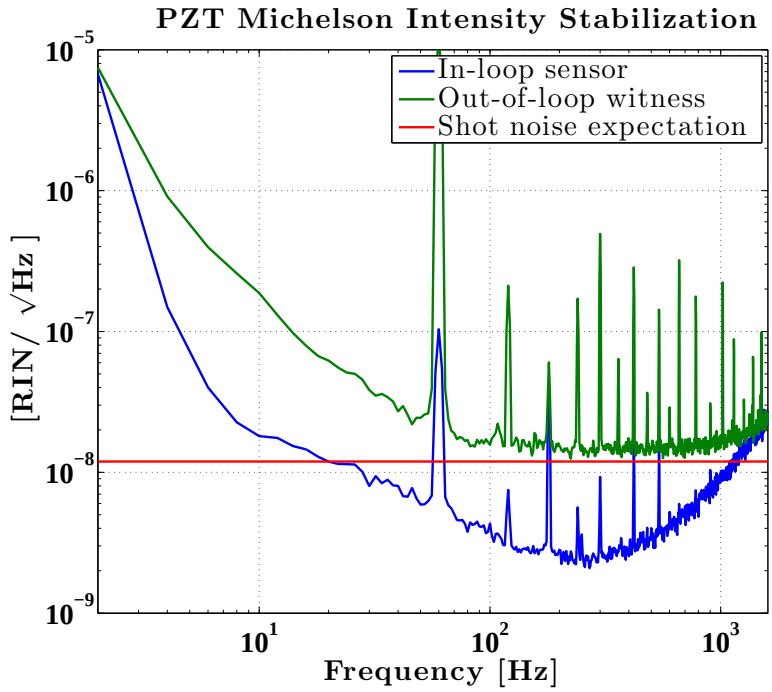

FIGURE 6.9. Spectra of the in-loop sensor and an out-of-loop witness photodiode showing the residual intensity noise when the servo is enabled. The servo is sensing limited, which is why the in-loop sensor appears to be so far below the shot noise level. The free running RIN of the source is typically 5x10^{-7} to 10^{-6} $1/\sqrt{\text{Hz}}$.

Figure 6.11. The circuit noise budget was created using the LISO software package [111].

Frequency noise coupling is controlled by carefully tuning the Michelson arm lengths to be the same. Taking free running frequency noise of an NPRO to be 100 Hz/$\sqrt{\text{Hz}}$ at 100 Hz, with a $1/f$ slope, the required arm mismatch is approximately

$$\Delta L = \frac{3\text{x}10^{14}\text{Hz} \cdot 10^{-16}\text{m}/\sqrt{\text{Hz}}}{100\text{Hz}/\sqrt{\text{Hz}}} \tag{6.9}$$

or about 300 µm, at the edge of what careful positioning by eye will accomplish. Fine tuning is achieved by modulating the laser frequency directly while monitoring the Michelson output at the same frequency, and adjusting the mirror positions to minimize this effect.

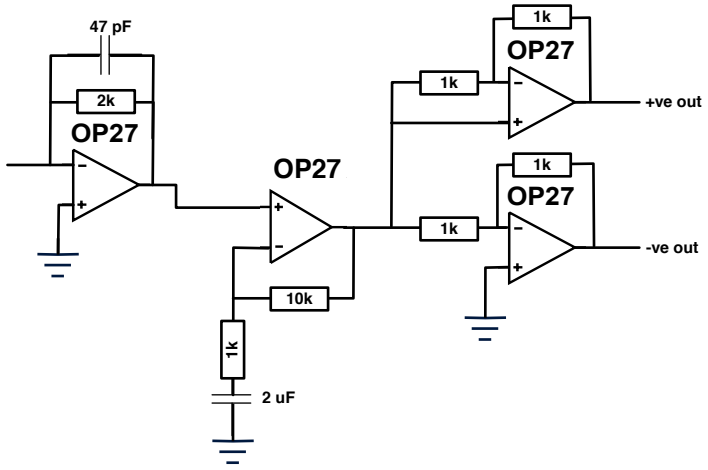

FIGURE 6.10. Schematic of the simple photodiode readout circuit used for the piezo Michelson. After the transimpedance front-end there is one whitening stage to condition the output spectrum for improved SNR during digitization. This is followed by single to differential conversion, as all following electronics (anti-aliasing filter and ADC) are differential devices.

The electronics which drive the piezo can also contribute significant noise, due to the high voltage necessary for operation. The drive electronics had a flat noise floor of several $\mu V/\sqrt{Hz}$ which, with an actuation coefficient of 14 nm/V, would dash any hopes of achieving the goal sensitivity. A large series resistance in the drive line, coupled to ground through the piezo capacitance, places a low frequency ($f_p \sim 1$ Hz) pole in the electronics noise path and filters out the driver. This also restricts the bandwidth of the locking servo, but the input disturbance is both small and mostly common mode on the steel bread-board, requiring very little control authority.

Scattering can contribute significant noise as well, and a serious effort was made to both minimize the existence of stray beams, and to direct the unavoidable stray light onto low scatter, black glass beam dumps. Scattering events can also occur in the presence of gas molecules [112, 113]. The phase noise contributed by these interactions, depends on the molecular species, the absolute pressure, and

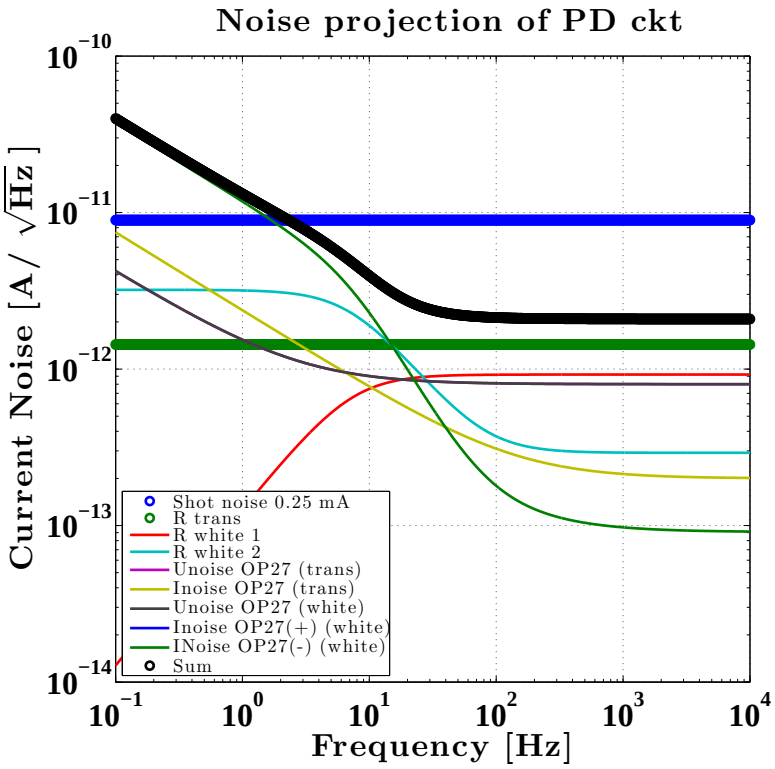

FIGURE 6.11. Noise budget for the photodiode readout circuit used in the piezo Michelson. Shot noise at low photocurrents should be detectable in the band of interest. Noise budget made using the LISO software package.

the optical interaction space (beam-size profile). In a single arm, a gas species with pressure ρ and polarizability α will produce an apparent displacement noise of

$$\delta x(f)_{\text{gas}} = 4\pi\alpha\sqrt{\frac{\rho}{v_0}}\sqrt{\int_0^L \frac{e^{-2\pi f w(z)/v_0}}{w(z)}dz}, \tag{6.10}$$

where v_0 is the thermal velocity of the molecules and $w(z)$ is the Gaussian beam profile (the beam is propagating in the z direction). The integration limit of L corresponds to the total optical path length, which for the simple Michelson is simply twice the arm length, but for a resonant interferometer will depend on the number of bounces (i.e. the storage time). Combining this noise from both arms will result in an apparent displacement of the Michelson of $\sqrt{2}\delta x(f)_{\text{gas}}$. The frequency shape of this noise is white up until a cutoff frequency set by the beam size and

molecular velocity, which is on the order of 1 kHz for aLIGO (the noise is constant over the band of interest), and low enough for this experiment that the noise is attenuated slightly in the measurement band. While for LIGO sensitivities the residual vacuum pressure must be kept very low (10^{-9} Torr), this small Michelson can operate at atmosphere, and this was the default operation due to acoustic injection from the vacuum pumps attached to the chamber. Brief measurements were made at 10^{-3} Torr (a 6 order of magnitude pressure differential) to verify that the broad-band minimum in the spectrum remained unchanged.

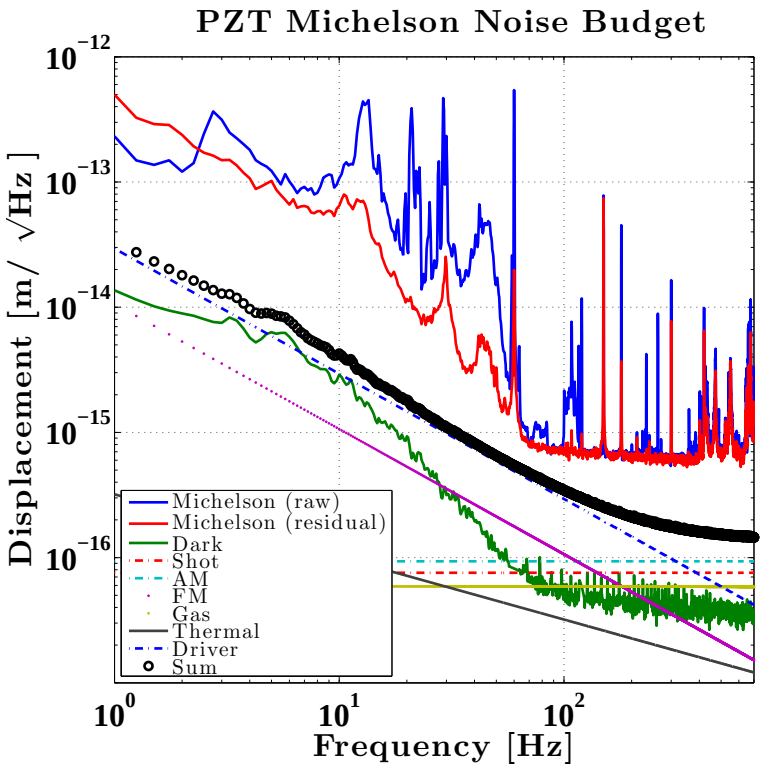

FIGURE 6.12. Noise budget for the piezo Michelson. Raw and residual refer to the Michelson displacement before and after witness sensor subtraction, respectively. The AM and FM traces are laser intensity and frequency noise couplings, respectively. The measured dark noise corner frequency is higher than that expected by the modeled circuit, but the comparison of broad-band high frequency dark noise to shot noise is reasonably close to the expectation.

Figure 6.12 combines the noise sources described above into a budget for the measurement. The "raw" trace is the calibrated Michelson displacement, and the "residual" trace is after the witness accelerometer and microphone subtraction has been performed. The broad-band noise floor is around 6-8x10^{-16} m/$\sqrt{\text{Hz}}$, with a slight slope. This noise is not quite as low as was hoped, and this consumes the most of the safety factor when compared to the 100 mA shot noise, if the length noise is unsuppressed. It is also clearly in excess of the budgeted noise, and corresponds either to the piezo noise (well above its thermal noise model) or, more likely some sensing noise in the setup. The leading noise source is the piezo driver noise, however this is very well measured and its coupling straightforward, hence the budget must be incomplete.

6.1.4 OMC Length Control

The length of the cavity is controlled with a dither scheme, modulating the piezo at several kHz and demodulating the transmitted RIN to form a length error signal. The bandwidth of this loop extends up to ∼100 Hz, and length noise from the piezo will be suppressed in this band. Taking the broad-band noise floor measured in Figure 6.12 to be the piezo noise and estimating a reasonable OMC length loop gain the suppressed piezo noise in terms of transmitted RIN is shown in Figure 6.13. For most of the detector's shot noise limited band the piezo noise will not be effectively suppressed, and increasing the OMC length loop to a suitable bandwidth from the piezo noise viewpoint is problematic.

6.1.5 Upconversion

Bursts from the piezo can also be a problem, potentially from the Barkhausen mechanism discussed in Chapter 5 (the piezo is made of ferroelectric domains)

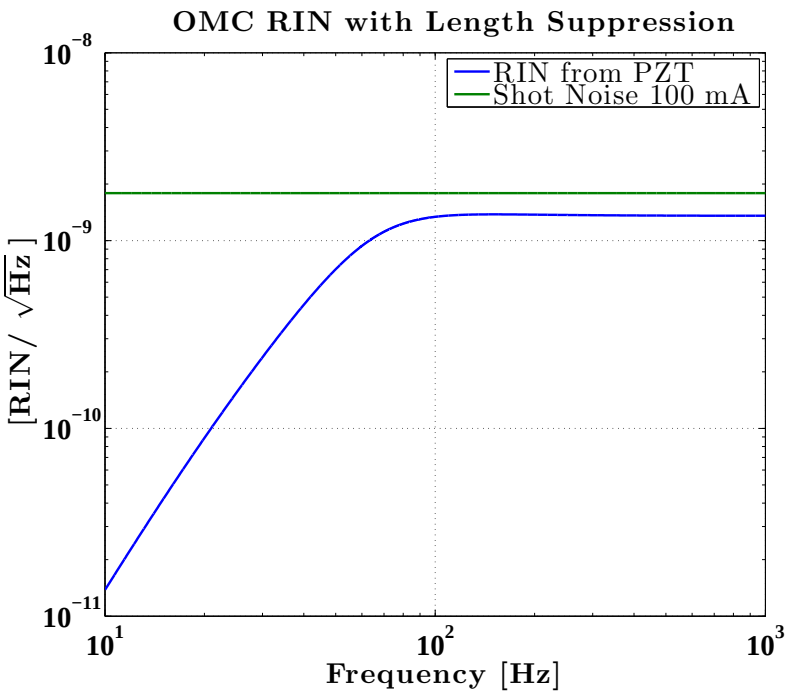

FIGURE 6.13. PZT noise projection with suppression from a 100 Hz UGF length servo. At frequencies where the piezo coupling is reduced, shot noise is not the only limiting source for the detector. In the shot noise dominated region, the noise does not exceed the maximum power shot noise, but would raise the noise floor of the instrument by ∼25 %.

and therefore presumably dependent on the slope of the drive voltage. When the voltage drive consists only of the control signal used to maintain the Michelson fringe offset the spectrum of the dark port signal is quite stationary and a burst search reveals a distribution of triggers resembling Gaussian noise, see Figure 6.14. As a test, with a piezo actuator attached to the mirrors in both interferometer arms a common mode drive voltage is applied, at 1 Hz, on top of the control signal. While the actuators are from the same batch, their actuation coefficients were sufficiently mismatched that there was significant leakage into the Michelson degree of freedom. To suppress this, a resonant gain filter was added to the fringe offset control loop, providing a differential trim voltage to each piezo to keep the Michelson leakage at the primary drive frequency to $\sim 10^{-4}$x the common drive amplitude, while still allowing upconverted noise to be detected without suppression.

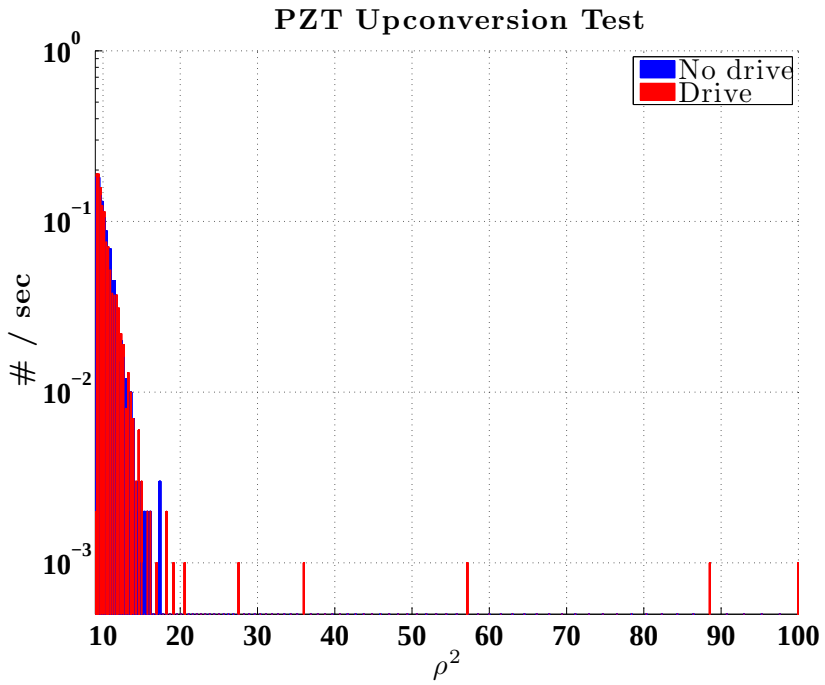

FIGURE 6.14. Distribution of triggers produced by a search for sine-Gaussian bursts in the dark port signal of the piezo Michelson. Identical searches were run on data sets both in the presence and absence of a large, low-frequency voltage drive applied in common mode to the piezo actuators in both interferometer arms.

In order to produce any detectable change in the dark signal output a significant amount of voltage had to be applied, approximately 100x more V_{rms} than is used in the LIGO OMC. At this level, the search does produce a set of non-Gaussian transients between 100 and 500 Hz, in excess of the background data set, including a few with $\rho \sim 10$. Examining the frequency of the loudest triggers it is revealed that they are centered on 300 Hz, see Figure 6.15, and are potentially due to a glitch in any of the several power supplies in the system running at 60 Hz, most likely in the piezo driver which is significantly more taxed with the common mode voltage application.

Examining the timing of the triggers in the driven scenario it is revealed that the handful of transients occur in a very brief period around 240 seconds into the test, as opposed to expectation of the typical Barkhausen phenomena which would

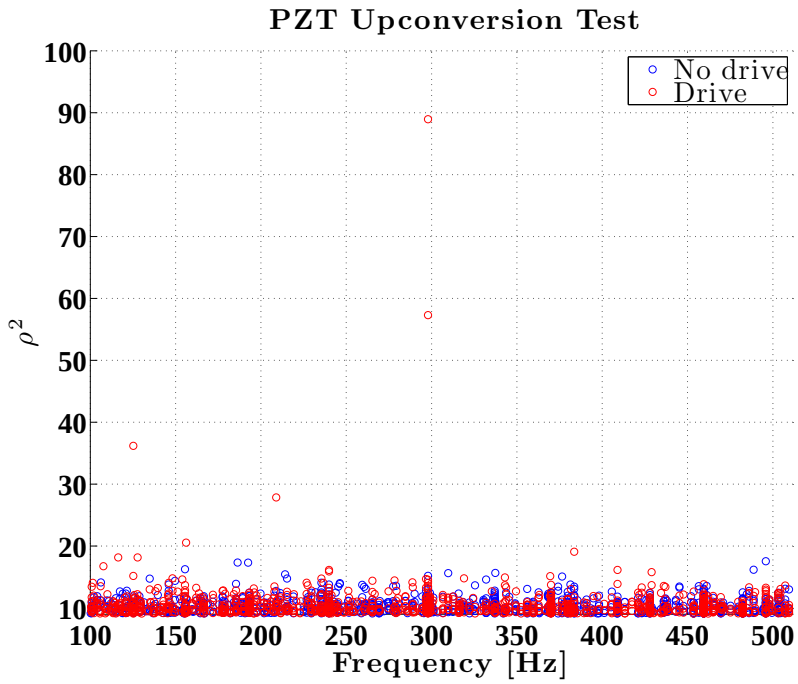

FIGURE 6.15. A scatter plot of the same data sets whose distributions are shown in Figure 6.14, useful for identifying any characteristic frequencies of the transients seen in excess of Gaussian noise. The 300 Hz power line harmonic contributes the two loudest events of the data set.

involve extra transients at any time when the drive derivative was maximized (that is, twice per second). As such, with the sensitivity of the piezo Michelson being relevant at the shot noise levels expected during OMC operation and no significant evidence of excess transients at drive levels in great excess of operational voltages, it seems safe to conclude that there will not be a direct contribution to the background from the OMC PZT.

7

Future Work

Much of the work in this thesis represents the continuation and/or evolution of years of design work and prototyping of the isolation platforms, with the significant addition of interferometric performance gauges. As the detector is pushed toward full performance, in all senses (duty cycle, stationary sensitivity, background rate), some further evolution of the platform controls will most likely take place. Two topics, which are already actively being researched but are not yet implemented widely on the detector, include the use of machine learning and the mitigation of cross-coupling effects.

7.1 Adaptive Filtering

The controls design and modeling presented earlier in this work must make use of models of the input motion, and as stated in the beginning of Chapter 3 the seismic input is quite variable. As this is the case, the design of static filters is done with an approximately median input spectrum, which provides generically well performing isolation but cannot be stated to be truly optimized all of the time. A possible solution is to implement machine learning, which adjusts the filter weights, of the blend filters for example, or a sensor correction path, in real time to respond to changes in the inputs (the sensor noises involved being well defined and stationary).

The effects of changes in the actuation plant can also be suppressed by machine learning, although these variations are probably already quite small. Considering the optimized subtraction used during S6, while it can't be stated that there was no variation in the performance of the original Wiener filters, trained in February 2010, the performance of the same filters in October shows the degradation is hard to notice. Figure 7.1 shows the subtraction factor provided by the DARM Wiener feed-forward directly after implementation and again 8 months later, at the end of the science run. Recall that this factor is in addition to a factor of ∼10x already provided by the locally tuned sensor correction, such that the overall subtraction, compared to the ground motion, is already at the few % level (so any mis-match due to a change in the actuation path must be less than this). It is conceivable, however, that a future isolation scheme would push beyond this level of isolation, and require an actively updated transfer function.

An experiment implementing an adaptive LMS [80] feed-forward algorithm (specifically the Filtered-X LMS variant [114]) was successful at the LIGO laboratory's 40m prototype instrument [115]. While the Wiener filter feed-forward described in Chapter 3 relies on previously measured correlation series and matrix inversion, the adaptive LMS technique instead estimates the necessary correlation samples each cycle and needs no matrix inversion. If the feed-forward filter weights are contained in the vector $h(n)$, then at every sample $h(n)$ will be modified following

$$h(n+1) = h(n)\left[1 - \mu\alpha\right] h(n) + \mu\epsilon(n)x(n), \tag{7.1}$$

where μ is the *adaptation rate* or *adaptation gain*, $x(n)$ is the witness input, $\epsilon(n)$ is the error signal $\epsilon(n) = x(n) - \sum_{n=1}^{N} x(n-i)h(n-i)$ (N being the filter length), and α is another gain which characterizes the *leakage factor* $[1 - \mu\alpha]$. In general, the

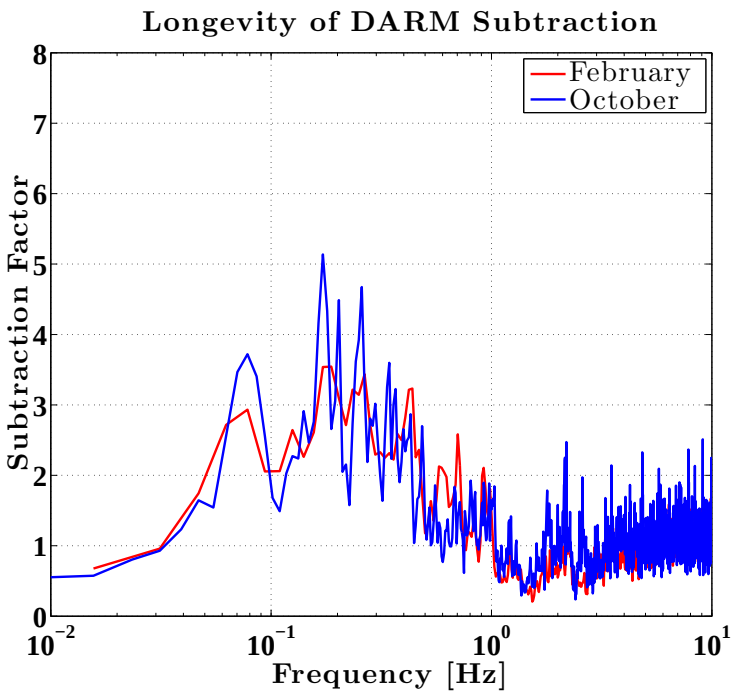

FIGURE 7.1. Comparison of the DARM feed-forward optimization over a long-term period. The subtraction filter was trained on data roughly coincident with the red trace, but the performance is very similar without retraining 8 months later, indicating that the noise coupling and actuation transfer function remain unchanged.

performance of such an estimation relies on the proper tuning of the parameter μ, the value of which effectively low-passes the estimation noise created by the variance of the time series $x(n)$, with a time constant proportional to $1/\mu$. More colloquially, slowly updating the filter weights of a relatively quickly changing system will not provide good subtraction, but quickly updating the filter weights of a relatively slowly changing system will introduce some adaptation noise. For the LIGO seismic isolation, the change in inputs is drastically slower than the calculation rate of the real-time software, and a scenario can be imagined where the filters are allowed to innovate for a period of time, perhaps a few times per day, and then the parameter μ is brought to 0, removing any adaptation noise.

The leakage factor, $[1 - \mu\alpha]$, is used to stabilize the algorithm against digital artifacts such as saturations/overflows from impulses, or other problems which

arise due to limited-precision. The leakage also effectively contributes a white noise, whose variance depends on α, to the adaptation process, such that its stabilization effect resembles the use of dither to overcome noises in digital systems [80].

7.2 Cross-Couplings

As fine tuning of the platform controls develops, one of the obstacles which arises is cross-couplings between the different degrees of freedom. These occur due to a number of reasons, including the alignment accuracy of the sensors and actuators, and unavoidable asymmetries of the mechanical assembly. For instance, there is ideally a negligible direct coupling of the vertical (Z) platform motion to the mirror's longitudinal motion, but it is nevertheless important to reduce the amount of vertical motion due to signal bleed into the rotational DOFs (RX and RY), since the three signals are constructed from the same set of sensors. Overall, the assembly and sensor alignment can produce a 1% level of cross-coupling to start, and careful measurement is needed to tune beyond this, as is done with the CPS plate alignment described in Chapter 3. Future work on the platform controls could include the analysis of the effects of more (or all) off-diagonal elements of the platform motion, with the goal of removing any limit to the performance from controller constraints between DOFs.

There is also the possibility of direct coupling of the drive signal to the sensor, that is, via the electronics pathways or magnetic fields and not through the mechanics. The BSC ISI's exhibit an effect conceivably due to this, between the vertical and horizontal "common mode" motions, which are Z and RZ. Figrue 7.2 shows the response of the Z and RZ CPS, T240 (low frequency Stage 1 seismometer), and GS13 (1 Hz, high sensitivity Stage 2 seismomter), to a Z excitation. The Z control loop is closed for this measurement, with the excitation impressed by

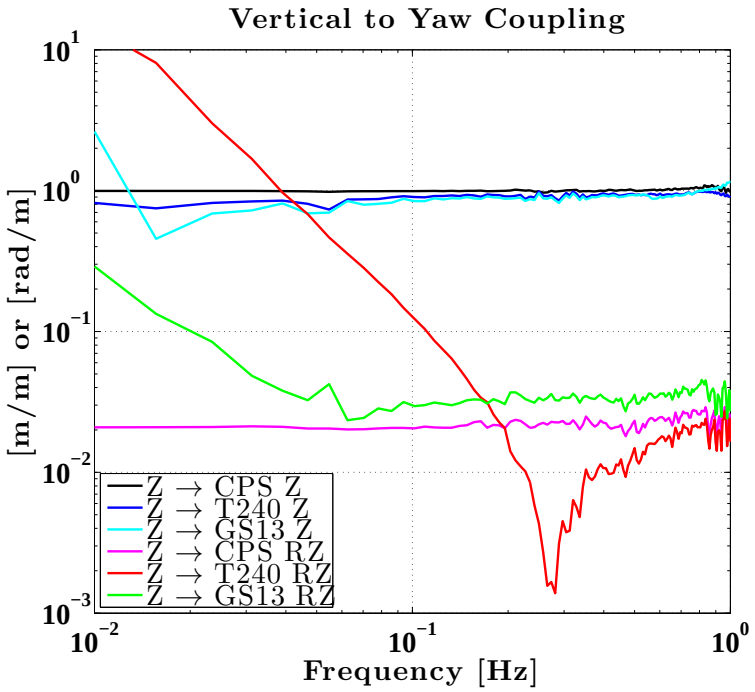

FIGURE 7.2. Response of the Z and RZ sensors to Z drive. The Z responses are all, as expected, ∼1 m/m. The RZ CPS and GS13 response of a few % is consistent with the expectation from the mechanical assembly (blade spring orientation). The GS13 measurement is noise limited below 0.1 Hz. The RZ T240 response shows a serious anomalous coupling.

the controller (the gain is very high at the frequencies in question), and the RZ motion is left uncontrolled, except for some AC coupled damping signal.

While the Z sensor responses all show the expected transfer functions of 1 m/m, the RZ T240 response is conspicuously out of the ordinary. The RZ CPS and GS13 show a several % coupling (0.02-0.03 rad/m), which is close to what is expected from the layout of the platform's blade springs. The RZ T240 is apparently measuring a summation of this transfer function with an additional $1/f^2$ coupling to Z drive. The summation is clear due to the dip where the flat 0.02 rad/m CPS transfer function meets the $1/f^2$ slope (the magnitudes are the same and the phase must be π).

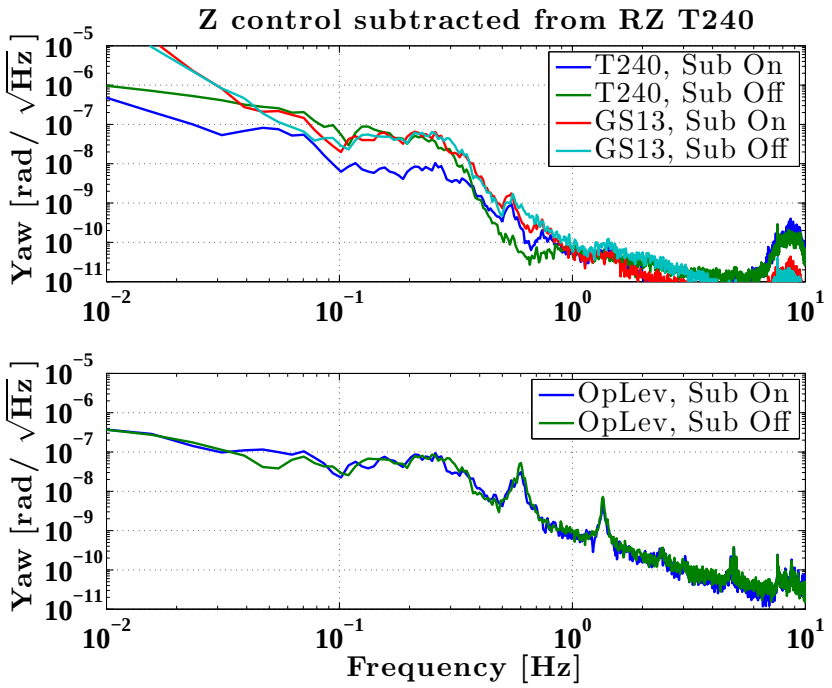

FIGURE 7.3. Test of Z control signal subtraction from the RZ T240 (error point), in order to reduce the injected yaw motion from the observed extraneous signal cross-coupling. While the T240 spectrum reports effective (a factor of ∼10x) subtraction via filtered Z control, neither the Stage 2 witness GS13 nor the optical lever reflected off the suspended test mass report any improvement in angular motion.

The size of this coupling is what takes it beyond a curiosity. If the Z control loops provide a factor of ∼10x at the microseism than the drive signal is effectively the same size as the input ground motion, which is ∼1 mu/$\sqrt{\text{Hz}}$. With a ∼0.1 rad/m coupling to RZ this creates a 100 nrad /$\sqrt{\text{Hz}}$ sensed yaw signal. In the absence of Z drive, the RZ spectrum approaches the T240 noise at these frequencies, a few nrad/$\sqrt{\text{Hz}}$, making the Z injection a sizable increase, and large enough to strain the interferometer's angular control loops which typically have a 1-3 Hz bandwidth.

Since the Z drive signal is known to high accuracy a correction signal which feeds a filtered Z control signal to the RZ error point has been shown to effectively reduce the in-loop witnesses, see FIgure 7.3 Confounding the issue, the out of loop optical lever signal is unchanged by this improvement. Also confounding the issue

are specific tests with an identical actuator and sensor, on a testbed, which are unable to produce similar couplings.

8

Conclusion

At the time of writing the installation of Advanced LIGO has been completed, and the Livingston director has been fully locked using the seismic control scheme laid out in this thesis. The detector operates on DC readout and has reached a sensitivity corresponding to a binary inspiral range in excess of 35 Mpc. To date, this is the most sensitive gravitational wave detector of its kind, and was achieved only after years of work done by hundreds of people. With the Hanford detector rapidly coming online, the community is anticipating not only the first direct detection of gravitational waves, but the era of routine detection and astronomy. A global network of detectors operating at similar sensitivities is planned, including detectors in Italy, Japan, and perhaps India.

On the way to full sensitivity the duty cycle of the instrument will be tested, with implications for the efficacy of the isolation throughout widely variable conditions including high winds, high microseismic activity, and earthquakes. The performance of the system will be judged not only on the stationary motion transmitted to the detector's test masses, but by its ability to reject transients which could contribute background events to the astrophysical signal searches. Some advanced techniques described here, and successfully implemented during eLIGO, may be useful again in keeping the instrument running as much as possible, with

the cleanest possible data stream. A brief look into the future of low frequency controls shows some promise with different schemes, all designed to improve the sensing of, and isolation from, inertial tilts, due to their strong coupling to the inertial sensors. The next few years of sensitivity realization and (hopefully) signal observation will most likely determine the needs from, and the needs of, the next generation of ground-based detectors.

Appendix A: Suspension Damping

Damping the suspensions is required for practical ring-down times and ease of mechanical actuation at their resonant frequencies, but there are costs, beyond increased thermal noise, involved with introducing any loss into the system as well as a somewhat subtle difference in the two main instances of pendulum damping used in LIGO. This difference arises between the suspended seismic platforms and the suspended mirrors. The platforms are large and support inertial sensors as part of their payload, allowing for viscous damping against inertia. The mirrors, however, do not support any extra instrumentation, so their velocity is damped relative to their support cages, and this distinction has important implications for the passive isolation. At equilibrium $\sum F = 0$, and we can write the equation of motion of the inertially damped pendulum as

$$m\ddot{x}_1 - b\dot{x}_1 - k(x_1 - x_0) = 0. \tag{1}$$

Converting this to a frequency dependent transfer function, by use of the Laplace transform, and substituting the parameters $k = m\omega_0^2$ and $b = m\omega_0/Q$, we find that

$$\frac{x_1(\omega)}{x_0(\omega)} = \frac{\omega_0^2}{\omega_0^2 - \omega^2 + \frac{i\omega\omega_0}{Q}}, \tag{2}$$

where the $1/\omega^2$ nature of the roll-off is preserved, for $\omega > \omega_0$, no matter the Q value to which the pendulum is damped (and in practice they are damped to a Q of $\sim$1).

For the pendulum damped relative to its support, like the test mass suspensions, the equation of motion is modified to be

$$m\ddot{x}_1 - b(\dot{x}_1 - \dot{x}_0) - k(x_1 - x_0) = 0, \tag{3}$$

and the modified transfer function is

$$\frac{x_1(\omega)}{x_0(\omega)} = \frac{\omega_0^2 + \frac{i\omega\omega_0}{Q}}{\omega_0^2 - \omega^2 + \frac{i\omega\omega_0}{Q}}. \tag{4}$$

There is now a zero, at $\omega = w_0 Q$, which turns the $1/\omega^2$ cut-off into a less impressive $1/\omega$. So, the more damped the pendulum becomes (that is, the lower the Q), the less isolation it provides! With a fundamental resonance at 0.5 Hz, damped to a Q of 10, the isolation is already compromised at 5 Hz, seemingly a disaster. This effect is overcome by avoiding truly viscous damping, instead using the freedom gained via the digital control system to implement filters whose frequency response is tuned to introduce losses only around the suspension resonances, while attenuating the damping force at other frequencies. In this way, even the pendulum damped relative to its support can offer $1/\omega^2$ isolation and a reasonable Q simultaneously.

Although the isolation transfer function of the inertially damped pendulum maintains its $1/\omega^2$ shape even when the Q is reduced to $\sim$1, there is the slight curiosity of what the transfer function from the inertial input motion to the relative position sensor looks like. In this case, the transfer function becomes

$$\frac{x_1(\omega) - x_0(\omega)}{x_0(\omega)} = \frac{\omega^2 - \frac{i\omega\omega_0}{Q}}{\omega_0^2 - \omega^2 + \frac{i\omega\omega_0}{Q}}. \tag{5}$$

A term in the numerator reappears, such that this function falls as only a factor of ω towards zero frequency when heavily damped, but ω^2 when the Q is high (undamped). Effectively, one of the zeros at zero frequency has moved up to a new frequency, ω_0/Q. In any damping configuration, the transfer function approaches a magnitude of 1 at $\omega > \omega_0$, i.e. the relative position sensor becomes simply a measurement of the input motion (or, as is more common in practice, its own instrument noise).

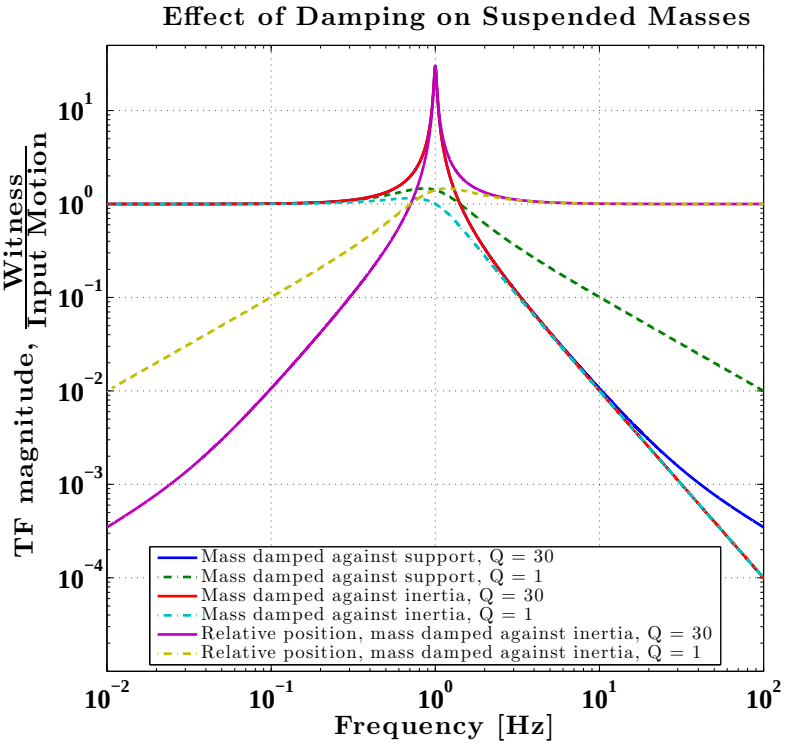

FIGURE A.1. Effect of viscous damping on isolation transfer functions of a suspended mass, with two different Q parameters.

Appendix B: Per Square Root Hz

One of the chief signal processing tools used in noise analysis is the *spectral density*. The amplitude spectral density is portrayed numerous times in this thesis, for various physical quantities, with the somewhat peculiar unit of, for example, "meters *per square root Hz*". In order to determine the frequency content of a well defined signal one simply takes its *Fourier transform*, that is, for a signal time series $x(t)$ one calculates

$$\tilde{x}(\omega) = \int_{-\infty}^{\infty} x(t) e^{-i\omega t} dt, \tag{6}$$

where ω is the angular frequency, and the $\sim$ denotes that $\tilde{x}(\omega)$ is the transform pair of $x(t)$. When the angular frequency convention is used, a constant normalization factor must be applied in the definition of the *inverse* Fourier transform,

$$x(t) = \frac{1}{2\pi} \int_{-\infty}^{\infty} \tilde{x}(\omega) e^{i\omega t} d\omega. \tag{7}$$

For noise analysis the signal is often less well defined, instead being formed by a random time series which asymptotically obeys some probability distribution function. In order to examine the frequency content of such signals, assuming they are stationary, instead of the Fourier transform of the signal one uses the Fourier transform of its *auto-correlation* series, $r(t)$, via the calculation

$$S_{xx}(\omega) = \int_{-\infty}^{\infty} r(t)e^{-i\omega t}dt = \int_{-\infty}^{\infty} \left[\int_{-\infty}^{\infty} x(\tau)x(\tau + t)d\tau \right] e^{-i\omega t}dt, \tag{8}$$

where τ is the *lag*. The quantity $S_{xx}(\omega)$, which is the Fourier pair of the auto-correlation, is known as the *power spectral density* (PSD), often referred to as simply the *spectrum*. This choice of name becomes clear when the dimension of $S_{xx}(\omega)$ is examined: $r(t)$ has the dimension of $x(t)$ squared, and the dt brings a unit of time. If, as is often the case in experimental work, $x(t)$ is a voltage signal, then $r(t)$ has units of V^2 and $S_{xx}(\omega)$ has units of $\mathrm{V}^2{\cdot}\mathrm{s}$, or equivalently, V^2/Hz, that is, Volts squared *per Hertz*, hence the use of the word *density*. So, the value of the power spectral density at a frequency ω is the contribution, per unit bandwidth, to the signal's overall noise power from components fluctuating at ω. Often times the experimenter is not interested in the power, but the amplitude spectral density (ASD) of the signal, whether it be a voltage, current, or even displacement as is seen in this work, so the square root of $S_{xx}(\omega)$ is taken, and we arrive at the unit of, for example, $\mathrm{V}/\sqrt{\mathrm{Hz}}$.

Also, the reason the power spectrum is depicted here with the xx subscript is because there is an analogous quantity when the information of two time series is combined, known as the *cross-spectral density* (CSD). In the CSD the cross-correlation is Fourier transformed instead of the PSD's auto-correlation, and it would be written in this notation as $S_{xy}(\omega)$ if the second time series was $y(t)$. A very important statistical measure of the relationship between two signals is the *coherence*, $\gamma_{xy}(\omega)$, which involves both the PSD and the CSD via the relation

$$\gamma_{xy}(\omega) = \frac{|S_{xy}(\omega)|^2}{S_{xx}(\omega)S_{yy}(\omega)}. \tag{9}$$

An example: if a time series, $x(t)$ is *white* then we say that each of its samples is uncorrelated with all the other samples, and so its auto-correlation series becomes

$$r(t) = \begin{cases} \sigma^2, & \text{t} = 0. \\ 0, & \text{otherwise.} \end{cases} \tag{10}$$

where σ^2 is the variance of the distribution which the samples of $x(t)$ belong to. Equivalently, one can write

$$r(t) = \sigma^2 \delta(t), \tag{11}$$

where $\delta(t)$ is the Dirac delta function. The spectrum of this signal will then be equal at all frequencies (hence the term *white*), with the value $S_{xx}(\omega) = \sigma^2$. The shot noise of a photocurrent, i_{DC}, is a prime example of white noise, and the value of the ASD is found by the simple relation

$$\sqrt{S_{ii}(\omega)} = \sqrt{2ei_{DC}}, \tag{12}$$

where e is the fundamental charge and the unit of $\sqrt{S_{ii}(\omega)}$ is $\text{A}/\sqrt{\text{Hz}}$. If one digitizes a shot noise limited photocurrent and then calculates its ASD, the value will not vary with the length of time collected (i.e. looking to lower frequencies), or with the digitization rate (i.e. looking to higher frequencies), although the total integrated power will scale.

Another example for contrast: if a times series, $x(t)$, is a sinusoid, then all of its noise power is contained in a single frequency bin, at the frequency of the oscillation. The ASD of such a signal, not its autocorrelation, resembles a Dirac delta function, and in practice its peak amplitude will vary with changes in the ASD calculation parameters. Here, the rms amplitude of the signal becomes more

informative, and to determine this the bandwidth of the ASD must be accounted for.

For instance, imagine a sinusoidal signal, with amplitude A and frequency f, is being measured on top of some background noise which is white with variance σ^2. The ASD of the combined signal and noise will be a peak accompanied by a frequency independent constant, as shown in Figure B.1. Let $A = 100$ "counts" peak, and $f = 1$ Hz, and $\sigma^2 = 1$. If the length of time series collected to calculate the ASD is $T = 10$ seconds, as is true for the blue trace in Figure B.1, the spectral height of the signal will become $A/\sqrt{2}/\sqrt{1/T} \simeq 224$ cts/$\sqrt{\text{Hz}}$, where the factor of $\sqrt{2}$ converts peak amplitude to rms amplitude of a sine wave, and the $\sqrt{1/T}$ is the width of each bin. If, as is true for the red trace in Figure B.1, the length of the time series becomes $T = 50$ seconds, the constant floor of the ASD will remain unchanged, but the height of the signal will increase to 500 cts/$\sqrt{\text{Hz}}$, since its energy is contained in a vanishingly narrow frequency bin. This is not a triviality of signal processing, indeed it is the core of many analyses: when looking for an oscillating signal on top of a noise background, integrating for a longer time improves the peak height as $\sqrt{T}$.

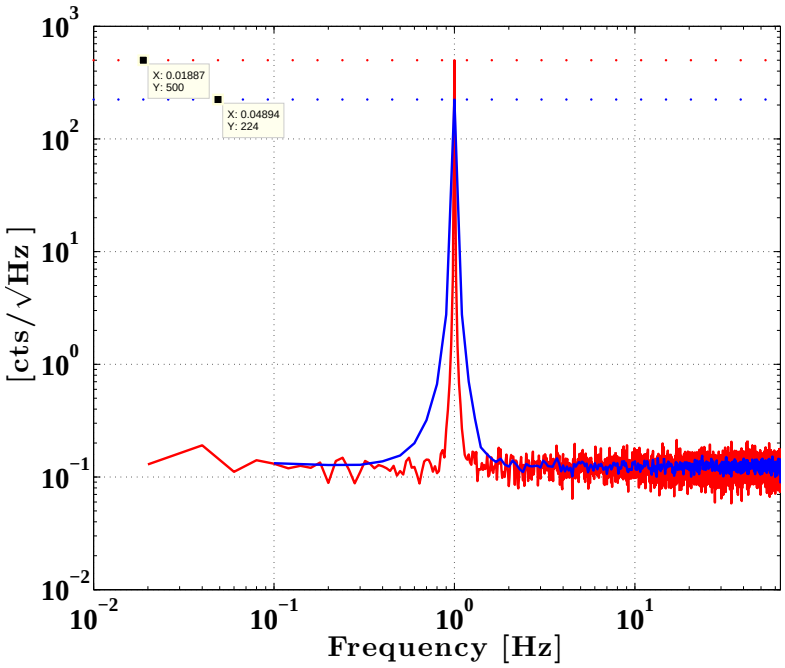

FIGURE B.1. Example ADSs, displaying the different behavior of a well defined sinusoid at 1 Hz and a white background noise. Increasing the integration time by 5 increases the peak height by $\sqrt{5}$, but leaves the variance of the background noise unchanged.

Appendix C: Feedback Basics

Although a rich and varied topic, even just the basic trappings of feedback control prove highly useful in experimental work. Applications include the suppression of external disturbances to allow for sensitive measurements, or the stabilization of an unstable system to allow for any measurements at all. A simple single-input single-output (SISO) control loop is all that is needed to lay out the important aspects, as shown in Figure C.1. The combination of the elements in the figure is often referred to as a *servomechanism*.

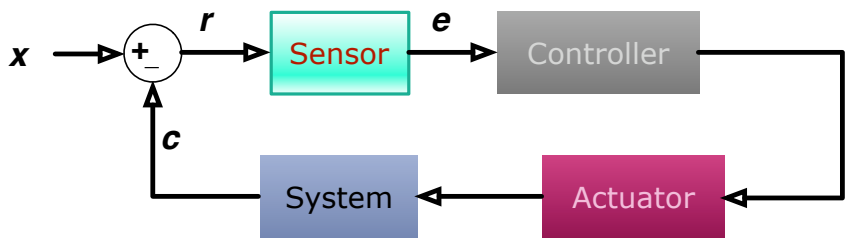

FIGURE C.1. A simplified SISO control loop. The controller takes as a reference the output of the sensor, known as the error signal, e, and uses the actuator to manipulate the system to be controlled. The output of the system is the control signal, c, which attempts to cancel the external disturbance, x, with the residual disturbance, r, remaining. The sensor converts r into the error signal, e.

Let the Controller be $C(\omega)$, the Actuator be $A(\omega)$, the System be $S(\omega)$, and the sensor be $H(\omega)$. All of these are functions of frequency, and are assumed to be linear, and time-invariant. Their product is the *open loop gain*, $G(\omega)$, and the sub-product $A(\omega)S(\omega)$ is, in control theory lingo, called the plant, $P(\omega)$ which was

referred to for many of the mechanical systems discussed in the main body of this text. In some texts the system is referred to as the *process*.

In reality both the sensor and actuator will be accompanied by their own self-noises, but these can be disregarded for simple analysis. Indeed, assuming the sensor is a faithful reporter of the system output we can ignore $H(\omega)$ totally, with the result being e and r become identical. Combining $S(\omega)$ and $A(\omega)$ into $P(\omega)$, the diagram reduces to that shown in Figure C.2, where now $G(\omega) = P(\omega)C(\omega)$.

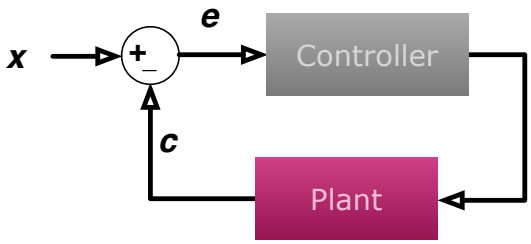

FIGURE C.2. An even more simplified SISO control loop. The sensor and actuator are assumed to be noiseless, and $H(\omega) = 1$ (that is to say, the sensor generates a perfect representation of r, such that $r = e$.)

To calibrate the error or control signals in terms of the external disturbance all one needs to know is the loop gain. Since $e = x - c$, and $c = eG(\omega)$, it must be true that

$$x = c\frac{1+G}{G}, \tag{13}$$

and that

$$x = e(1+G). \tag{14}$$

While $G(\omega)$ is the open loop gain, the quantity $G/(1+G)$ is the inverse of what is called the *closed loop gain*. In practice these relations boil down to this: where the loop gain is high, the control signal is approximately equal to the input disturbance,

whereas where the loop gain is low, the error signal is approximately equal to the input disturbance.

The design of $G(\omega)$ is guided by the requirements of the servo and possibility of inverting the plant. Considerations include how much bandwidth is needed to achieve the necessary suppression of input disturbance, how much sensor and actuator noise can be tolerated, and how robust the response of the controller needs to be against impulsive inputs.

While solving the problem of determining a good $G(\omega)$, there is a strict requirement which must be heeded on $G(\omega)$'s frequency response, indeed it is the fundamental problem in feedback control: *stability*. When the loop is closed, the error signal is equal to the suppressed disturbance, $e = x/(1 + G)$. At frequencies where the magnitude of the open loop gain, a complex quantity, approaches unity ($|G(\omega)| = 1$), the phase of $G(\omega)$ must not be $\pm\pi$, or else the value of $x/(1 + G)$ will diverge, and the control loop will be unstable.

If the control loop only crosses unity gain at one frequency, unsurprisingly called the *unity gain frequency* (UGF), then the difference between the phase of $G(\omega)$ at that frequency and $\pm\pi$ is referred to as the *phase margin* of the loop. The amount of additional gain that would be required to push the UGF to the point where the phase becomes unstable is referred to as the *gain margin*. A controller which produces an open loop gain which never approaches phase instability is referred to as *unconditionally stable*, and is not dependent on operating with a particular bandwidth. In LIGO the need for low frequency suppression, since the greatest disturbance to be overcome is the seismically driven motion of the mirrors, often dictates the need for *conditionally stable* controls, which can operate at the designed bandwidth but not much above or below this. A Bode plot of three open loop gains for comparison is shown in Figure C.3.

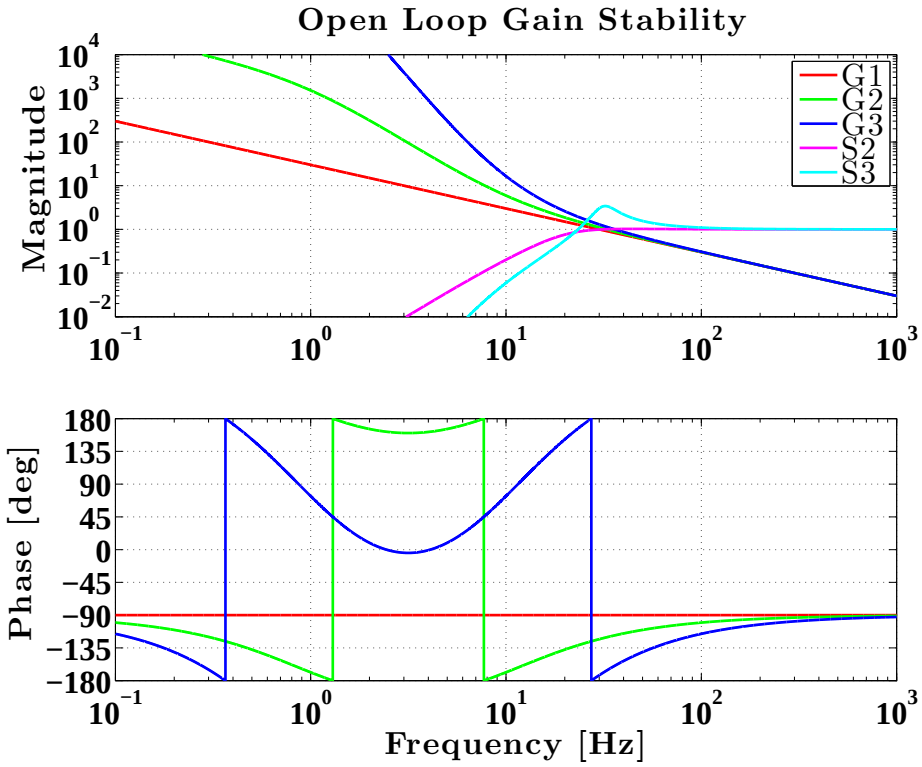

FIGURE C.3. Three example open loop gains. $G1$, in red, is a simple $1/f$ control loops, which is unconditionally stable. $G2$, in green, features more low frequency gain, but the phase dips below $-\pi$, producing a region where, should unity gain fall there, would become unstable. $G3$, in blue, has even more gain, and shows that decreasing phase around unity gain is not a simple threshold effect, but instead produces excess motion around unity gain, "gain peaking", as seen in the lighter blue curve, $S3 = 1/(1 + G3)$.

Appendix D: The PSL

Significant efforts are made to prepare the laser beam before it enters the interferometer, and this system has been the subject of lengthy study by several people [116, 117]. The basic layout of the PSL is as follows:

- The beam originates from a commercially available 2 W NPRO [118], a solid state laser (Nd:YAG crystal) with a high degree of frequency and polarization purity, with a wavelength of 1.064 µm (∼282 THz). An internal servo is used to damp the ∼1 MHz relaxation oscillation.

- The NPRO output travels through a single-shot power amplifier (the MOPA, or Master Oscillator Power Amplifier), which contains several Nd:YVO crystals which are pumped with 808 nm light from a high power laser diode, coupled through optical fibers. The output of the MOPA is 35 W.

- The MOPA output travels through another amplification stage, the HPO (High Power Oscillator), which is injection locked and contains Nd:YAG crystals, also pumped with the 808 nm diode light. The HPO can output laser power in excess of 200 W.

- Now that there are plenty of photons, several stabilization stages follow. The first is the PMC (Pre-Mode Cleaner), a 2 m resonator cavity with a finesse of ∼125. The PMC performs several duties, including the suppression of higher

order transverse modes (non TEM_{00}), hence its name. It also passively filters intensity noise at high frequencies, due to its $\delta f = 300$ kHz cavity pole. Although not in the detection band, this is an important factor since it reduces intensity noise at the main RF sideband frequencies (9 and 45 MHz for aLIGO, used for controlling the interferometric cavities) before they are impressed on the beam via an electro-optic modulator (EOM) downstream of the PMC. The PMC is locked to the main laser frequency with a ∼10 kHz PDH servo, actuating with a PZT attached to one of the cavity mirrors. When operating at full power the intensity on the PMC mirrors is quite high, $\sim 10^{10}$ W/m^2.

- A beam picked off from the PMC transmission is used for active intensity stabilization. The power fluctuations are measured on a photodiode, whose output forms the error point of a ∼100 kHz servo. Actuation is achieved with an acousto-optic modulator (AOM), which diffracts a varying amount of the light from the main beam to suppress the fluctuations. The degree to which the power can be stabilized is limited by the shot noise in the sensor beam, $RIN_{shot} = \sqrt{2e/i_{DC}}$, where e is the fundamental charge, and i_{DC} is the photocurrent on the photodiode. This servo is typically expected to provide a RIN no larger than 10^{-8} $1/\sqrt{\text{Hz}}$ in the audio band.

- Another beam picked off after the PMC is locked, with a ∼500 kHz PDH servo, to a 20 cm suspended cavity, known as the reference cavity, which is kept under high vacuum and temperature stabilized. The cavity is formed with two mirrors attached to a rigid spacer, and the finesse is quite high, in excess of 10^4. This serves as the vanguard of a multi-stage frequency stabilization scheme, eventually replaced as the reference by the 16.5 m input

mode cleaner, and then by the 4000 m common arm length. The free-running frequency noise spectrum of the NPRO is around 100 Hz/$\sqrt{\text{Hz}}$ at 100 Hz, with a roughly $1/f$ characteristic, and the frequency stabilization servo in the PSL suppresses this by several orders of magnitude.

Appendix E: Lock Acquisition

Before the detector is capable of producing data useful for gravitational wave detection it must be brought to its operating point, a process referred to as "locking the interferometer". In the past (iLIGO and eLIGO) this process was stochastic, waiting for the error points of the various length feedback loops to develop into suitable signals when the mirrors swung through resonance by chance ("grabbing the fringe"). The suitability of the signals was gauged by monitoring the power level at various points in the interferometer, with fast switching of the controls path triggered based on these monitors. A detailed description of the procedure is given in [120]. Depending on the residual seismic motion the "fringe velocity" can become high enough that the mean time to acquire lock with this method is uncomfortably high.

The force required to stop the mirrors in time is proportional to the cavity finesse and, unfortunately, to the square of the mirror velocity, $F_{req} \propto mv^2\mathcal{F}$. Transitioning the iLIGO lock acquisition scheme to aLIGO would be difficult for a number of reasons, including:

- Reaching high sensitivity at 10 Hz places technical limits on the actuator noises, which in turn limits the range (available peak force) of the mirror drive to much smaller numbers than iLIGO (from 25 mN to ∼100 µN). The increase in mirror mass, from 10 kg to 40 kg, also decreases how much

acceleration the mirror experiences for a given force, but this also cuts the force noise coupling so the point is moot.

- There is an additional cavity to lock (the SRC) in aLIGO
- The rms residual mirror velocity is not much different between the detector generations

In light of these and similar concerns, a new scheme was devised to introduce deterministic (or at least partially deterministic) locking [119]. Two important features of the new scheme are:

- An auxiliary Nd:YAG laser beam is injected into each arm cavity, frequency doubled to 532 nm and phase locked to the main laser, and then PDH locked to the arm as a readout of the mirror motion [121]
- An RF sensing scheme in the corner station which senses the MICH, PRC, and SRC degrees of freedom well, but is not sensitive to the resonance conditions in the arm cavities [122]

First the arm lengths are sensed individually with their green lasers. Then two beat signals are developed, one which compares the X arm with the PSL and the other which compares the two arms. The PSL is then locked to the X arm length, and the Y arm to the X arm by actuating its mirrors.

An offset into the PSL vs. X arm beat will then allow for the two arms to be pushed off of and held off of resonance, allowing for the corner to be locked in the usual stochastic fashion. Once the corner is locked, the frequency offset in the arm servo can step the arm cavities back onto resonance in a controlled fashion, a process referred to as the CARM "offset reduction". The green beat sensing is not

sufficient to place the arms directly onto the ultra-narrow CARM resonance (the coupled cavity has sub-Hz linewidth), so a procession of suitable errors signals is traversed as the cavity narrows, including DC signals in transmission of the arms and finally RF signals in reflection [123].

Appendix F: Permissions

Several figures describing the global feed-forward work presented in Chapter 3 was previously published in Classical and Quantum Gravity, in an article written by the author and his collaborators. Once accepted, the right to reproduce the content of the article in a dissertation was granted by the publisher, the following is a communication between the author and the publisher:

"Dear Ryan DeRosa,

Thank you for your email and for taking the time to seek this permission.

When you assigned the copyright in your article to IOP, we granted back to you certain rights, including the right to include the article within any thesis or dissertation.

Therefore, please go ahead and make what use you wish of the content of the article.

The only restriction is that if, at a later date, your thesis were to be published commercially, further permission would be required.

Please let me know if you have any further questions.

In the meantime, I wish you the best of luck with the completion of your dissertation.

Kind regards,

L. Evans

Publishing Assistant

IOP Publishing

Please note: We do not usually provide signed permission forms as a separate attachment. Please print this email and provide it to your publisher as proof of permission."

References

[1] C. W. Misner, K. S. Thorne, and J. A Wheeler. *Gravitation*, W. H. Freeman, San Francisco, 1973.

[2] P. Linsay, P. Saulson, R. Weiss, S. Whitcomb. *A study of a long baseline gravitational wave antenna system*. Proposal to the NSF, 1983.

[3] P. R. Saulson. *Fundamentals of Interferometric Gravitational Wave Detectors*. World Scientic Publishing Company, 1994.

[4] R. A. Hulse and J. H. Taylor. Discovery of a pulsar in a binary system. *Astrophys. J. Lett.*, 195:L51-L53, January 1975.

[5] J. M. Weisberg and J. H. Taylor. The relativistic binary pulsar B1913+16: Thirty years of observations and analysis. *Binary Radio Pulsars*, vol. 328 of *Astronomical Society of the Pacific Conference Series*, July 2005.

[6] J. Abadie et al. Search for gravitational waves from low mass compact binary coalescence in LIGOs sixth science run and Virgos science runs 2 and 3. *Phys. Rev. D*, 85:082002, April 2012

[7] H. Dimmelmeier, C. D. Ott, A. Marek, H. T. Janka. The gravitational wave burst signal from core collapse of rotating stars. *Phys.Rev. D*, 78:064056, 2008

[8] C. D. Ott, E. P. O'Connor, S. Gossan, E. Abdikamalov, U. C. T. Gamma, S. Drasco. Core-Collapse Supernovae, Neutrinos, and Gravitational Waves. *Proceedings of the Neutrino 2012 Conference, Kyoto Japan*, June 2012

[9] B. Abbott et al. Upper limits on gravitational wave emission from 78 radio pulsar. *Phys. Rev. D*, 76(4):042001 , August 2007.

[10] M. Pitkin, the LIGO Scientific Collaboration. Searching for gravitational waves from known pulsars. *Classical and Quantum Gravity*, 22:277, 2005.

[11] J. Aasi et al. Gravitational Waves from Known Pulsars: Results from the Initial Detector Era. *Ap. J.*, 785:119, 2014.

[12] L. P. Grishchuk. Primordial gravitons and possibility of their observation. *JETP*, 23:293, March 1976.

[13] A. A. Penzias, R. W. Wilson. A Measurement Of Excess Antenna Temperature At 4080 Mc/s. *Astrophysical Journal Letters*, 142: 419421, July 1965.

[14] R. H. Dicke, P. J. E. Peebles, P. J. Roll and D. T. Wilkinson. Cosmic Black-Body Radiation. *Astrophysical Journal Letters*, 142: 414419, July 1965.

[15] M. Maggiore. Gravitational Wave Experiments and Early Universe Cosmology. *Physics Reports*, 331:283-367, 2000.

[16] B. Allen. The stochastic gravity-wave background: sources and detection. *Proceedings of the Les Houches School on Astrophysical Sources of Gravitational Waves*, 1996.

[17] B. Allen, J. D. Romano. Detecting a stochastic background of gravitational radiation: Signal processing strategies and sensitivities. *Phys. Rev. D*, 59:102001, 1999.

[18] K. Grover, S. Fairhurst, B.?F. Farr, I. Mandel, C. Rodriguez, T. Sidery, and A. Vecchio. Comparison of gravitational wave detector network sky localization approximations. *Phys. Rev. D*, 89:042004, February 2014.

[19] E. Thrane, N. Christensen, R. Schofield. Correlated magnetic noise in global networks of gravitational-wave interferometers: observations and implications. *Phys. Rev. D.* 87:123009, 2013.

[20] E. Flanagan. The Sensitivity of LIGO to a Stochastic Background, and its Dependance on the Detector Orientations. *Phys.Rev.D*, 48:2389-2407,1993.

[21] The LIGO Collaboration and the Virgo Collaboration. An upper limit on the stochastic gravitational-wave background of cosmological origin. *Nature*, 460:990-994, August 2009.

[22] B. P. Abbott et al. An Upper Limit on the Stochastic Gravitational-Wave Background of Cosmological Origin. *Nature*, 460:990-994, August 2009.

[23] J. Abadie et al. Upper limits on a stochastic gravitational-wave background using LIGO and Virgo interferometers at 600-1000 Hz. *Phys. Rev. D*, 85:122001, June 2012.

[24] J. Weber. Detection and Generation of Gravitational Waves. *Phys. Rev.*, 117:306, January 1960.

[25] J. Weber. Evidence for the Discovery of Gravitational Radiation. *Phys. Rev. Lett.*, 22:1320, June 1969.

[26] J. L. Levine, R. L. Garwin. Absence of Gravity-Wave Signals in a Bar at 1695 Hz. *Phys. Rev. Lett.*, 31:173, July 1973.

[27] J. L. Levine and R. L. Garwin. New Negative Result for Gravitational Wave Detection, and Comparison with Reported Detection. *Phys. Rev. Lett.*, 33:794, September 1974.

[28] E. Mauceli, Z. K. Geng, W. O. Hamilton, W. W. Johnson, S. Merkowitz, A. Morse, B. Price, and N. Solomonson. The Allegro gravitational wave detector: Data acquisition and analysis. *Phys. Rev. D*, 54:1264, July 1996

[29] A. Morse, W.O. Hamilton, W. W. Johnson, E. Mauceli, M.P. McHugh. Calibration and sensitivity of resonant-mass gravitational wave detectors. *Phys. Rev. D*, 59:062002, February 1999.

[30] R. Weiss. *Electromagnetically Coupled Broadband Gravitational Antenna.* MIT Quarterly Progress Report, April 1972.

[31] C. Fabry, A. Perot. On a new form of interferometer. *Astrophys. J.*, 13:265, May 1901.

[32] A. E. Siegman. *Lasers.* University Science Books, 1986.

[33] R. W. P. Drever et al. Laser Phase and Frequency Stabilization Using an Optical Resonator. *Appl. Phys. B*, 31:97-105, 1983.

[34] J. Levine and R. Stebbins. Upper Limit on the Gravitational Flux Reaching the Earth from the Crab Pulsar. *Phys. Rev. D*, 6(6):1465, September 1972.

[35] A. A. Michelson, E. W. Morley. On the Relative Motion of the Earth and the Luminiferous Ether. *American Journal of Science*, 34:333345, 1887.

[36] B. J. Meers. Recycling in laser-interferometric gravitational-wave detectors. *Phys. Rev. D*, 38:2317-2326, October 1988.

[37] J. E. Mason, P. A. Willems. Signal Extraction and optical design for an advanced gravitational-wave interferometer. *Applied Optics*, 42:1269-1282, March 2003.

[38] H. B. Callen and T. A. Welton. Irreversibility and generalized noise. *Phys. Rev.*, 83:3440, 1951

[39] P. R. Saulson. Thermal noise in mechanical experiments. *Phys. Rev. D*, 42:2437-2445, 1990.

[40] Y. Levin. Internal thermal noise in the LIGO test masses: a direct approach. *Phys. Rev. D*, 57:659-663, 1998.

[41] G. M. Harry et al. Thermal noise in interferometric gravitational wave detectors due to dielectric optical coatings. *Classical and Quantum Gravity*, 19:897-917, 2002.

[42] K Yamamoto et al. Current status of the CLIO project. *J. Phys. Conf. Ser.*, 122:012002 ,2008.

[43] K. Somiya. Detector configuration of KAGRAthe Japanese cryogenic gravitational-wave detector. *Classical and Quantum Gravity*, 29:124007, 2012.

[44] Punturo et al. The Einstein Telescope: a third-generation gravitational wave observatory. *Classical and Quantum Gravity*, 27(19):194002, 2010.

[45] http://sci.esa.int/ngo/49839-ngo-assessment-study-report-yellow-book/

[46] G Hobbs et al. The International Pulsar Timing Array project: using pulsars as a gravitational wave detector. *Classical and Quantum Gravity*, 27(8):084013, 2010.

[47] P. A. R. Ade et al (BICEP Collaboration). Detection of B-Mode Polarization at Degree Angular Scales by BICEP2. *Phys. Rev. Lett*, 122:241101, June 2014.

[48] C. Caves. Quantum-mechanical noise in an interferometer. *Phys. Rev. D*, 23:1693, 1981.

[49] The LIGO Scientific Collaboration. A gravitational wave observatory operating beyond the quantum shot-noise limit. *Nature Physics*, 7:962-965, 2011.

[50] J. Aasi et al. Enhanced sensitivity of the LIGO gravitational wave detector by using squeezed states of light. *Nature Photonics*, 7:613-619, 2013.

[51] M. Evans, L. Barsotti, J. Harms, P. Kwee, H. Miao. Realistic Filter Cavities for Advanced Gravitational Wave Detectors. *Phys. Rev. D*, 88:022002, 2013.

[52] E. Flanagan, K. S. Thorne. Noise Due to Backscatter Off Baffles, the Nearby Wall, and Objects at the Far end of the Beam Tube. LIGO technical report T940063, 1994.

[53] D. J. Ottoway, P. Fritschel, and S. J. Waldman. The Impact of Upconverted Scattered Light on Advanced Interferometric Gravitational Wave Detectors. *Optics Express*, 20:8329, 2012.

[54] B. P. Abbott et al. LIGO: the Laser Interferometer Gravitational-Wave Observatory. *Rep. Prog. Phys.*, 72:076901, 2009.

[55] T. Accadia et al. Virgo: a laser interferometer to detect gravitational waves. *Journal of Instrumentation*, 7:03012, 2012.

[56] H. Grote for the LSC. The GEO 600 status. *Classical and Quantum Gravity*, 27:084003, 2010.

[57] K. Kawabe for the TAMA collaboration. Status of TAMA project. *Classical and Quantum Gravity*, 14:1477, 1997.

[58] T. Fricke et al. DC readout experiment in Enhanced LIGO. *Classical and Quantum Gravity*, 29:065005, 2012.

[59] N. Smith-Lefebvre. Optimal alignment sensing of a readout mode cleaner cavity. *Optics Letters*, 36:4365-4367, 2011.

[60] G. M. Harry for the LSC. Advanced LIGO: the next generation of gravitational wave detectors. *Classical and Quantum Gravity*, 27:084006, 2010.

[61] Virgo collaboration, https://wwwcascina.virgo.infn.it/advirgo/docs.php

[62] B. F. Schutz. Networks of gravitational wave detectors and three figures of merit. *Classical and Quantum Gravity*, 28:125023, 2011.

[63] http://gwastro.org/for%20scientists/gravitational-wave-interferometer-noise-calculator

[64] The LIGO Scientific Collaboration and the Virgo Collaboration. Prospects for Localization of Gravitational Wave Transients by the Advanced LIGO and Advanced Virgo Observatories. http://arxiv.org/abs/1304.0670

[65] The LIGO Scientific Collaboration and the Virgo Collaboration. Predictions for the Rates of Compact Binary Coalescences Observable by Ground-based Gravitational-wave Detectors. *Classical and Quantum Gravity*, 27:171001, 2010.

[66] P. Melchior. *The tides of the planet earth*. Pergamon Press, Oxford 1983.

[67] E.J. Daw, J.A. Giaime, D. Lormand, M. Lubinksi, J. Zweizig. Long term study of the seismic environment at LIGO. *Classical and Quantum Gravity*, 21(9): 2255-2275, April 2004.

[68] R. X. Adhikari. Gravitational radiation detection with laser interferometry. *Review of Modern Physics*, 86, February 2014.

[69] W. Hua et al. Low Frequency Active Vibration Isolation for Advanced LIGO. *Proceedings SPIE 5500, Gravitational Wave and Particle Astrophysics Detectors*, September 2004.

[70] C. Hardham et al. Multi-DOF Isolation and Alignment with Quiet Hydraulic Actuators. *Proceedings of ASPE Spring 2004 Topical Meeting on Control of Precision Systems*, 2004.

[71] W. Hua. *Low Frequency Vibration Isolation and Alignment System for Advanced LIGO*. PhD thesis, Stanford University, June 2005.

[72] W. Hua, D.B. DeBra, C.T. Hardham, B.T. Lantz, J.A. Giaime. Polyphase FIR Complementary Filters for Control Systems. *Proceedings of ASPE Spring 2004 Topical Meeting on Control of Precision Systems*, 2004.

[73] S. Wen et al. Hydraulic External Pre-Isolator System for LIGO. *Classical and Quantum Gravity*, 31:235001, November 2014.

[74] S. Wen. *Seismic Isolation for the Laser Interferometer Gravitational Wave Observatory with Hydraulic External Pre-Isolator System*. PhD thesis, Louisiana State University and Agricultural and Mechanical College, May 2009.

[75] R. DeRosa et al. Global feed-forward vibration isolation in a km scale interferometer. *Classical and Quantum Gravity*, 29(21): 5008-5023, October 2012.

[76] N. Wiener. *Extrapolation, Interpolation, and Smoothing of Stationary Time Series, with Engineering Applications*. MIT Press, Cambridge, MA, 1949.

[77] MathWorks. MATLAB 2010.

[78] J. Durbin. The fitting of time series models. *Rev. Inst. Int. Stat.*, 28: 233-43, 1960.

[79] Y. Huang, J. Benesty, and J. Chen. *Acoustic MIMO Signal Processing*, Signals and Communication Technology, Springer, 2006.

[80] S. Haykin. *Adaptive Filter Theory, Fourth Edition*, Prentice Hall, Information and System Sciences Series, 2002.

[81] B. Gustavsen and A. Semlyen. Rational approximation of frequency domain responses by Vector Fitting. *IEEE Trans. Power Delivery*, 14(3): 1052-1061, July 1999.

[82] B. Gustavsen. Improving the pole relocating properties of vector fitting. *IEEE Trans. Power Delivery*, 21(3):1587-1592, July 2006.

[83] D. Deschrijver, M. Mrozowski, T. Dhaene, and D. De Zutter. Macromodeling of Multiport Systems Using a Fast Implementation of the Vector Fitting Method. *IEEE Microwave and Wireless Components Letters*, 18(6): 383-385, June 2008.

[84] F. Matichard et al. A Review of Advanced LIGO Hybrid Seismic Isolation and Positioning Systems. *In preparation*, 2014.

[85] D. Tshilumba et al. Vibration analysis and control of the LIGO observatories large chambers and support piers. *in preparation*, 2014.

[86] F. Matichard et al. Advanced LIGO Two-Stage Twelve-Axis Vibration Isolation and Positioning Platform. Part 1: Design and Production Overview. *Submitted for publication*, 2014.

[87] F. Matichard. Advanced LIGO Two-Stage Twelve-Axis Vibration Isolation and Positioning Platform. Part 2: Experimental Investigation and Tests Results. *Submitted for publication*, 2014.

[88] J. S. Kissel. *Calibrating and Improving the Sensitivity of the LIGO Detectors*. PhD thesis, Louisiana State University and Agricultural and Mechanical College, July 2009.

[89] G. D. Meadors, K. Kawabe, K. Riles. Increasing LIGO sensitivity by feedforward subtraction of auxiliary length control noise. *Classical and Quantum Gravity*, 31(10):105014, 2014.

[90] B. J. Carr and S. W. Hawking. Black Holes in the Early Universe. *Mon. Not. R. astr. Soc.* 168:399-415, 1974.

[91] M. A. Abramowicz, W. Kluzniak, J. E. McClintock, and R. A. Remillard. The importance of discovering a 3:2 twin-peak quasi-periodic oscillation in an ultraluminous X-ray source, or how to solve the puzzle of intermediate-mass black holes. *Astrophys. J.* 609:L63-L65, 2004.

[92] D. R. Pasham, T. E. Strohmayer, and R. F. Mushotzky. A 400-solar-mass black hole in the galaxy M82. *Nature*, 513:74-76, September 2014.

[93] K. Venkateswara, C. A. Hagedorn, M. D. Turner, T. Arp, and J. H. Gundlach. A high-precision mechanical absolute-rotation sensor. *Rev. Sci. Instrum.*, 85:015005, 2014.

[94] V. Dergachev et al. A high precision, compact electromechanical ground rotation sensor. *Rev. Sci. Instrum.*, 85(5), 2014.

[95] B. Lantz, R. Schofield, B. O'Reilly, D.E. Clark, and D. DeBra. Requirements for a Ground Rotation Sensor to Improve Advanced LIGO. *Bulletin of the Seismological Society of America*, 99(2B): 980-989, May 2009.

[96] M. Zumberge, J. Berger, J. Otero, and E. Wielandt. An Optical Seismometer without Force Feedback. *Bulletin of the Seismological Society of America*, 100(2):598605, April 2010.

[97] D. E. Clark. *Contorl of Differential Motion Between Adjacent Advanced LIGO Seismic Isolation Platforms*. PhD thesis, Stanford University, March, 2013.

[98] K. Dahl, G. Heinzel, B. Willke, K. A. Strain, S Gossler, and K. Danzmann. Suspension platform interferometer for the AEI 10 m prototype: concept, design and optical layout. *Classical and Quantum Gravity*, 29(9) 095024, 2012.

[99] P. Horowitz and W. Hill. *The Art of Electronics*. Cambridge University Press, 1989.

[100] Michele Maggiore. *Gravitational waves*, volume 1. Oxford Univ. Press, November 2008.

[101] S. Mukherjee for the LSC. Multidimensional classification of kleineWelle triggers from LIGO science run. *Classical and Quantum Gravity*, 23(19), 2006.

[102] S. Mukherjee, R. Obaid, and B. Matkarimov. Classification of glitch waveforms in gravitational wave detector characterization. *Journal of Physics: Conference Series*, 243(1):012006, 2010.

[103] S. Chatterji. *The search for gravitational wave bursts in data from the second LIGO science run*. PhD thesis, Massachusetts Institute of Technology, 2005.

[104] S. Chatterji, L. Blackburn, G. Martin and E. Katsavounidis. Multiresolution techniques for the detection of gravitational-wave bursts. *Classical and Quantum Gravity*, 21, 2004.

[105] G. Bertotti. emphHysteresis in Magnetism. Academic Press, 1998.

[106] Stanford Research Systems. http://www.thinksrs.com/

[107] Livingston Detector Log 12472, https://alog.ligo-la.caltech.edu/aLOG/index.php?callRep=12472

[108] T. Fricke. *Homodyne Detection for Laser-Interferometric Gravitational Wave Detectors*. PhD thesis, Louisiana State University and Agricultural and Mechanical College, May 2011.

[109] http://www.noliac.com/

[110] F. A. Levinzon. Fundamental Noise Limit of Piezoelectric Accelerometer. *IEEE Sensors Journal*, 40(1):108-111, February 2004.

[111] LISO (LInear Simulation and Optimizaiton). Written by Gerhard Heinzel.

[112] R. Weiss. *Scattering by Residual Gas*. LIGO technical note T890025, May 1989.

[113] M. E. Zucker and S. E. Whitcomb. Measurement of Optical Path Fluctuations due to Residual Gas in the LIGO 40 Meter Interferometer. *Proceedings of the Seventh Marcel Grossman Meeting on General Relativity, July 1994, Stanford University, R.T. Jantzen and G.M. Keiser, eds.*, 1996.

[114] B. Widrow, D. Shur, and S. Shaffer. On adaptive inverse control. *15th Asilomar Conference on Circuits, Systems, and Components*, pp. 185-189, 1981.

[115] J. C. Driggers, M. Evans, K. Pepper, R. Adhikari. Active noise cancellation in a suspended interferometer. *Review of Scientific Instruments*, 83(2):24501, February 2012.

[116] J. H. Pold. *Design, Implementation, and Characterization of the Advanced LIGO 200 W Laser System*. PhD thesis, Gottfried Wilhelm Leibniz Unversitat Hannover, 2014.

[117] P. Kwee et al. Stabilized high-power laser system for the gravitational wave detector Advanced LIGO. *Optics Express*, 20(10):10617-10634, 2012.

[118] T. J. Kane and B. L. Byer. Monolithic, unidirectional single-mode Nd:YAG ring laser. *Optics Letters*, 10(2):65-67, 1985.

[119] A. Staley et al. Achieving Resonance in the Advanced LIGO Gravitational-Wave Interferometer. *Submitted for publication*, 2014.

[120] M. Evans et al. Lock acquisition of a gravitational-wave interferometer. *Optics Letters*, 27(8):598-600, 2002.

[121] A. J. Mullavey et al. Arm-length stabilization for interferometric gravitational-wave detectors using frequency-doubled auxiliary lasers. *Optics Express*, 20(1):81-89, 2012.

[122] K. Arai et al. Sensing and controls for power-recycling of TAMA300. *Classical and Quantum Gravity*, 19:1843, 2002.

[123] R. L. Ward. *Length Sensing and Control of a Prototype Advanced Interferometric Gravitational Wave Detector*. PhD thesis, California Institute of Technology, 2010.

Vita

Ryan Thomas de Rosa was born in 1983, in Philadelphia, Pennsylvania. He received bachelor degrees in physics and optical engineering from the University of Rochester, in Rochester, NY, in 2006. After working as a researcher in condensed matter physics at the National High Magnetic Field Laboratory (NHMFL), in Tallahassee, Florida, he began graduate studies in physics at the Louisiana State University, Baton Rouge, in 2008.